POLITECNICO DI TORINO

CORSO DI LAUREA MAGISTRALE IN INGEGNERIA AEROSPAZIALE

Development of an Optical Sensor Simulator for Space-Based Debris Surveillance

Anno Accademico: 2022/2023
Referente: Dr. Fabrizio stesina
Supervisore: Dr. Jens Utzmann
Tutore: Mr. Giovanni Cirillo
Tutore: Mr. Martin Michel
Candidato: Cantarella Simone
Nr-Matr..: 290654

Data: 2023-07-16

Acknowledgments

I wish to show my gratitude to my university and company supervisors, Dr. Fabrizio Stesina and Dr. Jens Utzmann, without whom I would not have had the opportunity to develop this work.

I also want to extend my thanks to the rest of the Airbus SSA team, who always patiently helped to answer even the most extreme of my inquiries and helped propel my curiosity farther, to great effect.

I further extend my thanks to Antonio and Janik for helping me with their relevant technical know-how and to the rest of the Airbus interns who contributed to making my stay pleasant and enviable.

Additionally, I want to thank all my past and current friends from Turin and Rome who, even after long hiatuses, have proven repeatedly to be my very own safety net.

Last but not least, my deepest thanks go to my family for their unconditional support even during the most difficult of situations.

Abstract

Since the 2007 Chinese anti-satellite missile test, Space Debris has become a dominating talking point within the space community, prompting initiatives like the European Space Agency's Space Situational Awareness (SSA) program – started in 2009 - to track and catalogue fragments and leftover upper stage structures.

This study aims to develop a tool capable of simulating images of debris captured from a satellite operating from a Sun-synchronous orbit, to develop software prior to launch that enables the onboard processing of this particular image data.

To accomplish this objective, a Python-based tool was developed following an object-oriented programming approach. The tool integrates crucial data sources, including the GAIA Star Catalogue, which provides accurate positions and brightness information of stars, and the SPOOK object propagator for synthetic debris objects. Realistic Cosmic Ray maps were also derived from data on proton fluxes within the South Atlantic Anomaly.

The image simulator is designed for utilization of both CCD and CMOS sensors, tailored for a Newtonian-type telescope. It incorporates a Point Spread Function to simulate photon diffraction on the pixel wells of the sensor, and permits us to generate distinct "point" and "streak" features. The simulator effectively accounts for various sources of noise, including poissonian-like events such as atmospheric dispersion and straylight of photon sources, as well as non-poissonian noises like readout and reset noise. This model was compounded by an in-depth analysis and modelling of defective pixels, through reverse engineering of data from both types of sensors. Finally, an optical performance model is also integrated to predict and simulate photon collection from artificial objects based on their albedo, size, shape, temperatures and dimensions.

The results demonstrate the effectiveness of the developed software through 15 validation scenarios, with an additional two scenarios recreating real-life pointing and tracking situations for both CCD and CMOS sensors. These simulations have yielded significant improvements in background noise modeling and Signal-to-Noise Ratio (SNR) approximation. The outcomes provide a foundation for the development of onboard software for debris tracking and segmentation, which would enable Airbus' projects to process data directly onboard space-based telescope without the need to transmit large image files.

Table of contents

List of Acronyms

SPOOK	Special Perturbations Orbit determination and Orbit analysis toolKit
ART	Airbus Robotic Telescope
SST	Space Surveillance and Tracking
ISO	International Organization of Standards
CCD	Charge-Coupled Device
CMOS	Complementary Metal Oxide Semiconductor
A/D	Analog-to-Digital
ADU	Analog-to-Digital Units
LEO	Low Earth Orbit
MEO	Medium Earth Orbit
GEO	Geostationary Earth Orbit
ESA	European Space Agency
FOV	Field of View
NASA	National Aeronautics and Space Administration
FITS	Flexible Image Transport System
FWHM	Full Width at Half Maximum
EE	Ensquared Energy
SNR	Signal-to-Noise Ratio
WCS	World Coordinate System
SIP	Simple Imaging Polynomial
RMS	Root-Mean-Square
T2D	Time-to-Double
PDF	Probability Density Function
QQ	Quantile-Quantile
RA	Right Ascension
DEC	Declination
ICRS	International Celestial Reference System
SAA	South Atlantic Anomaly
PSF	Point Spread Function
IOD	Initial Orbit Determination
R&D	Research and Development
FPS	Frames Per Second
COTS	Commercial Off-the-Shelf
GNSS	Global Navigation Satellite System

List of Tables

List of Figures

Introduction

The Space Debris challenge

On June 29, 1961, 77 minutes after the separation of Transit-4A, the upper stage of the Thor-Ablestar vector exploded, scattering almost 300 trackable fragments in MEO. To this date, roughly two thirds of these fragments are still orbiting Earth, along with an unknown number of uncatalogued debris. At the time, this single event more than tripled the debris population orbiting Earth, and in 60 years of space endeavours this population has risen to 56450 tracked objects, of which an approximate 28160 have not de-orbited and are currently tracked by the US Space Surveillance Network.[1]

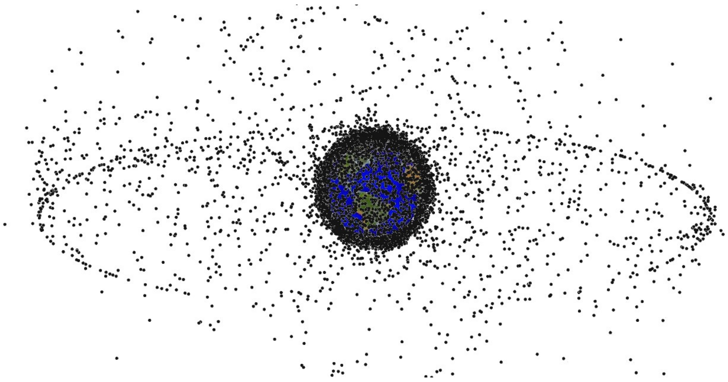

Figure 1: Distribution of debris on GEO, Credit: NASA ODPO

The Inter-Agency Space Debris Coordination Committee (IADC) provides a definition for these kinds of space fragments, stating that *”Space debris are all man made objects including fragments and elements thereof, in Earth orbit or re-entering the atmosphere, that are non functional”*. Thus, for space debris, we do not only consider fragmentation from accidental explosions, but also leftover structures from spent upper stages or discarded equipment. [2] Compounding these issues, three-body interactions resulting from luni-solar influence, along with atmosphere drag, can shift the orbital parameters of these objects leading to potential orbit safe-keeping risks.

Current tracking capabilities are limited to a 5 cm definition for LEO and 30 cm for GEO, however ESA estimates show that even millimiter-size fragments can cause detrimental damage to subsystems, and objects larger than 1 cm could cause break-up events of satellites.[1] [3] These types of in-orbit collisions have devastating results on debris populations, with the first-ever recorded case happening in 2009 and generating 2300 trackable fragments (Iridium-33 and Kosmos2251 collision). Other worrying strategical concerns arise from untracked spy satellites, and engagement demonstrations such as the FengYun-1C intercept of 2007, which alone raised debris population by an estimated 25%. Figure 2 shows this trend broken down into it's contributing objects.

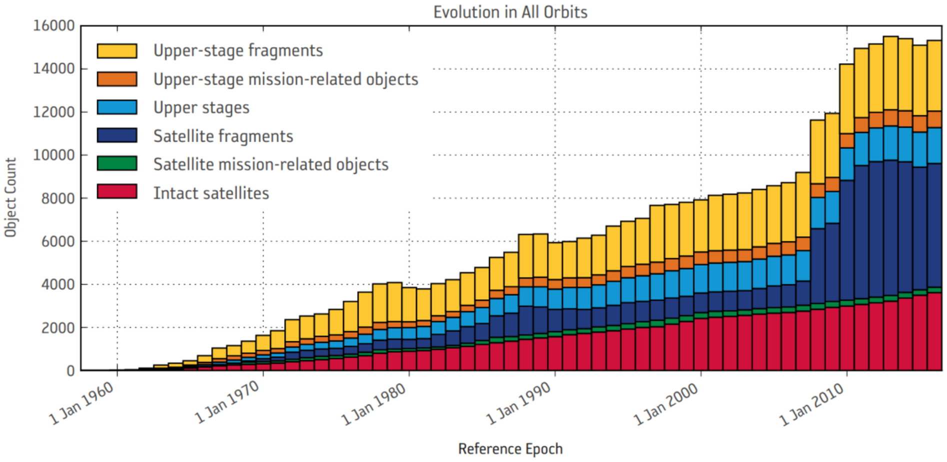

Figure 2: Evolution of tracked debris population as of February 2017 [3]

Were the debris population be left unchecked to rise, collisions would unavoidably rise, potentially leading to the manifestation of what is known as the *Kessler Syndrome*, a type of chain reaction where the rate of debris creation is self-sustained by the collisions from the debris density itself.

Mitigating and preventive action has been undertaken to try and contain the issue, with Europe leading the The Space Situational Awareness (SSA) Programme instituted in 2009 to combat the rise of debris population. Under the programme, ESA aims to acquire an independent capability to overwatch *"objects and natural phenomena that could harm satellites in orbit or infrastructure such as power grids on the ground"*. To fulfill these goals, the SSA programme has identified three core areas of research:

- **Space Weather (SWE)**: to monitor and predict the interplanetary and planetary environments which could affect the integrity or quality of human life.
- **Near-Earth Objects (NEO)**: to detect natural asteroids that could potentially intercept the Earth's path.
- **Space Surveillance and Tracking (SST)**: to oversee the orbital life of active and inactive objects orbiting Earth.

These topics are actively being developed in parallel, with significant contributions from existing European collaborators such as Airbus. European accomplishments in the field include (according to ESA Space Safety office):

- Research and development in satellite laser ranging
- Research and development in optical surveillance techniques
- Test and validation of radar detection techniques
- Development and installation of a monostatic test radar, Santorcaz, Spain
- Development and installation of a bistatic test radar, France
- Execution of multiple 'Collision Avoidance Manoevres' from ESOC teams

As of 2019, the work of the Space Surveillance and Tracking segment has fallen under the Space Debris Office, operational within the ESOC facility, headquartered at Darmstadt, Germany.

With the recent surge of launches into outer space, mostly thanks to the 12000 planned platforms for the Starlink constellation (shown in Figure 3), space surveillance has begun to turn into both a safety and security concern.

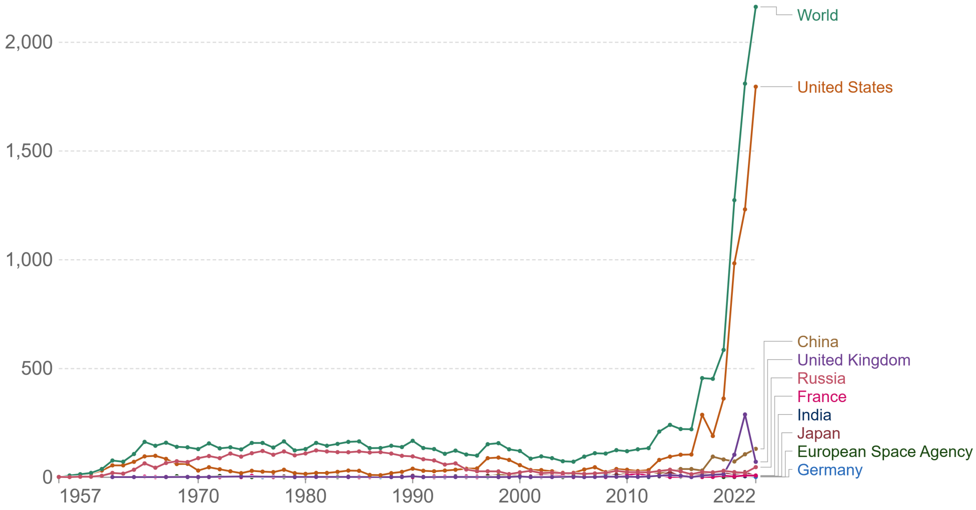

Source: United Nations Office for Outer Space Affairs, Online Index of Objects Launched into Outer Space (2023)
Note: When an object is launched by a country on behalf of another one, it is attributed to the latter.

Figure 3: Yearly number of objects launched into outer space

Goals and Structure of the Thesis

The main objectives on which this thesis is built upon are outlined here:

- Study of Error sources that affect the astrometric measurements of optical sensors
- Evaluation of existing telescopic imagery to identify faults and apply image correction techniques
- Enhancement of the Image Simulator modes and functionalities
- Definition of a validation pipeline for the implemented software

To properly reflect these goals, the thesis has been structured to provide the reader with a comprehensive breakdown of the relevant phenomena:

- The current chapter introduces the orbital debris problem and provides an overview of the thesis
- Chapter 1 introduces the relevant hardware and software utilized during the thesis, and describes typical observation scenarios
- Chapter 2 dissects the error sources affecting the measurements
- Chapter 3 introduces the Image Simulator, broken down into its various modules
- Chapter 4 discusses validation scenarios and demonstrates procedures to validate real-life images
- Chapter 5 provides an overview of the results and an outlook for future improvements

Further details regarding particular topics and techniques are grouped in an Annex chapter.

1 Overview of hardware & software

1.1 ART and SBOC

The Airbus Robotic Telescope (ART) constitutes a key component in the validation pipeline in the B2 phase of the Space-Based Optical Component (SBOC) project. Quoting *Cirillo2023*[4]: *"SBOC is an optical payload, intended to be used as payload for the ESA VISDOMS-mission (Verification of In-Situ De- bris Optical Monitoring from Space). The main goal of this mission is to improve the knowledge on the distribution of small debris in LEO, which cannot be detected by ground-based sensors."* The planned mission places the payload on a dawn-dusk sun-synchronous orbit, pointing towards anti-Sun direction.

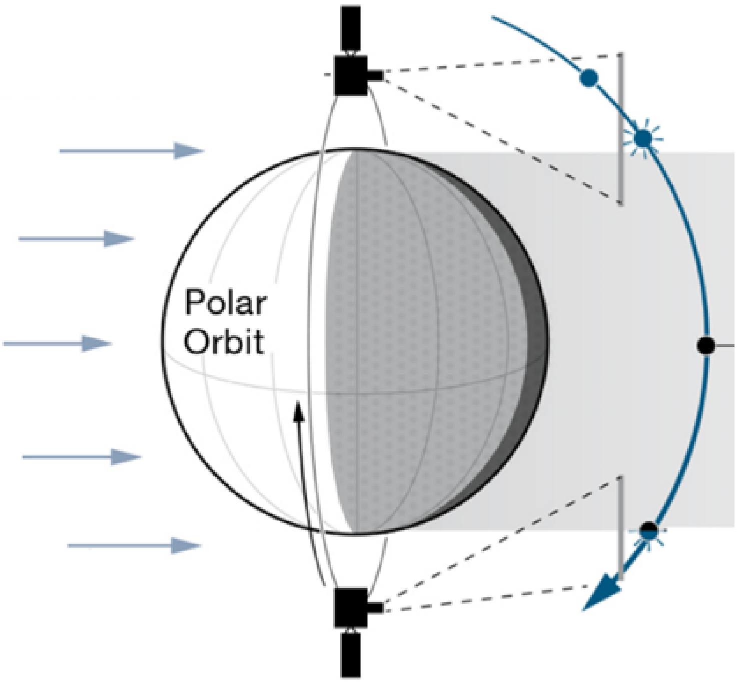

Figure 4: Typical surveillance scenario from a Sun- synchronous orbit [4]

Deployed in June of 2018, ART is a 40 cm aperture Newtonian telescope located in Extremadura Spain. Its deployement has enabled Airbus to perform tracking and sideral observation and to develop its own end-to-end Processing Pipeline in the SST field. ART provides the team with crucial image data for SSA development activities for participation in international measurement campaigns. The location for the telescope has been selected for its optimal observation conditions, with favourable enviromental and meteorogical observations (low seeing effects and roughly 260 clear night per year)[5].

Figure 5: The Airbus Robotic Telescope

In January of 2023 ART has undertaken a significant upgrade, via installation of a new camera with a large CMOS detector. This new hardware has enabled the telescope with a wider FOV, higher sensitivity and higher frame rates, similar to the ones planned for use within the SBOC flight model. The new hardware is capable of on-board binning of images provided in the FITS data handle format.

Focal Lenght	960 mm	
Aperture Diameter	400 mm	
Readout times	2 Mhz, 12 Mhz	
Wavelenght range	300 nm to 1000 nm panchromatic	
Surveillance modes	Sideral, Tracking	
Detector type	CCD	CMOS
Detector size	4008 x 2672 pxl	14192 x 10640 pxl
Field of View	2.15 x 1.43 deg	3.07 x 2.19 deg

Table 1: ART technical specifications [5]

The Newtonian-style telescope utilized features a two-mirror configuration of parabolic reflectors, to collect photons at a 90° angle on a focal plane where the camera sensor is placed. The primary mirror (objective) collects light from the enveloped FOV, and through the use of the secondary mirror and baffles at the aperture it is possible to eliminate most of unwanted straylight sources. Newtonian telescopes are a convenient solution when performing astrometry, since they do not experience the chromatic aberration typical of refracting telescopes, and they are less expensive than their comparable counterparts.

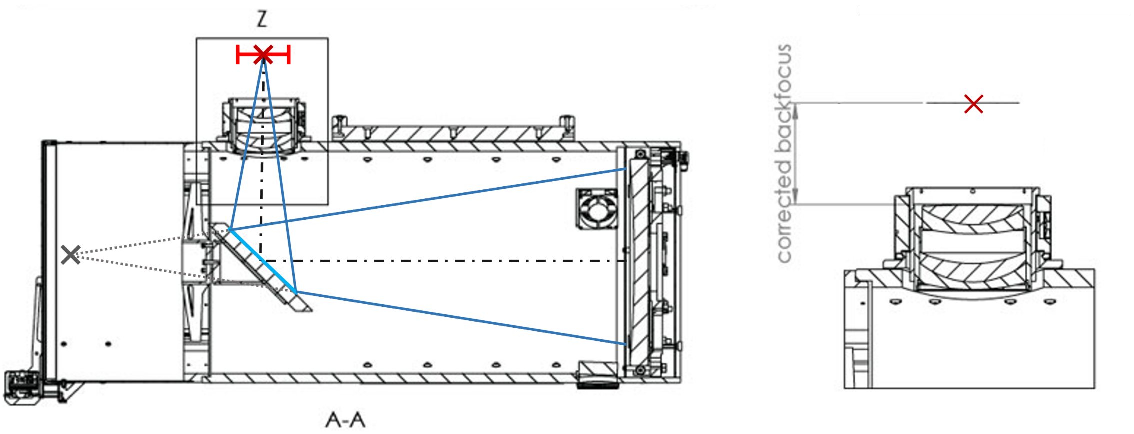

Figure 6: ART's internal double-mirror configuration

1.2 Tracking and Surveillance scenarios

A set of reaction wheels built into the gimbal mount of the telescope allow for 2 DOF rotations in order to perform observations on varying RA/DEC coordinates. We define as dRa/dDEC the velocities of the objects observed in this reference system: if these values are known and already stored in the catalogue, we are able to perform a tracking scenario by matching the rotation of the satellite with the relative position of the object on the celestial sphere. In this scenario, only the tracked object appears as a *point source*, whereas all other objects are seen as *streaks* due to the effects of motion blur.

In an ideal scenario, the aperture would be perfectly aligned with the light source during tracking, and all the signal would be concentrated in one single pixel throughout the whole exposure. In reality, diffraction effects create an "Airy disc" pattern on the pixel well, and vibration phenomena during tracking compound this issue, effectively "de-focusing" the point source.

Tracking is especially useful when computing operations such as: light-curves determination, telescope calibration, signal power analyses and astrophotography of LEO objects. Typical exposure times range from 0.5 to 30 seconds, and known GPS satellite coordinates are often used to calibrate the gimbal tracking controls of the mount.

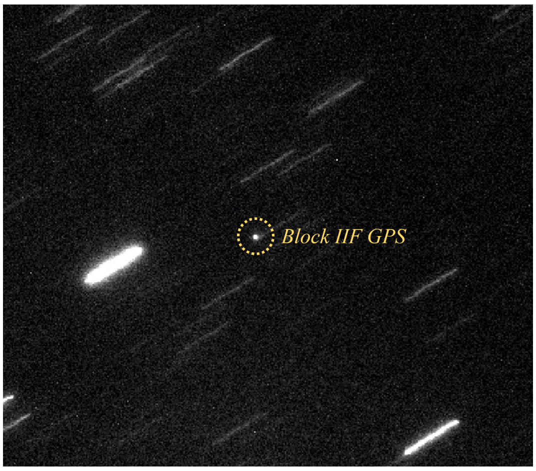

Figure 7: Tracking scenario on a Block IIF GPS object

Surveillance scenarios scenarios are the conventional fixed-view images of stars, constellations, and faraway objects (Sideral observations). These observations are usually performed at high exposure times (up to 300s) to calibrate the camera and at shorter exposure times (0.5- to 5s) when scanning for potential debris across a determined FOV. In these scenarios, stars and faraway galaxies often appear as still point sources, whereas rapidly moving debris or satellites appear as long streak-like sources.

These streaks are helpful to perform Initial Orbit Determination (IOD), especially if we are able to catch both ends of the streak within our FOV. When an unknown object is recorded, it is added to the catalogue and scheduled for future observation to improve the determination of its orbital parameters.

The total signal power of the object is spread thin along the entire streak, in addition to the other diffraction phenomena mentioned prior. For these reasons, photometrists often employ terms such as Full Width at Half Maximum, or Ensquared Energy, to define the severity of the dispersive effects on these signal sources.

The following image displays an example of a sideral observation scenario where a single streak source is detected crossing the entire field.

Figure 8: 300s exposure of the M82-M81 "ballet" in the Ursa Major constellation

1.3 Sensor types

Optical sensors are key components in astrophotography, enabling the capture of light from celestial objects. They convert the incoming light into electrical signals, which are then processed and transformed into digital images. These sensors have to be highly sensitive, allowing the detection of faint light sources and fine details in astronomical objects.

Optical sensors come in different types, each with its own advantages and characteristics. They enable long-exposure imaging to capture dim and distant objects, and their high resolution provides detailed images of galaxies, nebulae, and other celestial phenomena.

Generally, optical sensors perform a four-phase process when capturing each frame:

1. **Exposure**: the sensor is exposed to light, and the photons captured interact with the sensor's light-sensitive elements generating electrical charges proportional to the intensity of the incident source.

2. **Readout**: In this phase, the accumulated electrical charges or voltage in each pixel of the sensor are sequentially read out. Analogue to digital conversion is then performed.

3. **Reset**: the pixel charges are reset to a baseline level, to avoid any residual charge from influencing subsequent frames.

4. **Post-processing**: a variety of processing steps can be applied to manipulate the digital data, such as binning, salt-pepper noise reduction, stacking and signal amplification. The image is then stored in an appropriate image format (such as .FITS).

In this section we shall discuss only the sensor types relevant for our criteria of use, but they can come in a variety of configurations that suit a diverse range of applications.

1.3.1 CCD Sensors

CCD (Charge-Coupled Device) sensors are electronic optical devices used to capture and digitalize light signals. They have a variety of employments in many imaging applications, including astrophotography and astrometry. CCD sensors consist of a 2D array of pixel wells that collect photons and convert them into electrical charges.

The CCD sensor operates on the principle of the photoelectric effect. Within each pixel well a photosensitive element is contained, often some kind of silicone-based photo-diode. When a photon strikes a photo-diode, it generates an electric charge proportional to the intensity of the incident light. This process effectively converts a photon signal into "free-electron" signal, that is the number of released electrons detected in the readout process. This conversion is not lossless, and wavelengths are converted differently from eachother: these constitute an intrinsic sensor property known as *Quantum Efficiency*, which is often provided as an interpolation of the sampled free-electrons at different wavelengths.

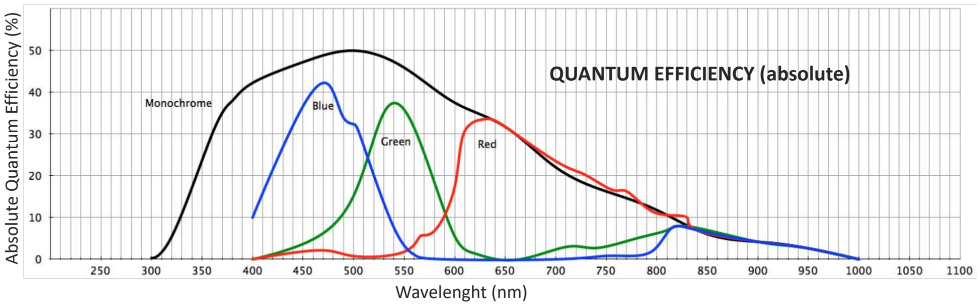

Figure 9: Quantum efficiency curves for the MicroLine ML 11002 sensor

The charge is then trasfered across the sensor using a "charge-coupled" structure, that is a series of capacitors that shifts accumulated charges in a line of pixels to an output amplifier. At the readout, the amplifier convers the now-analog signal into digital values (ADU), which are then stored as an uncompressed image file.

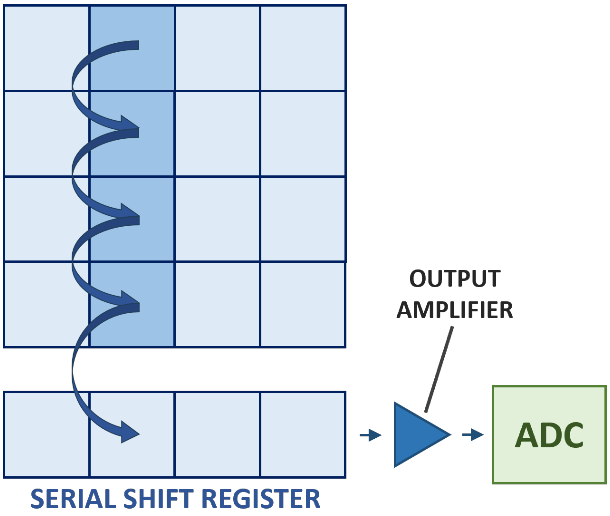

Figure 10: CCD sensor readout process

CCD sensors have revolutionized the field of astrophotography and astrometry thanks to their high sensitivity and low noise characteristics, compared to consumer-grade photography systems. Thanks to their extremely low thermal leakages, they excel in long-exposure settings, which are critical in astrophotography when capturing faint celestial objects.

ART hosted a MicroLine ML 11002 until January of 2023. ML 1002 is a type of high-performance CCD with a 4008x2672 imaging array, low noise, and wide dynamic range; making it especially suited for these kinds of applications.

1.3.2 CMOS Sensors

CMOS (Complementary Metal-Oxide-Semiconductor) sensors have recently gained massive popularity in the space community, thanks to their massively improved performance in readout speeds, lower power consumption, and cost-effectiveness.

The pixel array of a CMOS operates differently from a CCD, with photo-diodes, transistors and amplifiers all embedded within each pixel well. This means that charge conversion from photon to digital units takes place directly within the pixel itself, without the need of charge transfer mechanisms. This peculiarity boosts significantly the readout speeds and sensitivity, and makes these sensors particularly well-suited for capturing fast-moving objects.

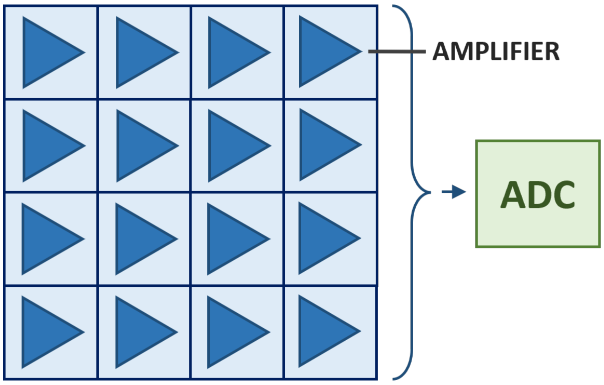

Figure 11: CMOS sensor readout process

Some CMOS sensors employ back-side illumination (BSI) technology. In traditional sensors, the circuitry is positioned between the light-sensitive surface and the incoming light, causing some light to be blocked. BSI CMOS sensors address this issue by flipping upside down the sensor and placing the circuitry on the backside, allowing more light to reach the light-sensitive area. This enhances the sensor's sensitivity, making it advantageous for astrometric applications where capturing faint signals is crucial.

A critical characteristic of most CMOS sensor is the rolling shutter under which they operate. Unlike the global shutters of CCD sensors, CMOS sensors readout images row by row. This can lead to artifacts and distortions during relative motion, and some mitigation techniques might be required to compensate for these effects. As of the time of this paper, CMOS with built-in global shutters remain too expensive to be justified for some R&D applications.

Since January of 2023, the ART has been upgraded with the Sony IMX411 camera sensor, a high-performance CMOS sensor with back-side illumination featuring a 14192 x 10640 camera array, a larger FOV and extremely lower readout noise. However, due to the greater density of amplifiers and smaller pixel sizes, the camera experiences greater charge leakage and is more suited for shorter exposures.

1.3.3 FITS images

Originally standardized in 1981 by NASA, the Flexible Image Transport System (FITS) is a digital image format that supports inclusion of a variety of non-image data extensions. The format is commonly used for astronomic purposes, and allows for storage of metadata through Headers, included in a multi-table database of key-value pairs. These Headers provide astronomers to a direct and readable access to commonly used parameters for astrometric evaluations.The FITS format provides uncompressed data and supports up to 64 signed integers and is maintained by the International Astronomical Union (IAU) FITS Working Group, with Version 3 being published in 2010.

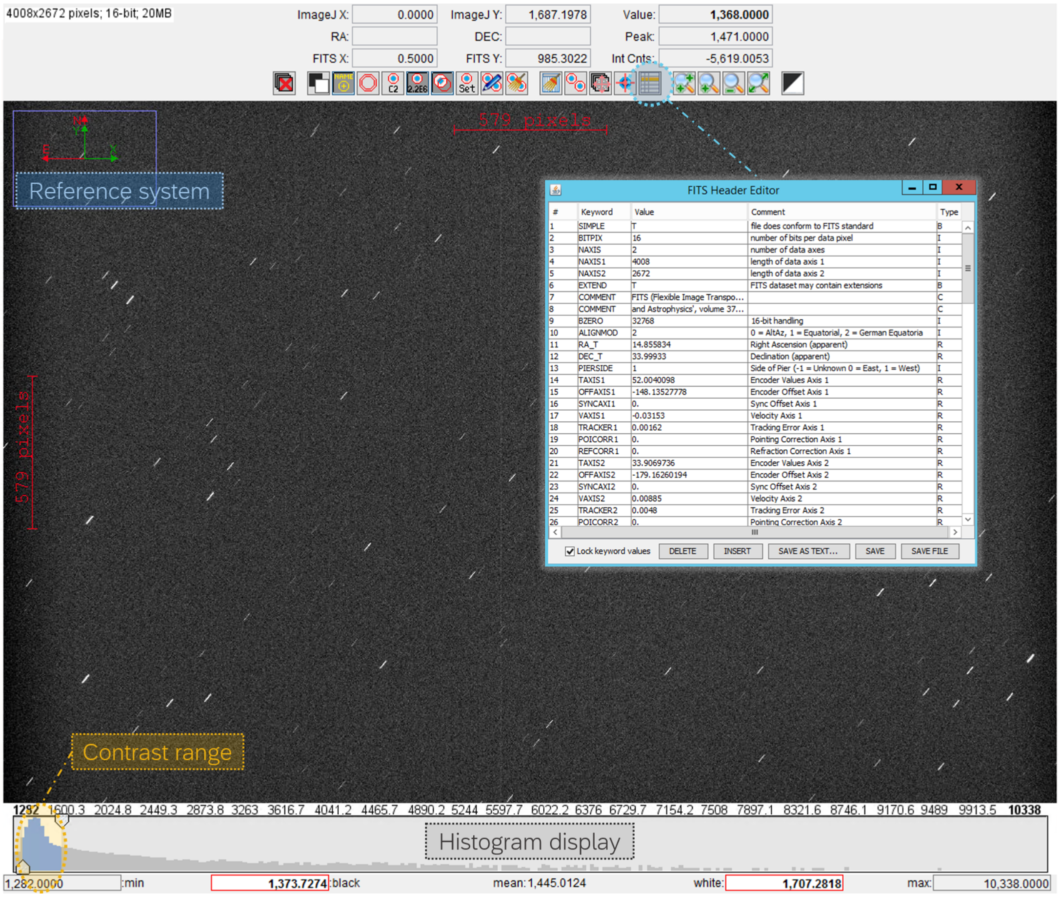

4008x2672 pixels; 16-bit; 20MB

ImageJ X: 0.0000
ImageJ Y: 1,687.1978
Value: 1,368.0000
RA:
DEC:
Peak: 1,471.0000
FITS X: 0.5000
FITS Y: 985.3022
Int Cnts: -5,619.0053

FITS Header Editor

#	Keyword	Value	Comment	Type
1	SIMPLE	T	file does conform to FITS standard	B
2	BITPIX	16	number of bits per data pixel	I
3	NAXIS	2	number of data axes	I
4	NAXIS1	4008	length of data axis 1	I
5	NAXIS2	2672	length of data axis 2	I
6	EXTEND	T	FITS dataset may contain extensions	B
7	COMMENT	FITS (Flexible Image Transpo...		C
8	COMMENT	and Astrophysics', volume 37...		C
9	BZERO	32768	16-bit handling	I
10	ALIGNMOD	2	0 = AltAz, 1 = Equatorial, 2 = German Equatoria	I
11	RA_T	14.855834	Right Ascension (apparent)	R
12	DEC_T	33.99933	Declination (apparent)	R
13	PIERSIDE	1	Side of Pier (-1 = Unknown 0 = East, 1 = West)	I
14	TAXIS1	52.0040098	Encoder Values Axis 1	R
15	OFFAXIS1	-148.13527778	Encoder Offset Axis 1	R
16	SYNCAXI1	0.	Sync Offset Axis 1	R
17	VAXIS1	-0.03153	Velocity Axis 1	R
18	TRACKER1	0.00162	Tracking Error Axis 1	R
19	POICORR1	0.	Pointing Correction Axis 1	R
20	REFCORR1	0.	Refraction Correction Axis 1	R
21	TAXIS2	33.9069736	Encoder Values Axis 2	R
22	OFFAXIS2	-179.16260194	Encoder Offset Axis 2	R
23	SYNCAXI2	0.	Sync Offset Axis 2	R
24	VAXIS2	0.00885	Velocity Axis 2	R
25	TRACKER2	0.0048	Tracking Error Axis 2	R
26	POICORR2	0.	Pointing Correction Axis 2	R

☑ Lock keyword values

1,282.0000 :min
1,373.7274 :black
mean: 1,445.0124
white: 1,707.2818
max: 10,338.0000

Figure 12: The AstroImageJ interface for the .fits image format

FITS files are supported by a large range of programming languages used for data analysis, and programs such as AstroImageJ provide a useful GUI to perform a variety analyses of without the need of writing ad-hoc code. For debris observation, performing rapidly image stacking and gaussian filtering can prove particularly useful when trying to capture faint objects while Tracking, and AstroImageJ supports for these operations. More details regarding the technique of image stacking are provided in Annex I.

2 Sources of error

Astrometric observations do not normally provide a direct means to access the signal we're interested in, but merely a function of it from which we need to perform a process known as *data reduction of observations*. Through observable parameters and assumed statistical properties, one can come up with mathematical approaches to treat the measures observed and reconstruct the data we are actually interested in.

Data reduction thus constitutes an integral process to obtain positions, relative motion, signal strength and most other astrometric and photometric properties of celestial bodies. However, no observation is exempt from errors, which for the sake of clarity are defined here to be affecting the *uncertainty* of a measurement. One should expect that if we could evaluate all of these uncertainties and have their behaviour corrected, then our measurements would improve. This assumption, however, is not necessarily true, and we first need to distinguish between the various contributing uncertainties that affect the confidence in our results:

- **Random errors** arise from unpredictable, or stochastic, variations of a parameter that affect the measurement of a quantity. They exhibit fluctuating and agitated behavior and cannot be corrected without degrading the quality of other measurements. These affect the *precision* of a measurement.

- **Systematic errors** are unknown or unmodelled effects, which if corrected would improve astrometric performance. They exhibit a consistent behaviour across observations that requires estimation techniques to correct for. These errors affect the *accuracy* of a measurement.

Combined, the estimates from these two families of errors provide us with the uncertainty of a measurement. For astrometric data reduction, only systematic errors have to be accounted for, but for the purposes of a image simulator knowledge on reconstruction of random errors is also required.

2.1 Projection method

Although not strictly a source of uncertainty, projection methods are a modelling approach that needs to be accounted for. Since the observation is taking place at the focal plane of the telescope, we are technically performing a geometric transform of the celestial sphere. This type of projection (from *standard world coordinates* to *relative pixel coordinates*) is known as **Gnomonic projection**, a type of *central projection*.

To perform this kind of projection, we select an image plane that is typically tangent to the sphere, and a point known as the center of the projection. Then, to determine the image of a point, we simply take the line passing through the point's center and locate its point of intersection with the plane.

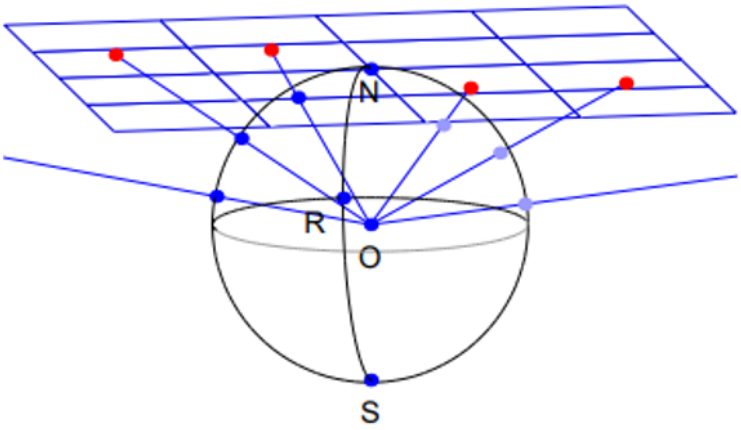

Figure 13: Gnomonic Projection

Due to the geometry of the problem, we experience a combination of expansion and distortion phenomena ad the edges of the projection, for which we model an expansion ellipse and observe the two effects separately.

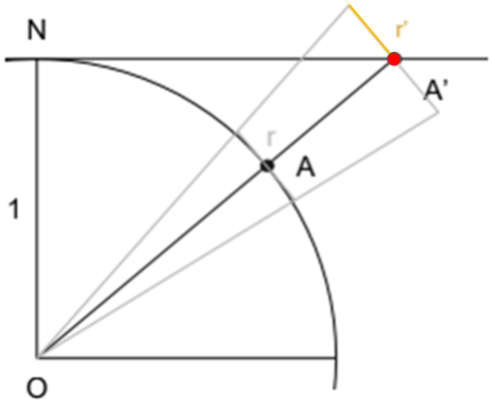

Figure 14: Expansion effects

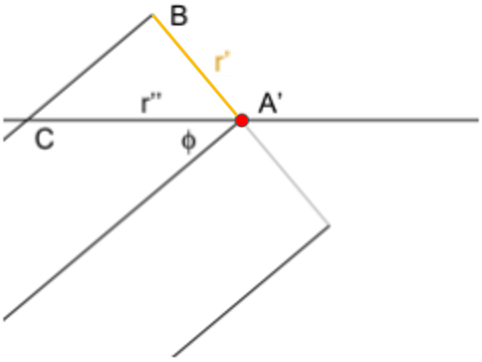

Figure 15: Distortion effects

Where $r' = r/\sin(\phi)$ and $r" = r/\sin^2(\phi)$. From Figure 16, which illustrates the expansion ellipse for a non-central projection, we come to the conclusion how the method is not area preserving and is not conformal, with distortion becoming greater at the edges of the projection on the focal plane.

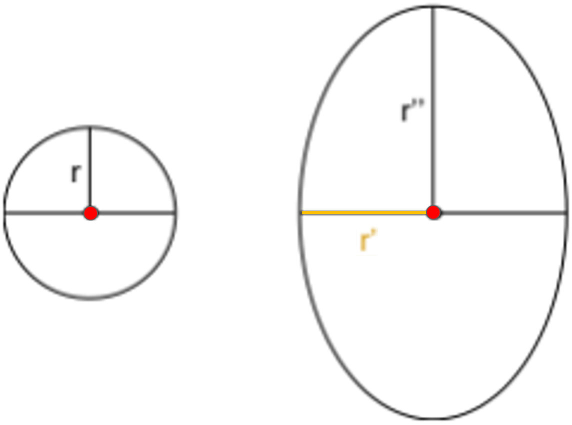

Figure 16: Expansion ellipse in the Gnomonic projection model

2.2 Systematic errors

2.2.1 Parallactic displacements

The position and relative velocity of the observer has a noticeable impact in these scenarios, creating an apparent displacement w.r.t. our inertial reference system (ICRS). The position of our telescope causes a *parallax* effect, whereas its velocity is responsible for the phenomena known as *aberration*. Combined, they are responsible for the family of parallactic displacements.

For both of these we distinguish 3 different types:

1. **Diurnal** displacements are caused by the motion of the observer (when ground-based) around Earth's barycenter.
2. **Orbital** displacements are caused by the motion of the orbit of the observer (when space-based) around Earth's barycenter.
3. **Annual (or Stellar)** displacements are caused by revolution of the Moon-Earth system's COM around the Solar System's barycenter.

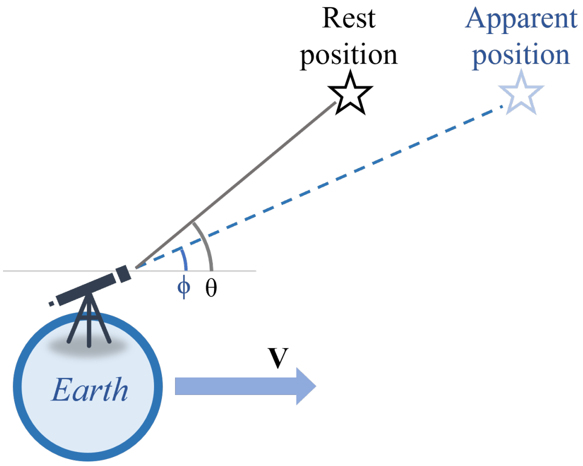

Figure 17: Aberration due to Earth's motion

To summarize:

Parallax displacements are difference in an object's apparent location when seen from two separate lines of sight. This effect is much more prevalent for closer objects, and are zeroed-out when observing at infinite distances.

Aberration displacements originate due to the time delays caused by the limitation of light-speed signals. The apparent motion of the object we observe shall be corrected for this "lag" caused by the relative motion between observer-target.

The magnitude of these effects greatly vary on observation scenarios, but generally aberration phenomena are much greater than parallax. [6]

2.2.2 Relativistic effects

According general relativity, light tends to follow the curvature of spacetime, hence when photons graze a massive object, they are bent toward a different direction. This effect, known as **Gravitational lensing** is caused by the gradient of gravitational potential of the object, and the bending angle θ depends on the mass of the object and the minimum distance from the photon path to the planetary body.

One can calculate this angle using the formula:

$$\theta = \frac{4GM}{rc^2} \tag{1}$$

Where for a sun-grazing object the angle of deflection is found to be a mere 1.75", and is completely negligible for all other celestial bodies in the Solar System.

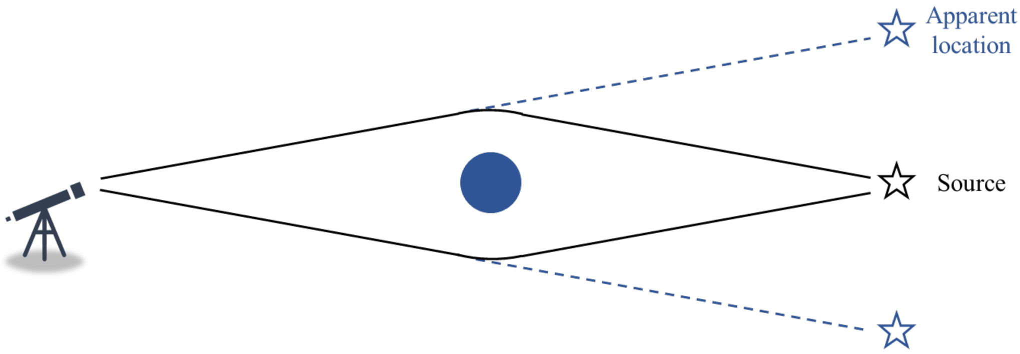

Figure 18: Gravitational lensing - schematic

Relativistic Aberration, similarly to the parallactic displacements, causes a change of the direction of a light ray when observed from inertial reference frames close to the speed of light. Its effects are described by Einstein's special theory of relativity, but the relevancy of such an effect is extremely minor.

Doppler effects, similarly to sound waves, cause a frequency shift for rapid relative radial movement. The effect is also known as *redshifting*, and has known widespread recognition for being utilized to prove the expansion of the universe. Some Doppler detection techniques utilize reflected signals to perform initial orbit determination, maneuver detection, and to perform satellite status characterization and anomaly detection.

2.2.3 Atmospheric effects

For objects in LEO and MEO, **atmospheric refraction** from the Earth's atmosphere can cause significant displacements. In a similar fashion to parallactic effects, atmospheric displacement strongly depends on the object's distance and the zenith angle.[7]

The effect is caused by the gradient in air density, which decreases at higher altitudes and with therefore decreasing index of refraction.

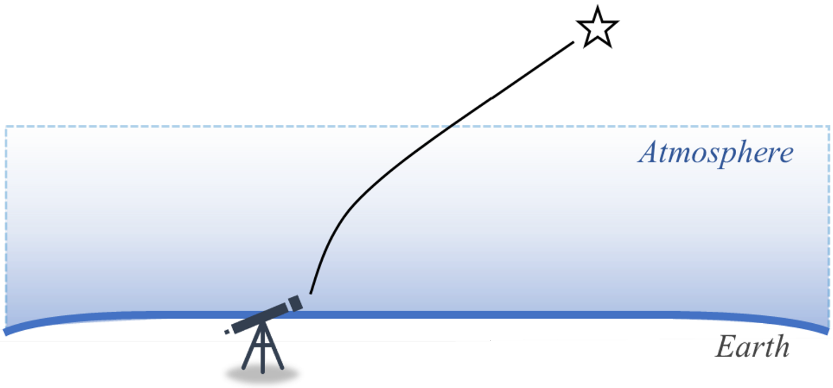

Figure 19: Atmospheric refraction of starlight - schematic

This kind of phenomena can be described through planar-stratified layers where one applies Snell's law at the interfaces:

$$n \sin(z') = \sin(z) \tag{2}$$

where z and z' are the unrefracted and refracted zenith angles, with $z' < z$.

Kaplan(2014)[7] has shown that though a simple single-slab model, refraction is entirely dependent on height and elevation. The problem is shown to be entirely geometric, with faraway objects such as stars not experiencing any refraction in terms of and demonstrates that the error increases with higher zenith angles and lower height.

In the report, the solution for this problem is shown to be (in degree terms):

$$\Delta z = (n-1) \tan z' \left(\frac{s}{h}\right) (e^{-h/s} - 1) \tag{3}$$

Where s is the height of the homogeneous atmosphere.

Results show that displacements for LEO and MEO objects are relevant (in the order of a few arcseconds), thus these type of phenomena should be accounted for.

2.2.4 Sensor-related errors

In the event of rolling shutter, exposure is performed sequentially line by line with a slight delay between line readout. While the exposure time for each line is the same, the mid-exposure times vary based on the coordinates of the line.

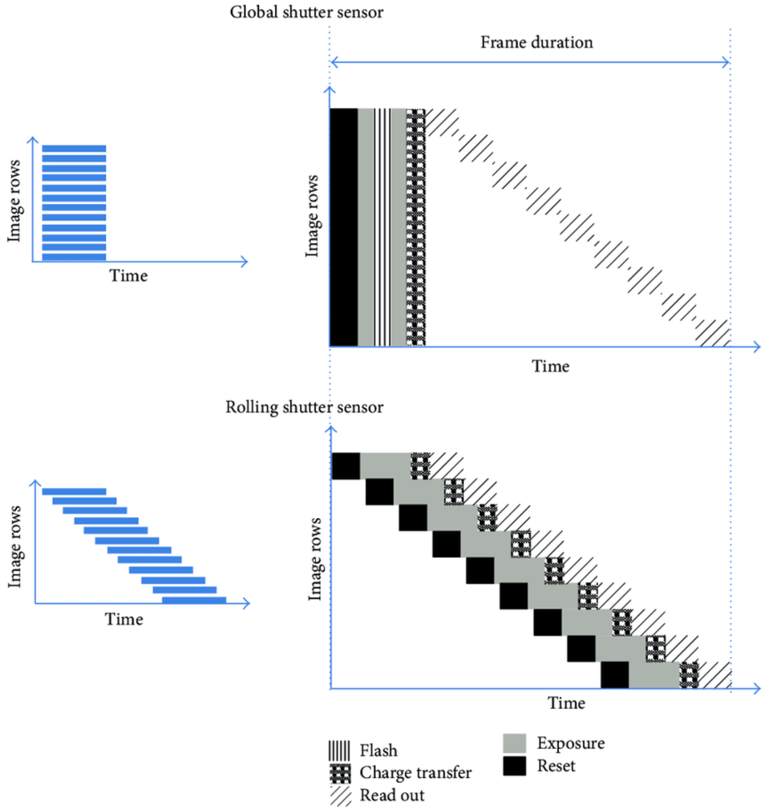

Figure 20: Readout timing for rolling and global shutter

Rolling shutters are known to cause a variety of image artifacts, of which we distinguish four different types:

- **Wobble/Jello Effect:** in the event of vibrations during exposure, straight lines will be represented as stretched and curved unpredictably.
- **Skew:** during rapid camera rotation, straight line angles are modified, causing vertical lines to appear as diagonal.
- **Spatial and Temporal aliasing:** in case of horizontal rolling shutter, vertically adjacent pixels will are sampled sequentially, causing smear for rapidly moving or rotating objects. Mid-exposure timing will also vary as a function of pixel position.

- **Partial Exposure:** in the event of steep brightness gradients or uneven flash exposure, sections of the image will experience different illumination conditions.

Wobble and Spatial aliasing are particularly relevant in the case of space debris observation, since any minor change in the energy content of the streak will affect OD techniques.

Amplifier Glow, colloquially known as "amp-glow", is a electroluminescence phenomena caused by voltage and temperature spillage from the readout circuitry. The effect is akin to a light source, or "glow", often located at the edges of the image. The behaviour is different between sensors, with CCD glow being associated with the amplifier of the serial shift register, while CMOS glow is caused by the integrated amplifiers in each pixels.

2.2.5 Platform-related errors

Calibration is an essential step in obtaining reliable astrometric data. Normally calibration for RA/DEC pointing and time correction is carried out by observing GNSS (GPS, Galileo or GLONASS) constellations, of which their ephemerides are readily available with their positions accurate to the centimeters scale. The ephemerides also contain reliable timing data which can be used to correct for time bias. Normally this is done by comparing the mid-exposure time-tag across a large number of GPS imagery, and interpolating the results to match those of the ephemerides.

Errors in sensor location, especially for Space-based observers, can also cause significant issues during operation. Usage of differential GPS is advisable to achieve a positioning accuracy that does not interfere significantly with the results.

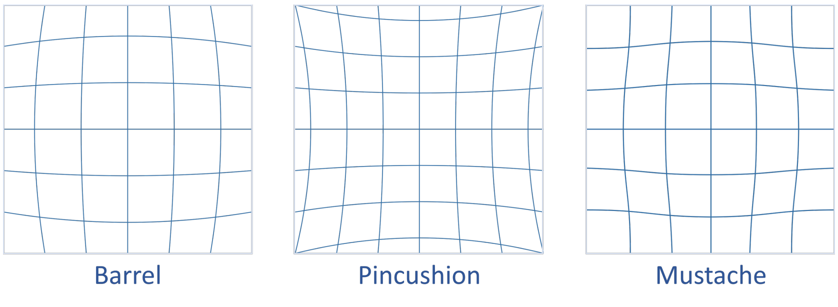

Figure 21: Examples of radial lens distortion

Other relevant issues that characterize the telescope hardware include **lens distortion**, a type of optical aberration where lines at the edges of the focal field are not projected straight.

2.3 Random errors

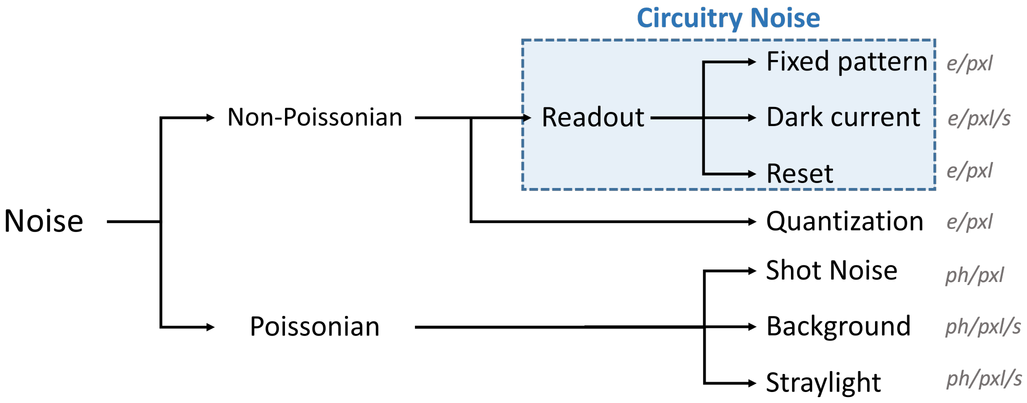

Figure 22: Taxonomy of noise sources

2.3.1 Atmospheric effects

Earth's atmosphere has proven to be a problematic interference both to ground-based and space-based astrometric operations.

The upper atmosphere absorbes most wavebands outside of radio, visible and near ultraviolet. Much of the infrared (21 mm to 1 mm) suffers from **absorption**. When using certain filters this effect has a considerable effect (for example when working with a R-I passband).

Visible light is more readily scattered from dust and mist (Mie scattering) and partly from small molecules (Rayleigh scattering). **Scattering** causes the electromagnetic radiation to be redirected from its original path. This effect is more known as Air Glow, and its resulting stray light has a significant effect on optical performance.

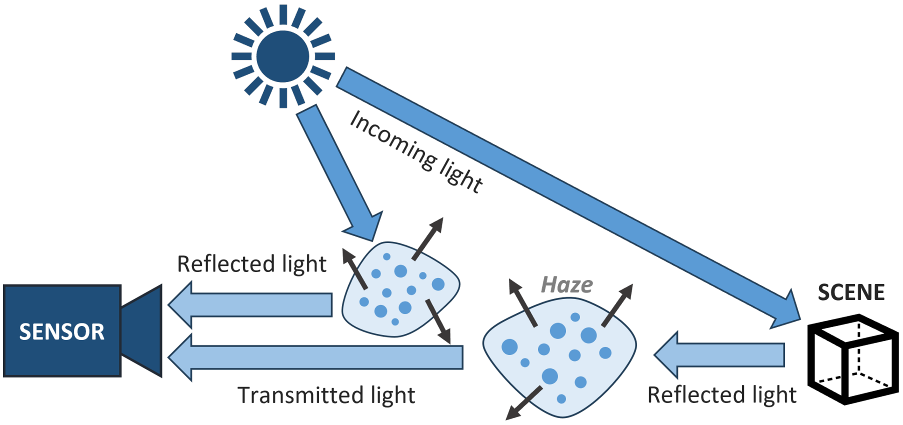

Figure 23: Scattering phenomena from small particles - schematic

Akin to Atmospheric refraction, variations of density within the atmosphere cause both intensity fluctuations and refractive index variations. Combined, these two effect cause smearing and shifting of apparent position, and are known as **Seeing** phenomena.

Combined, these three effects form the **Scintillation** phenomena, which results in a degree of unpredictability when measuring apparent magnitudes, colour, and positions of celestial objects.

2.3.2 Sensor-related errors

Digital imagers are affected by a variety of noise sources that significantly affect performance and need to be addressed. A comprehensive list of these effects would include (Per *Konnik 2014* [8]):

- **Shot noise:** the photon-capture process within the photo-diode has an inherent uncertainty due to the random fluctuations of photon arrival events. This effect is particularly important for low-light conditions.
- **Readout noise:** is caused on the amplifiers that convert the stored charge of each photo-diode pixel into an analog voltage. This noise is compounded by reset noise, dark current noise and fixed pattern noise.
- **Reset noise:** this effect is caused by the uncertainty of the reference voltage at which the sense node capacitor is set to prior to performing the pixel's charge packet measurement.
- **Dark Current (DC) noise:** also known as thermal noise, this effect is randomly generate by the thermal spillage in the pixel well, which releases a higher number of free electrons proportionally to the sensor temperature and exposure time.
- **Fixed Pattern Noise (FPN):** this effect is caused by minute differences in sensitivity across the pixel array, and is composed by a the dark signal non-uniformity (DSNU) and photo response non-uniformity (PRNU) components.
- **Quantization noise:** this error is artificially introduced in the digitization of the analogue signal, and is caused by the data discretization to fit within the integer limit.

We shall analyze these effects further by isolating them through calibration imagery in section 3.6.5.

Individual pixel defects are also commonly witnessed in COTS hardware with longer life cycles, especially if often exposed to high-energy particle events. A comprehensive breakdown and analysis of these defects is presented in Section 3.7.

2.3.3 Scenario-related errors

Background noise is commonly used to refer to the incoming light from an apparently empty section of the night sky. Even though no astronomical objects are detected in the FOV, we detect a baseline signal amounting to around 22 in the apparent magnitude scale. This signal is a compound phenomena made up of multiple sources, including:

- **Air Glow** due to the diffusive and scattering presence of the atmosphere
- **Light Pollution** from man-made sources
- **Zodiacal Light** caused by diffuse sunlight scattered by interplanetary dust.
- **Undetectable point-like sources** such as faint asteroids, galaxies or stars.

In optical system's design, **Stray Light** is any light source that was not intended for capture. These photons are usually reflected off of atmosphere or planetary bodies, with the highest contributors being the Moon and Jupiter. In some situations, the Earth itself can be a considerable staylight source, especially for space-based sensors orbiting over the polar regions, where albedo is higher. Straylight from air glow or the sun is also extremely relevant and require dedicated hardware and software suppression techniques. Much of telescope system design is oriented in the prevention of this straylight, often resulting in multiple-mirror designs supplemented by baffles, which help to significantly attenuate this phenomena.

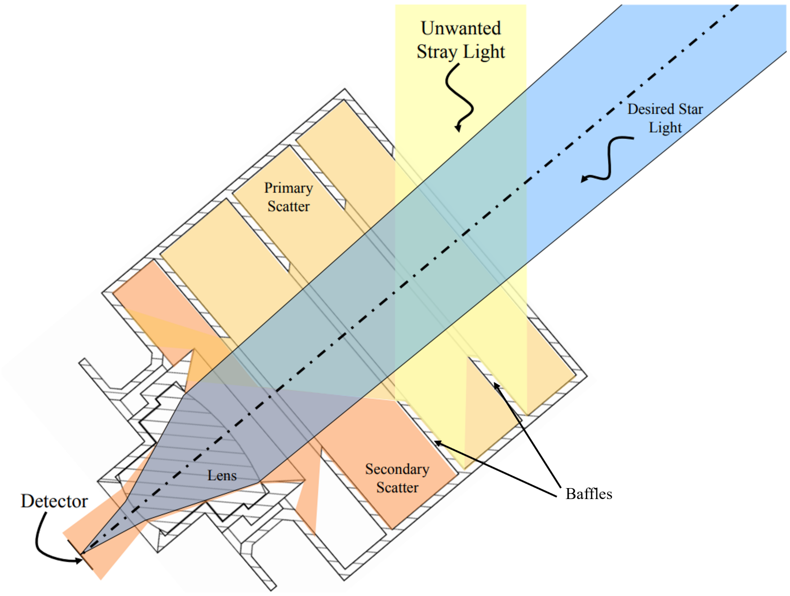

Figure 24: Baffle design for Stray Light suppression (from *Marcinian 2014* [9])

3 Image Simulator

3.1 Overview

In this chapter we shall discuss the implementation of the Image Simulator developed to test the on-board software for the SBOC project. Within this chapter we will go over the methodology, the architecture and the models of the simulator to provide the reader with a full run down of the logic behind its development.

For the image simulator we have outlined the following design drivers:

1. Modular design
2. Flexibility in feature implementation
3. Realistic simulation
4. Statistically-driven
5. Cross-validated through ART imagery

These drivers shall be kept into consideration throughout the entire development, to facilitate their implementation.

3.2 Architecture

To comply with the first two requirements, the simulator features a Object Oriented Programming approach, where input parameters and functions are grouped together into different classes.

We identify the following classes within the architecture:

1. **Main Synthetic Image** class: is responsible to handle the main image assembly process and contains essential data for output data generation.
2. **Detector Parameters** subclass: contains and processes data for process noise, defective pixels, timing errors and QE conversion.
3. **Telescope Parameters** subclass: contains the intrinsic properties of the telescope, and is responsible for generating vignette and distortion maps.
4. **Observation Scenarios** subclass: processes the star and object catalogue data and contains necessary input data to represent these features according to FOV and exposure time.
5. **Platform Parameters** subclass: handles data to simulate vibration of the gimbal during tracking and surveillance scenarios.

Inputs for these classes are stored in an internal *.json* file.

External software data is collected from the internal Airbus' TRACES tool for generating cosmic ray maps, the GAIA DR2 catalogue of visible stars and the SPOOK feature propagator (proposed for a future upgrade). The image below displays a comprehensive breakdown of the class structure within the simulator.

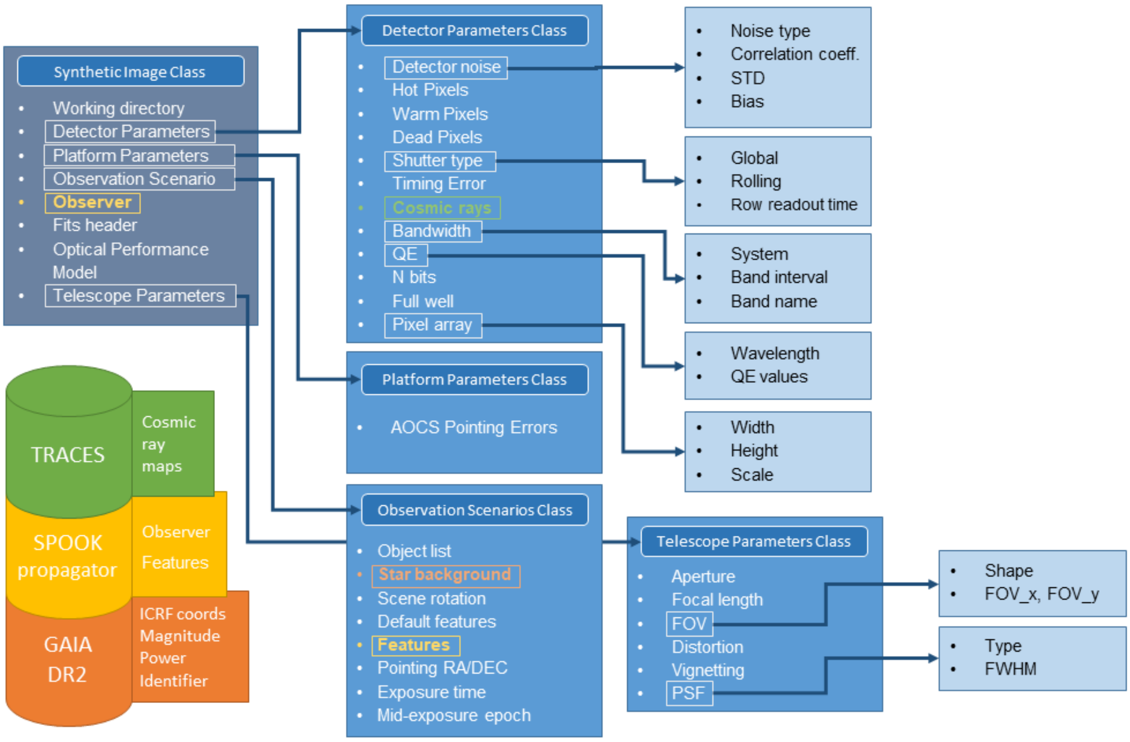

Figure 25: Class system breakdown of the image simulator

Relevant python packages featured in the model include *scipy* for statistical processing of noise data and *astropy.WCS*, used extensively for reference systems conversion across multiple standards.

3.3 Modelling approach

The image simulator operates on the philosophy of reconstructing all phenomena affecting the path of a photon as they appear in real life. This "photon-path approach" allows us to segmentate the phenomena in a sequence, since order of application matters in terms of obtaining a final result consistent with real imagery.

We have distinguished seven critical steps that affect image reconstruction:

1. Projection method
2. Source phenomena
3. Atmospheric effects
4. Telescopic interactions
5. Exposure phase
6. Conversion phase
7. Post processing phase

From these, we can identify and insert error sources according to their position within this analysis method.

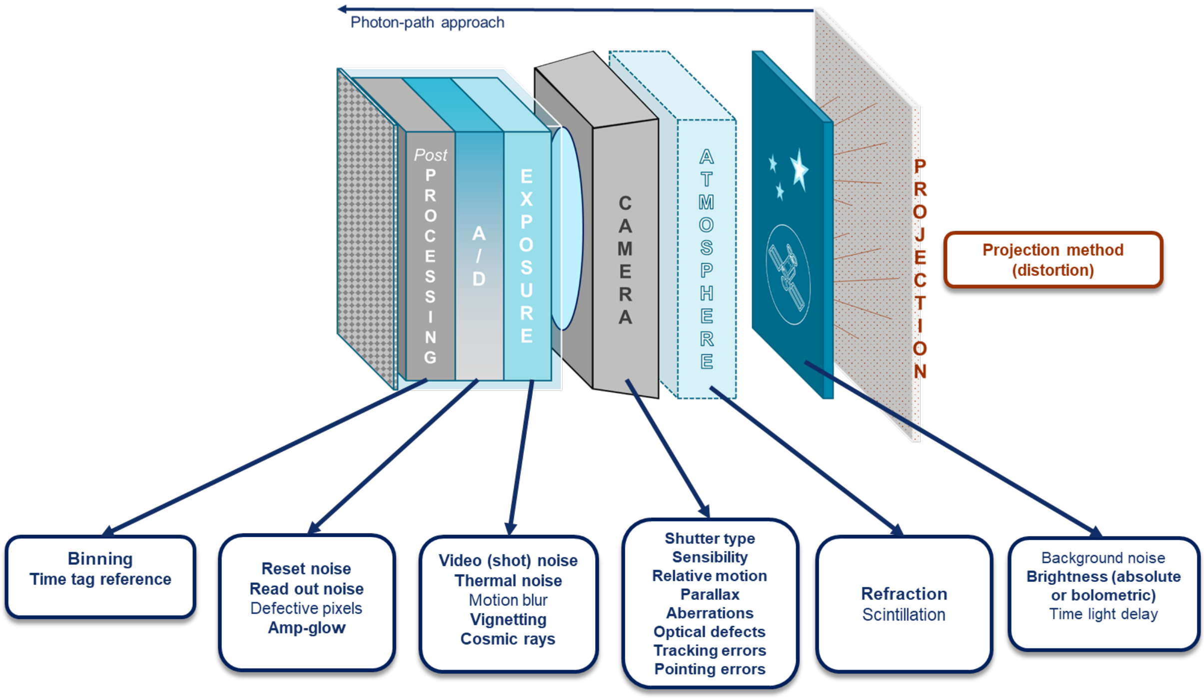

Figure 26: Block representation of the modelling principle for the Image Simulator

Reconstruction of these phenomena is possible through a backwards analysis of these effects, where we start from the image output, and build our model retracing the steps back to the original source.

To handle the variety of inputs a pipeline for data handling has been implemented, with the following structure:

1. Raw object data: containing inputs regarding object and telescope position, distances and phase angle.
2. Magnitudes: provided as an input, is used to represent star and sky background data.
3. Signal Power [photons]: star data is processed through exposure time and star temperatures, with straylight data also being introduced in this step.
4. Total Signal Power [photons]: previous sources are converted utilizing pixel dwell time, and poissonian noise sources are applied.
5. Total Signal Power [electrons]: utilizing quantum efficiency curves, intrinsic sensor noises are introduced.
6. Pixel Signal [electrons/pixel]: signals are converted to fit within the 2D focal plane array, by introducing FWHM/EE conversions for PSF application.
7. ADU: all signals are converted into digital units, with bias and pixel defects being implemented.
8. ADU correction: final adjustments are performed based on binning requests and bit depth (to perform ADU threshold for saturation). The image is then saved according to the provided file format.

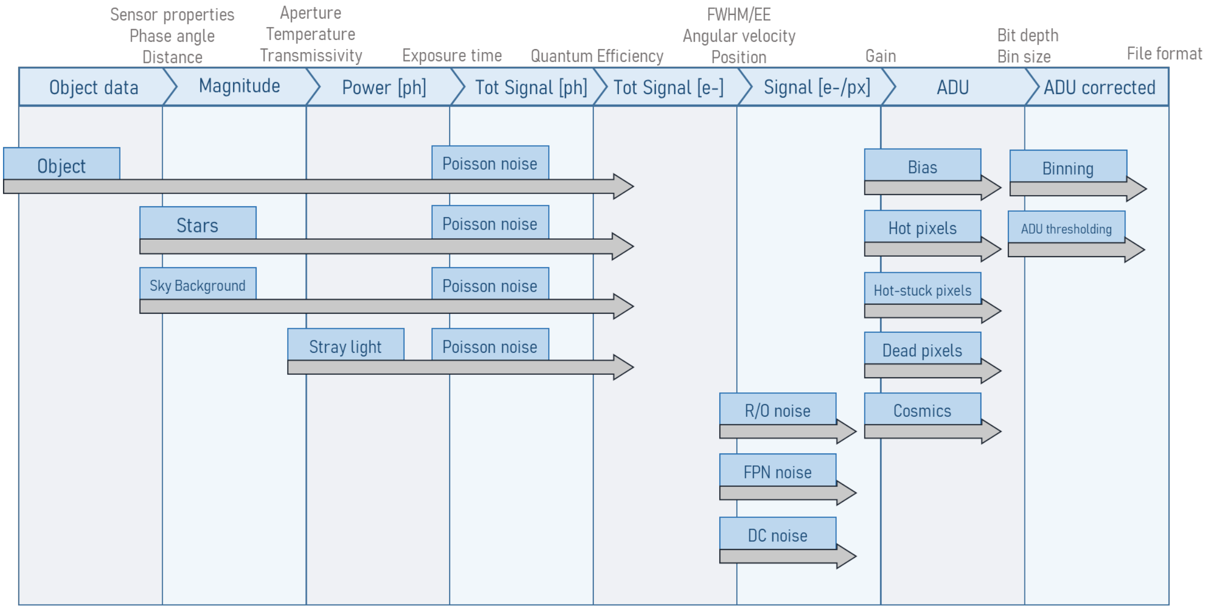

Figure 27: Process flowchart for simulation input data handling

3.4 Feature representation

To create both point and streak features, it's necessary to define a method to convert celestial coordinates onto the sensor's focal plane.

To achieve this, we define the point source coordinates through RA/DEC coordinates in the ICRS coordinate frame system, where we convert them to the GCRS frame (which considers earth's centers of mass instead of the solar system's barycenter) to correct for aberration and parallax displacements. This operation is entirely performed by the *astropy.wcs* package, which contains multiple utilities for coordinate conversion and focal plane representation.

At this point we have to consider that when performing observations on point sources, a diffraction and aberration pattern will be produced on the sensor matrix. This series of concentric rings around a central brightly illuminated region is known as an *Airy disc* pattern. The energy distribution within this pattern can be modelled through *Point Spread Function* (PSF), a more general term to describe the sensors' impulse response for a single point source.

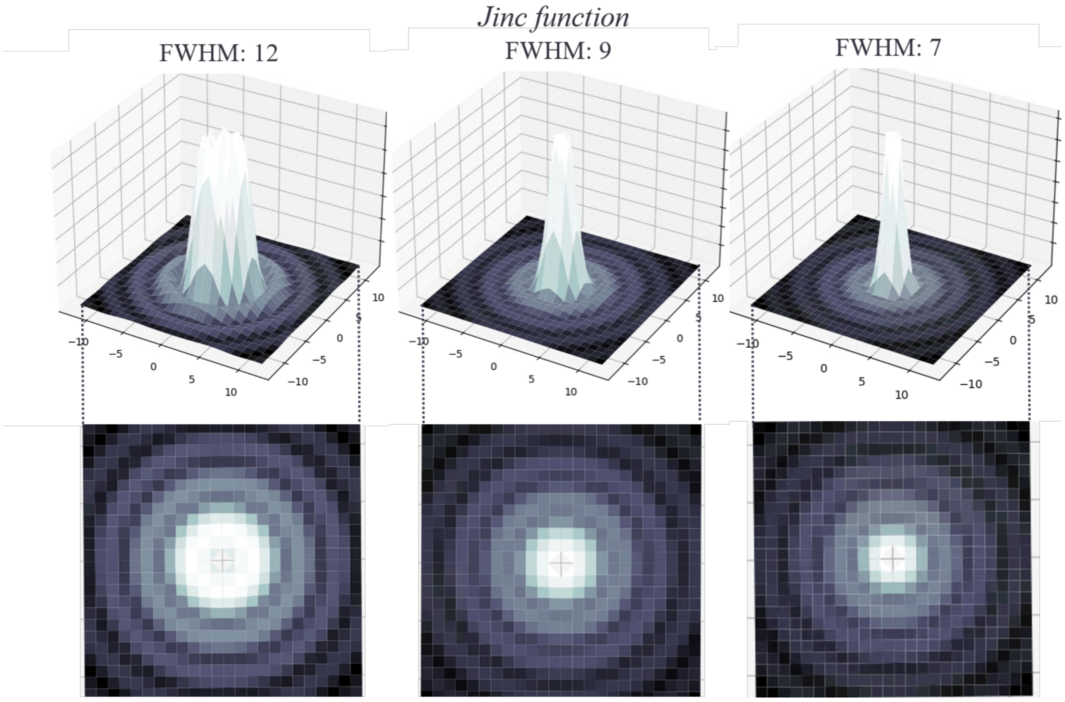

Figure 28: Airy disc representation using Jinc function, log-normed color scale

Within the image simulator, an approximation for the Airy pattern must be modelled in order to represent both streaks and stars. More complex modelling through the first-order Bessel functions can be computationally intensive, so a compromise must be reached by only modelling the central lobe of the distribution through the use of a Gaussian 2D distribution. To find the right parameters, we utilize the definition of FWHM addressed in annex II, to calculate the STD of the distribution:

$$\sigma_{normal} = \frac{FWHM}{2\sqrt{2\ln 2}} \tag{4}$$

With these initial assumptions we can begin working with stars, which within our model we assume to be point-like sources.

3.4.1 Star representation

The GAIA database, curated by the European Space Agency, provides astrometric, photometric and spectroscopic data on almost 2000 million stars in the Milky Galaxy and other extra-galactic objects. The objects' information is sorted by position, parallaxes, relative motion and apparent magnitude measurements. By filtering through the database for RA, DEC, and a limit magnitude for which $SNR = 1$, we store the data in a smaller local database of almost 30k stars, with magnitudes ranging from 20 (faintest) to 5 (brightest). For calibration and conversion purposes, brightness is calibrated using the Vega star as a magnitude zero baseline. To avoid using an excessive number of barely visible stars, for testing purposes we usually limit the lower bound to a magnitude of 18.

In addition to magnitude data, we store the effective temperature values provided from the GAIA catalogue. Alternatively, these can be obtained from Ballestero's formula under the black body hypothesis:

$$T_{eff} = 4600K\left(\frac{1}{0.92(BV)+1.7} + \frac{1}{0.92(BV)+0.62}\right) \tag{5}$$

Where B-V is defined as the range of wavelengths between the blue and visual magnitudes in the spectrum.

We apply Planck's law to model stars as black bodies, which allows to calculate the spectral radiance emitted at a determined temperature and frequency.

$$B_\lambda(\lambda, T) = \frac{2hc^2}{\lambda^5}\frac{1}{exp(\frac{hc}{\lambda k_B T}) - 1} \tag{6}$$

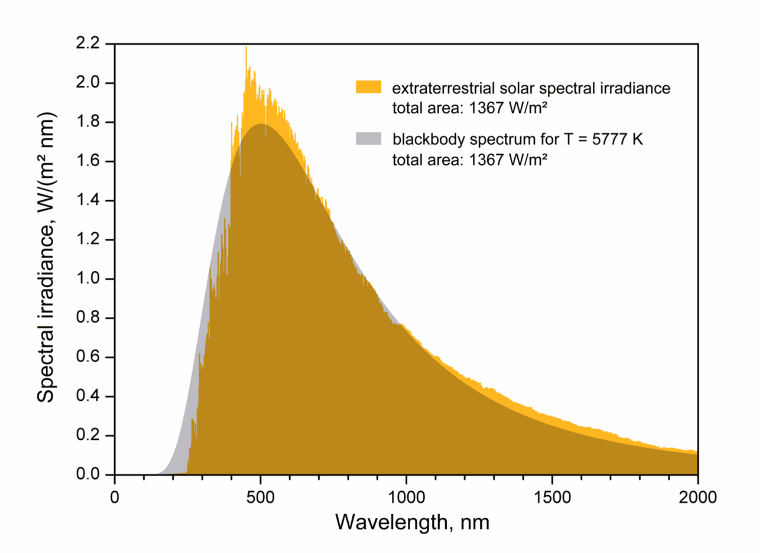

Figure 29: Spectral irradiance and its blackbody approximation, from T.C1 of [10]

From Figure 29 we can evaluate the quality of the black body approximation, which must return the same total emissive power as the Sun spectrum. By integrating across the visible range spectrum, we obtain the effective irradiance of a given star $L_{star,eff}$ in $\left[\frac{W}{sr \cdot m}\right]$. At this point, one can calculate the signal, that is the electrons detected by the sensor across the entire pixel range, as:

$$N_e(\lambda, T) = \frac{L_{star,eff} \cos{(LOS)} A_{aperture}}{\left(\frac{hc}{t_{int}}\right)} \tau_0 \Omega_{star-obs} \tag{7}$$

Where we take into account the aperture, the LOS angle w.r.t. the stellar body, the integration time, the transmissivity τ_0 and the solid angle $\Omega_{star-obs}$.

3.4.2 Streak representation

When a signal is moving across the focal plane during the exposure phase, a streak-like image is picked up on the output. Real streaks are often completely straight, with non-linearities introduced from gimbal vibrations during tracking. Integration time, focal plane velocity and signal intensity consistently affect how the streak is rendered.[11]

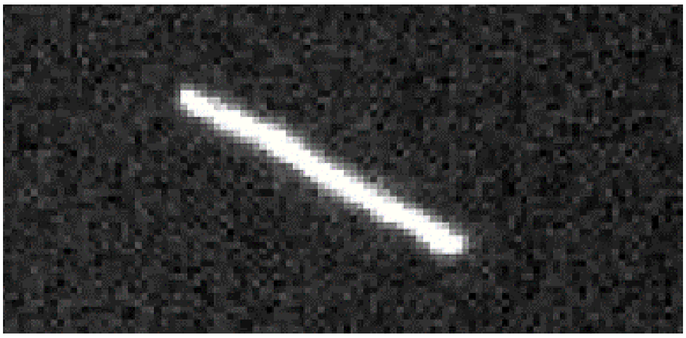

Figure 30: Streak affected by vibrations during tracking

To represent linear and curved streaks, we utilize the discretized streak positions to interpolate a cubic spline, from which it is possible to sample any intermediate position on which to apply our PSF. After an adequate number of intervals is established, the PSF is applied to the edges and centers of these linear segments, creating a semi-continuous set of diffusion models.

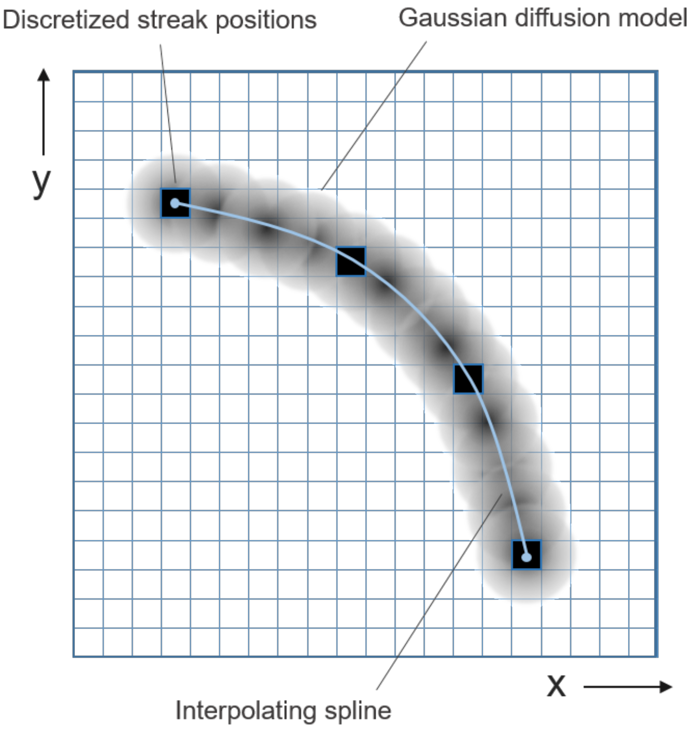

Figure 31: Streak representation - schematic

The denser the discretization, the smoother is the final result. Since streak energy is conserved, the diffusion models are summed additive for each time frame they are rendered, as shown in Figure 32.

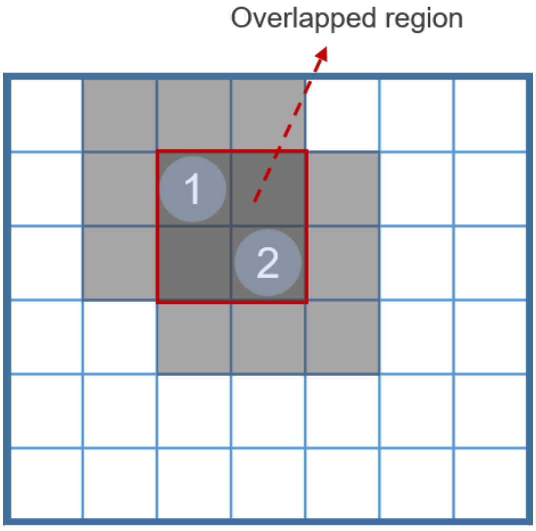

Figure 32: Overlap phenomena in PSF application - schematic

For the diffusion diffusion model, we shall use again 2d normal distribution to approximate the Airy disc pattern, using the formula:

$$f(x,y) = \frac{N_e}{\sqrt{2\pi}\sigma} exp\left(-\frac{(x-x_0)^2+(y-y_0)^2}{2\sigma^2}\right) \tag{8}$$

Where x_0, y_0 are the center coordinate values of the distribution, obtained by evaluating the spline function at the various intervals, and N_e is the star flux of electron numbers detected on the imaging detector, calculated by integrating across the visible bandwidth:

$$N_e = \int_{\lambda_1}^{\lambda_2} \tau_0 \cdot M_\lambda \cdot A_{aperture} \cdot QE \cdot t_{int} \cdot \mathrm{d}\lambda \tag{9}$$

Win M_λ being the star radiation within the provided wavelength range and τ_0 is the transmissivity of the entire optical system.

3.4.3 Rolling shutter corrections

The shutter of a camera is the component that allows light to enter within the aperture. Shutter controls the exposure time of the image and, in the case of most CMOS sensor this exposure takes place sequentially, one row at a time.

Consequently, during the integration time of the sensor, moving objects experience a shift in their centroid position and length, depending on angle and apparent focal plane velocity.

In the case of sequential row readout, horizontal streaks will not experience any length variation, because the readout happens to "catch" the entire streak during at the same time, whereas vertical streaks experience the most offset in centroid position since the readout process encounters them at varying time intervals.

If we segmentate the streak on multiple time intervals, we can operate directly on the centroids associated with each interval. Two main approaches are known to be utilized to correct for the centroid shift, both explored within *Kukić2018* [12]:

- **Spatial corrections** require estimation of angle and focal plane velocity prior to the rolling shutter effects. In this case one can perform a correction on the location of the centroids of the streaks, but not on the time of integration.
- **Temporal correction**: operates solely on the time stamps of each centroid, by performing a correction on the time of integration and associating this time variation to a spatial variation on the Y axis.

The latter method is much more straightforward, and requires only that we calculate a time offset relative to the reference time stamp. If we assume the middle of integration (for an individual streak interval), we can calculate the time delay between the start of an individual time frame (shown here as t'_{frame}) as[12]:

$$t'_{frame} = t_{frame} - t_{row} - t_f = \frac{1}{FPS}\left(i_{frame} - \frac{y_i}{n_{rows}} - f\right) \tag{10}$$

where f is defined as $f = t_{exposure}FPS$ and t_f represents the time bias.

A mock model to implement these corrections has been developed, with results shown in the image below.

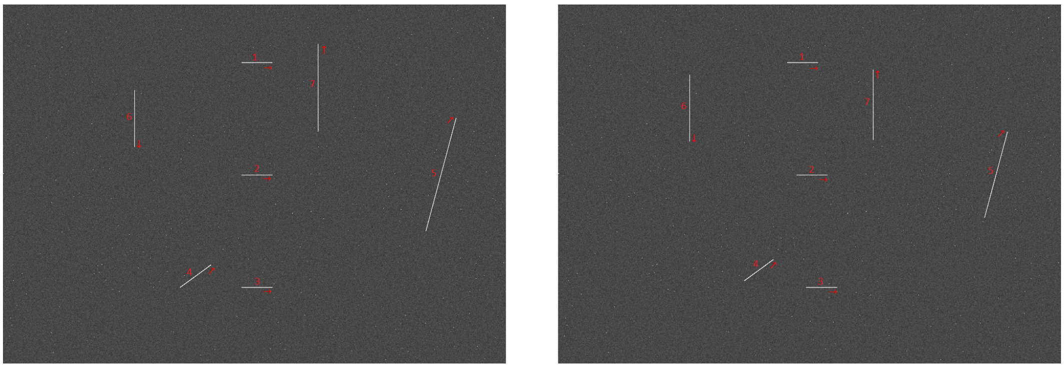

Figure 33: Synthetic images with Global Shutter (left) and Rolling Shutter (right) [4]

As predicted, the horizontal streaks remain unaffected in terms of length, with the two vertical streaks (No.6 and 7) being the ones affected the most.[4]

3.5 Cosmic representation

For space-based observers, one of the most relevant effects is caused by stray cosmic rays hitting the sensor. These high-energy particles (usually atomic nuclei or protons) mostly originate from outside the solar system and can cause an ample spectra of problems. In the case of imaging sensors, the most relevant phenomena is the creation of bright pixel features during the exposure and A/D conversion phases: the particle interacts with the sensor when crossing it, depositing some of its energy within it and excite additional electrons.

To model the energy loss of the particles we use a simplified version of the Bethe Bloch equation for heavy particles, in our case only the protons:

$$S(E) = -\frac{dE}{dx} = 2K\rho\frac{Z}{A}\frac{z^2}{\beta^2}\left\{\ln\left(\frac{2m_e c^2\beta^2\gamma^2}{I}\right) - \beta^2\right\} \tag{11}$$

where E is the kinetic energy of the particle, S(E) is its stopping power, Z and A are the atomic properties of the absorbing material, ρ is its density, z is the charge of the particle (=1) and K is

$$K = 2\pi N_a r_e^2 m_e c^2 \tag{12}$$

with $\beta = \frac{v}{c}$ and $\gamma = \frac{1}{\sqrt{1-\beta^2}}$, N_a being the Avogadro number and c the speed of light.

From the formula one can observe how the stopping power is entirely dependent from the properties of the material encountered and by the type of particle. For a LEO object the source of particles originates from the Van Allen radiation Belts, which contain charged particles carried from solar winds that become trapped via the influence of Earth's magnetic field. In the case of the inner belt, the heavy particles are mostly protons, and this belt can extend down to 200 km orbits in proximity of the South Atlantic Anomaly. In this area, ionizing radiation and flux of energy particles are significantly increased, and LEO satellites are exposed to their effects.

After integrating the deposited energy within the size of a single pixel, it's possible to determine the voltage offset using the conversion efficiency:

$$V_{pix} = \frac{C_{eff}E_{dep,pix}}{w} \tag{13}$$

where w is the energy necessary to create one electron-hole pair. This voltage offset influences the A/D conversion and causes higher ADU values in output.

To simulate shielding, we simply replace the material properties of silicon with those of either aluminium or copper, and begin our calculation by initially subtracting the stopping power integrated over the width of the shield.

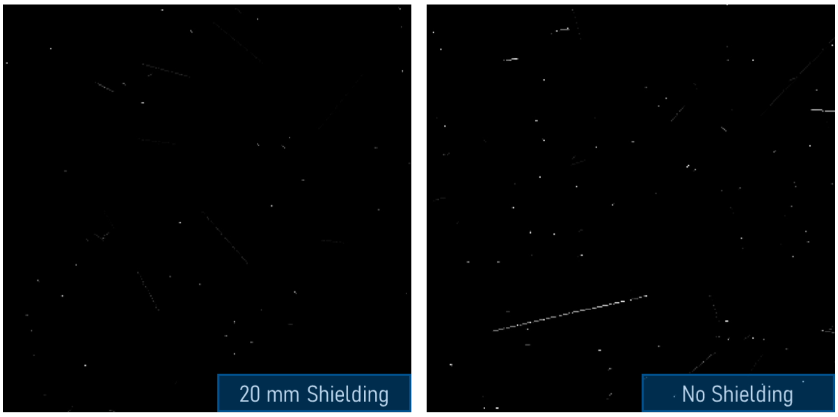

Figure 34: Generated cosmics maps under intense flux conditions inside the SAA

3.6 Optical performance model

Solid-state photosensors such as CMOS or CCDs are subject to a multitude of noise sources, both originating from atmospheric effects or from sensor imperfections. To limit and estimate the impact of these noises on the sensor, we simulate this effects within the pipeline. It is important to distinguish in two categories these phenomena: event-dependent Poisson noises and event-independent Gaussian noises. If we classify a photon entering a pixel well as an event, we can identify potential sources for our optical performance model.

DISCRETE SOURCES

- **Stars**, brighter than a magnitude threshold
- Radiance from **Planets** and **Planetoids**
- Reflected and thermally emitted light from **Satellites**

Discrete sources constitute a severe limitation when observing in anti-sun and anti-planetary directions (angle of LOS $< 90°$), and while baffle design can help mitigate the phenomena, the effects can still have a serious impact on SNR calculations.

CONTINUOUS SOURCES

- **Zodiacal Light**, sunlight scattered by interplanetary dust on the ecliptic plane in proximity of the Sun
- **Galaxies**, assumed as a continuous source due to their large number and angular dimension
- **Airglow**, caused by chemiluminescent reactions occurring within the Thermosphere.
- **Scattered light**, i.e. the radiance from planets or stars scattered by atmospheric molecules.

These sources, while easier to approximate, can be very hard to model individually, so for the purposes of this simulator they will be treated as background continuous sources, taking only their absolute magnitude into account.[13]

3.6.1 SNR model

SNR can serve as a useful parameter to determine signal detection in astrometric imagery. SNR can be simply represented as:

$$SNR = \frac{N_{signal}}{\sqrt{N_{signal} + N_{straylight} + N_{noise}}} \tag{14}$$

This will serve as the basis for the model, and we shall investigate how to determine both operands. For the signal power component, we must determine the signal entering a single pixel. This signal can be divided in two: reflected and thermal.

The thermal signal component is simply the emitted range of electromagnetic radiation from a body in thermal equilibrium. If we consider the object to be a black body, we can calculate the updwelling radiance by integrating Planck's law across the whole range of visible wavelengths:

$$B_\lambda(\lambda, T) = \frac{2hc^2}{\lambda^5} \frac{1}{exp(\frac{hc}{\lambda k_B T}) - 1} \tag{15}$$

For an object in LEO, which we consider to be at a temperature of 290K, the radiance emitted is almost negligible, whereas the dominant effect is represented by the reflected radiance.

We can calculate the solid angle by dividing the disc area of the sun by the square of the distance to the object:

$$\Omega_{sun-obj} = \frac{A_{sun}}{R^2_{sun-obj}} [sr, steradian] \tag{16}$$

One can calculate the reflected energy from the sun irradiance L_{sun} calculated through the same technique as above:

$$E_{reflected} = L_{sun}(\lambda) \cdot \Omega_{sun-obj} \cdot \Omega_{obs-obj} \cdot p \cdot \theta_F \tag{17}$$

Where p is the albedo of the object and θ_F is the phase integral function [13] provides functions for a diffuse-specular model for a sphere, where through the use of a mixing coefficient β one can determine the surface response for reflection. These models are expanded upon in Annex III, along with phase functions for a tumbling plate-like object.

We can now compute the powers transmitted across the whole aperture:

$$P_{reflected,aperture} = E_{reflected} \cdot A_{aperture} \cdot \cos(angleLOS) \tag{18}$$

$$P_{thermal,aperture} = E_{thermal} \cdot A_{aperture} \cdot \cos(angleLOS) \tag{19}$$

and sum them together to obtain the $P_{tot,aperture}$. This power can be reduced by the trasmittivity factor τ_0, and we deduce the deposited energy from:

$$E_{deposited,aperture} = \tau_0 P_{tot,aperture} \cdot t_{pixeldwell} \tag{20}$$

An approximation for the pixel dwell time is provided in Annex VI. At this point it is straightforward to compute the number of photons (i.e. the signal) by dividing the deposited energy by the energy carried by a single photon:

$$N_{photons} = \frac{E_{deposited}}{E_{photon}} = \frac{E_{deposited}}{\left(\frac{hc}{\lambda_{ops}}\right)} \tag{21}$$

3.6.2 Stray light model

Suppression of unwanted sources (Stray Light) is a critical topic in telescope design, since these sources will reduce the image quality and contrast. So-called "baffles" are conical structures designed to prevent unwanted photons from entering the sensor, through shading, occulting and shielding direct radiation for off-axis angles. For large off-axis angles, *"vanes"* play a critical role in reducing the scatter characteristics of the baffle, and are mounted directly on the interior of the baffle. Proper design and combined use of these two structures can help reduce straylight by several orders of magnitude.[14]

To estimate straylight within our model, we must calculate the irradiance at the operating wavelenght that is hitting the telescope:

$$E_{0,sun}(\lambda) = L_{sun}(\lambda) \cdot \Omega_{sun-obs} \tag{22}$$

From which we can calculate the signal power hitting the baffle, if LOS with the sun is smaller than 90 degrees (anti-sun pointing).

$$P_{straylight} = \begin{cases} A_{baffle} \cdot E_0(\lambda) \cdot \cos(LOS), & \text{if } LOS_{sun} < 90, \\ 0, & \text{otherwise.} \end{cases} \tag{23}$$

The same equations can be used for other celestial bodies, using their albedo and disc area to calculate the reflected light. For example, using the formulas seen in 3.6.1 and III, one can calculate the irradiance projected off the Moon and include it within the model. To extrapolate data necessary for the noise simulation, it's necessary to include the baffle mitigation and calculate the average number of photons entering each pixel:

$$P_{straylight,pxl} = \frac{P_{straylight}}{N_{pix,x}N_{pix,y}} \cdot \tau_{baffle} \tag{24}$$

Where τ_{baffle} is the stray light attenuation factor of the baffle. To find the number of photons, this time we utilize the integration time (instead of dwell time) and we divide by the energy of a single photon.

$$N_{p,straylight} = \frac{P_{straylight,pxl} \cdot t_{int}}{\frac{hc}{\lambda_{op}}} \left[\frac{photons}{pixel}\right] \tag{25}$$

3.6.3 Background noise model

Background noise will constitute a major noise source, but it is extremely difficult to model efficiently. Unlike straylight, it's impossible to point to a unique contributor for the whole phenomena, and instead there are multiple atmospheric phenomena that might cause it, such as Zodiacal light, Air Glow, Light pollution or other atmospheric disturbances. Accurate representation would require real-time overhead data on most layers of the atmosphere, which is not available for ART. At any rate, such a model would go beyond the requirements of the project, so we decide to provide as an input either background magnitude or irradiated energy. For the latter, we can obtain the magnitude:

$$m_{background} = m_{0,sun} - 2.5 \log \frac{E_{background}}{E_{0,earth}} \tag{26}$$

Instead, if the magnitude of the background is provided as input -such is the case within the image simulator- the irradiance at observer aperture can be calculated:

$$E_{aperture} = E_{0,earth} \cdot 10^{\left(\frac{m_{bkg} - m_{0,sun}}{-2.5}\right)} \tag{27}$$

where the apparent magnitude of the sun viewed from Earth is equal to $m_{0,sun} = -26.74$. Again, we compute the number of photons entering the aperture:

$$N_{p,aperture} = \frac{E_{aperture}}{E_{photon}} = \frac{E_{aperture}}{\frac{hc}{\lambda op}} \left[\frac{photons}{m^2 \cdot s \cdot arcsec}\right] \tag{28}$$

Finally, we need to account for transmissivity losses and convert the dimensions into photons per pixel:

$$N_{p,background} = A_{aperture} \cdot \tau \cdot IFOV^2 \cdot N_{p,aperture} \left[\frac{photons}{pixel}\right] \tag{29}$$

3.6.4 Noise model

Now that there is an established algorithm to compute photon counts, we can introduce a model for these event-dependent noise sources. We shall utilize the Poisson PDF:

$$f(k;\lambda) = \frac{\lambda^k e^{-\lambda}}{k!} \tag{30}$$

Which in python can be applied through the method *numpy.random.RandomState.poisson()*, after we initialize a seed. Using Quantum Efficiency for a specific operating wavelength, the conversion to electrons is straightforward:

$$N_e(\lambda) = N_{ph} \cdot QE_{\lambda} \tag{31}$$

At this point, one can begin introducing the noise sources intrinsic to the sensor, which scale independently from the pointing scenario. Normally, Readout (RO), Dark-Current (DC) and Fixed-Pattern (FP) noise estimates are provided by the manufacturer, or can otherwise be estimated through calibration images. These sources are normally provided in standard deviations of $[\frac{e-}{pixel}]$, except for DC-rates, which are provided in $[\frac{e-}{pixel \cdot s}]$, since they scale proportionally to exposure time. If not expressly indicated within the user manual, these values and their distributions can be approximated as in section 3.6.5, through analysis of calibration frames.

In the case of quantization noise, it's effect is easily replicable, since it's caused by truncation and rounding errors when performing A/D conversion. We can derive the STD from the formula:

$$\sigma_{quantization} = \frac{N_{fullwell}}{2^n \sqrt{12}} \tag{32}$$

Where n is the bit depth of the system.

Finally, for brief exposure times, a type of white noise known as reset noise might be relevant, if correlated double sampling techniques are not implemented. The readout diode is brought to a specific reference voltage before reading out the packet, creating an artificial noise: [15]

$$\sigma_{reset} = \sqrt{\frac{k_b \cdot T}{C_{SN}}} \tag{33}$$

C_{SN} represents the sense node capacitance [F] of the readout diode. These noise sources can be combined to obtain the global noise of the system in electrons at readout:

$$\sigma_{tot} = \sqrt{\sigma_{RO}^2 + \sigma_{reset}^2 + \sigma_{quantization}^2 + \sigma_{FPN}^2 + DC_{rate} \cdot t_{exp}} \tag{34}$$

It's important to note that the only outlier is represented by the dark current (thermal) noise, since it's the only system noise that scales with exposure time, and the DC rate itself can vary greatly under different cooling conditions.

3.6.5 Calibration frames analysis

So far the noise model has been implemented under the assumption that the distributions acting on the electrons are normal. To verify these claims we shall conduct a brief characterization of the sensor, through analysis of the calibration frames.

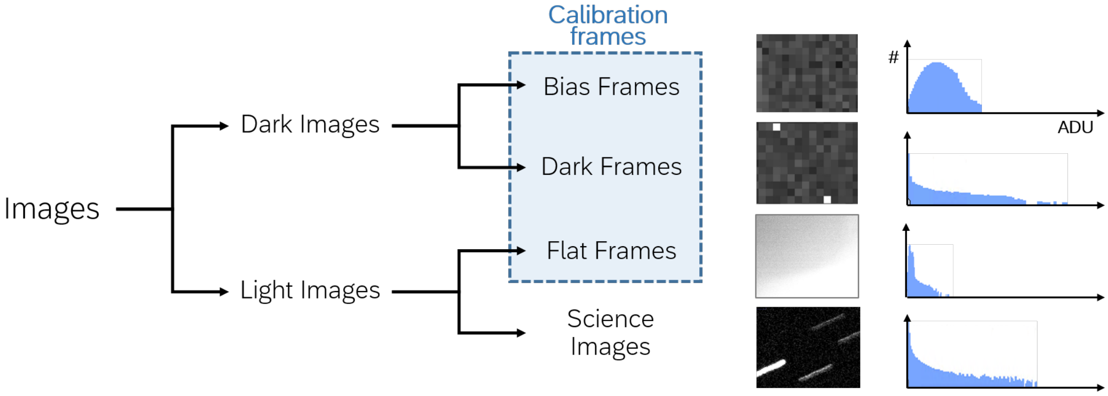

Figure 35: Taxonomy of Image Types

We distinguish a variety of frames used for astrophotography calibration purposes[16]:

- **Bias frames**: Captured at the lowest possible exposure time, with the shutter closed. They represent the sensor response in the readout phase, in absence of any signal.

- **Dark frames**: Can be taken on a variety of timed exposures and temperatures, with the shutter closed. They permit the measurement of the dark current response due to thermally released electrons during exposure.

- **Flat frames**: Through use of a diffuse and uniform light source in the FOV, flat frames are taken at various exposure times and with the shutter open. They can help calibrate the photosensitivity of individual pixels and determine the associated noise.

Through these calibration frames, one can characterize the sensor behaviour to improve quality of photometric data for our Science Images. However, Flat frames are difficult to replicate and require specialised facilities, so for the purposes of this project they will not be available.

Starting from the bias frames, which are captured at 0.01 seconds of exposure time, we produce an analysis for both the CCD and CMOS sensors. Results show clearly how the newer CMOS sensor considerably outperforms the CCD. The reduction in readout noise is especially considerable when plotting both distributions against each other:

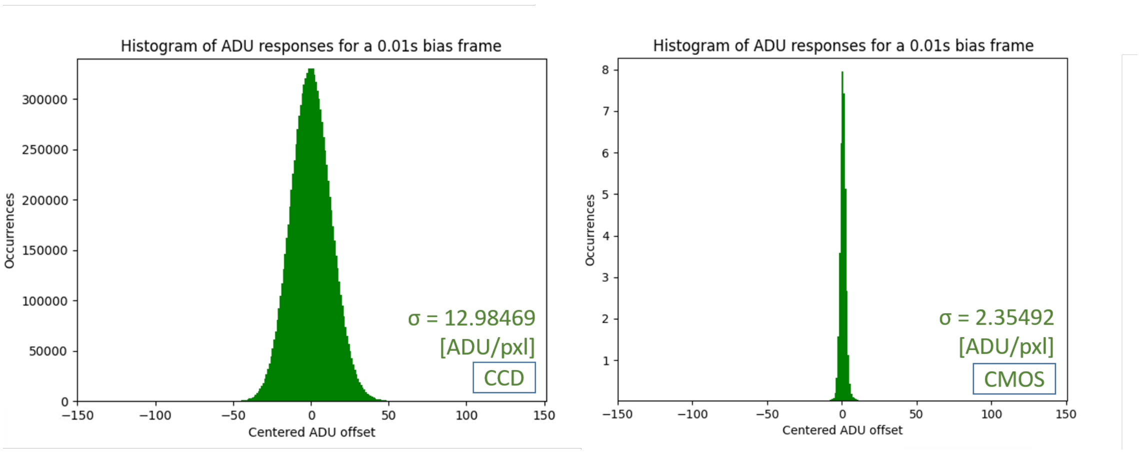

Figure 36: CCD vs CMOS bias frames comparison

The STDs from these calibration frames confirm the manufacturer's specifications, which are actually about 10% larger than the results calculated.

Sensor	Calculated STD	Declared STD
ML 11002	12.98469	14
IMX411	2.35492	2.4

Table 2: Standard deviations for 0.01s bias frames

Additionally, we can test these distributions for normality using the Jarque-Bera, Shapiro-Wilk and Kolmogorow-Smirnow tests (on both sensors). These algorithms operate on the null hypothesis that the sample has been generated from a normal distribution. The p-value of these tests -i.e. the level of marginal significance within a statistical hypothesis test- allows us to assess weather our image sample set has passed the test or not. If $p \geq 0.05$, we fail to reject the null hypothesis, and we assume that the distribution is normal. For performance necessities, we reduce the data-set to 5000 representative samples, and we obtain the following statistics:

Test	Statistic	p-value
Shapiro-Wilk	0.99814	0.29343
Kolmogorow-Smirnow	0.41422	≈ 0.0
Jarque-Bera	1.15100	0.56242

Table 3: Normality test results for CMOS reduced data-set (N=5000)

Both the Shapiro-Wilk and Jarque-Bera reject the null hypothesis and indicate normality, however the dataset does not pass the Kolmogorow-Smirnow test. To understand why the latter test is rejecting our dataset, we can visually analyse the data on a QQ (Quantile-Quantile)-plot, where we plot our data against the theoretical expected results of a normal distribution:

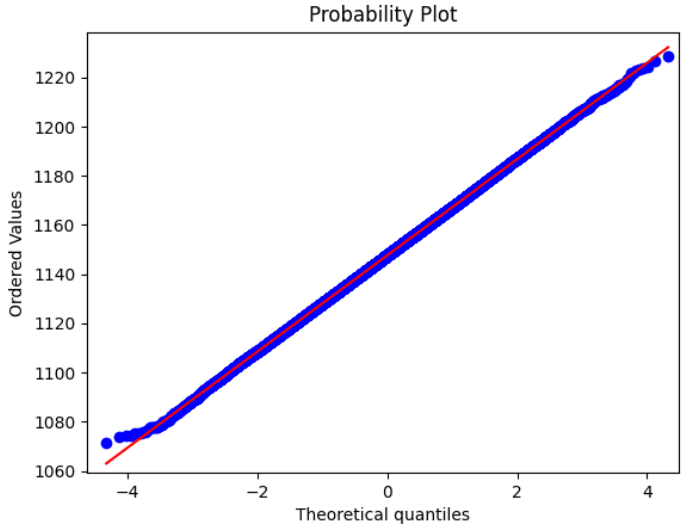

Figure 37: Quantile-Quantile plot

The linearity of the plot suggests that the data is indeed normally distributed, with only a few outliers not falling into that category. These outliers are likely causing the KS test to reject our hypothesis, since it tends to be a much more sensitive test for sample sizes such as ours.

We can then conclude that using a normal model for readout noise distribution is appropriate, and we can continue the analysis by tackling Dark Frames.

As mentioned before, dark frames allow us to determine the dark current response when working with a variety of temperatures and exposure times. In this paper we shall perform analyses on the CMOS sensor at -5,-15 and -25°C cooling conditions, from 5s to 300s of exposure times.

T_{exp} :	5s	10s	30s	60s	120s	300s
$\sigma_{dark}@-25°C$:	2.38	2.55	3.41	4.99	7.85	17.86
$\sigma_{dark}@-15°C$:	2.56	3.03	5.40	8.75	14.13	24.32
$\sigma_{dark}@-5°C$:	3.18	4.45	9.33	14.95	22.51	37.49

ADU/pxl

Table 4: STDs of CMOS calibration dark frames

From the table it becomes noticeable how the standard deviations are heavily influenced by these two parameters, and by plotting the data for 300 seconds into histograms, it is noticeable how the distribution is no longer purely Gaussian, but is now heavy-tailed on the right tail.

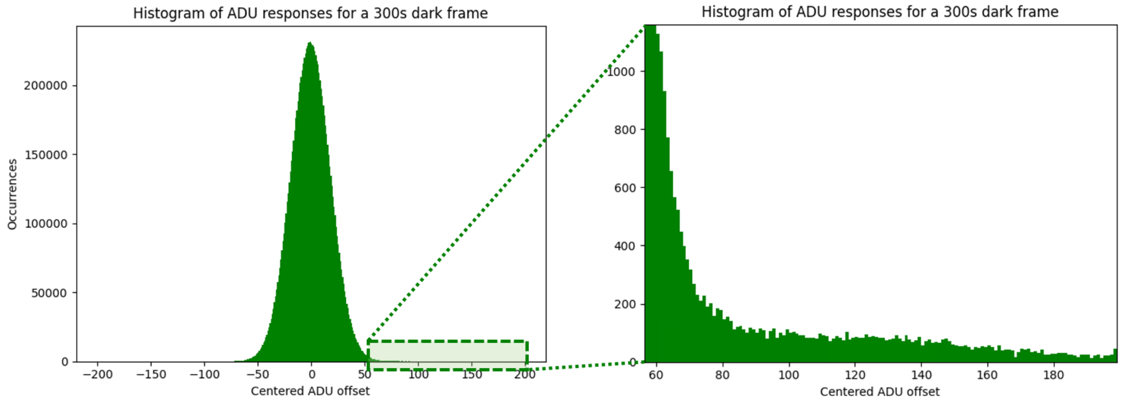

Figure 38: Long tail phenomena in dark frame imagery

Another way to visualize the phenomena, is to plot the data in another QQ-plot, where it becomes clear the skewed-ness of the normal distribution, and the anomalies present for higher ADU values. These outliers are caused by pixel defects which lead to higher dark current rates, and are thoroughly analysed within section 3.7.1.

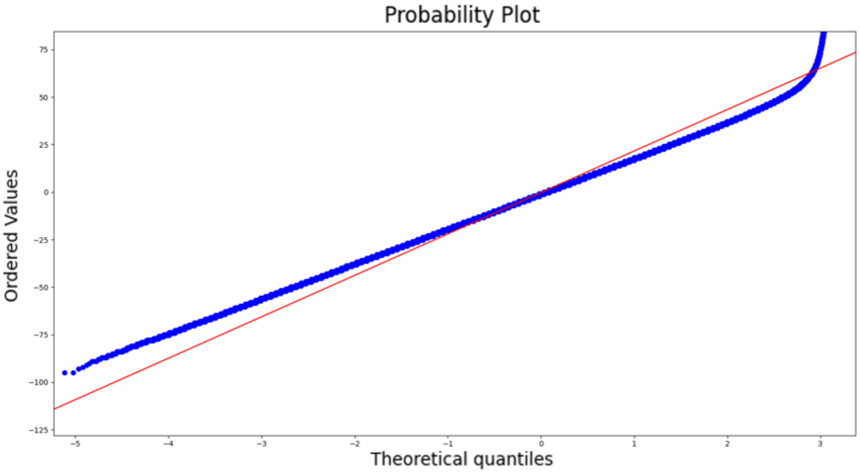

Figure 39: Quantile-Quantile plot of ADU values in a 300s dark frame

In this following paragraph, we shall define as "inliers" the pixel values with $ADU \leq N \cdot \sigma_{biasframe}$ and construct the following hypothesis:

HYPOTHESIS: The dark current rate of inlier pixels remains constant at different exposure times, and the average ADU offset produced shall scale linearly with exposure time, skewing the distribution.

To validate the statement, we conduct an analysis on the following procedure:

1. **Sample data from Bias Frames**
    - → Compute and store Average
    - → Compute and store Bias
    - → Compute and store STD
2. **Evaluate data from Dark Frames**
    - → Subtract Average and Bias to center distribution
    - → Flag pixel values $<$ limit*STD [limit $=$ 3÷10] as inliers
    - → Compute pixel average on inlier pixels for each dark frame
    - → Perform linear regression on averages vs T_{exp}

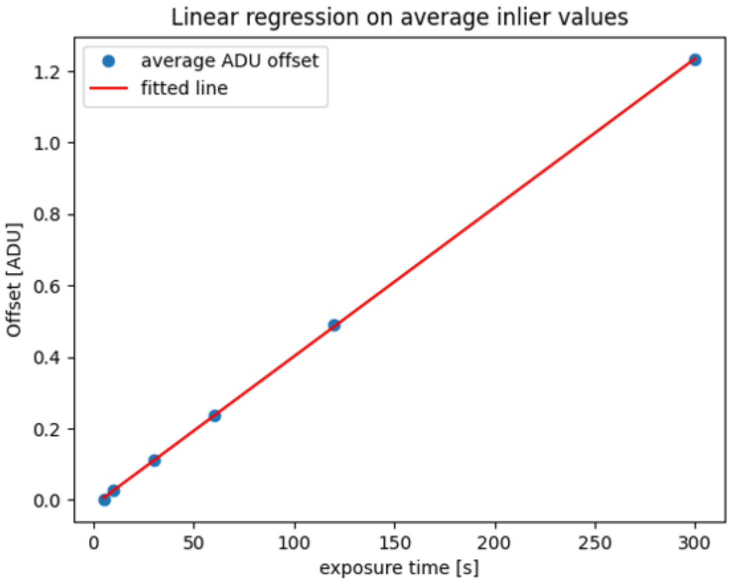

Figure 40: Linear regression on average ADUs @-5°C cooling

Where, in Python, we utilized the method from *scipy.stats.linregress()* to perform a least-squares regression and display the fitted line.

We find that the linear fit is very accurate, and our hypothesis of evaluating averages on inliers is appropriate. The slope of the fitted line corresponds to the dark-current rate (in ADU), which we can evaluate against temperature and sampling conditions:

		STD limit		
		3σ	5σ	10σ
T [°C]	-25	0.003300	0.003399	0.003479
	-15	0.003463	0.003577	0.003685
	-5	0.004168	0.004309	0.004440

$\left[\frac{ADU}{pix\cdot s}\right]$

Table 5: Dark Current rate results for varying cooling and sampling conditions

Through quantum efficiency we can convert these rates into electrons to find that the values are very close to the declared rate of 0.006 $\left[\frac{e^-}{pix\cdot s}\right]$.

3.7 Defective pixels

Experimental results from [17] have demonstrated that CMOS and CCD sensors are affected by a variety of pixel defects, with defect density scaling linearly with time immediately after production. These faults are often caused by high-energy particles, manufacturing and storage processes, and charge leakage. At higher ISO settings and long exposures, these defects become significant enough that they cannot be ignored, and can often result in the saturation of ADU values.

Normally, the behaviour of an ideal good pixel can be modelled simply as a measure of incident illumination which is represented as:

$$I_{pix}(R_{photo}, T_{exp}) = m(R_{photo} \cdot T_{exp}) \tag{35}$$

Where R_{photo} represents the incident illumination rate, T_{exp} is the exposure time, and m is amplification due to ISO setting. However, in the case of defective pixels, additional terms on dark current rate (R_{dark}) and dark offset (b) are now present:

$$I_{pix}(R_{photo}, R_{dark}, T_{exp}, b) = m(R_{photo} \cdot T_{exp}, R_{dark} \cdot T_{exp}, b) \tag{36}$$

To evaluate the behaviour of these faulty pixels, it is necessary to distinguish the different types of defects:

- **Warm pixels** have an illumination-independent component that increases linearly with exposure time, which results in a higher proportional scaling when capturing dark frames. R_{dark} values are non-zero and scale with exposure time, whilst b is still zero.
- **Stuck (Warm) pixels** have both non-zero R_{dark} and b values, and these two terms create a signal that is added on top of the incident illumination. If the offset b is greater than the maximum values determined by the bit-depth of the sensor, then these defects are called **Hot pixels**.
- **Dead pixels** are permanently damaged pixels that do not receive any power and register 0 free electrons. ADU values might not necessarily be set at 0 if bias is applied in post processing.

Experimental results from [18] show that the Hot Pixels to Stuck Hot Pixels distribution is roughly 54/46%. If ADU values are normalized against dark current, and we indicate as 1 saturated values, it is possible to observe the slope characterizing the behaviour of these pixels.

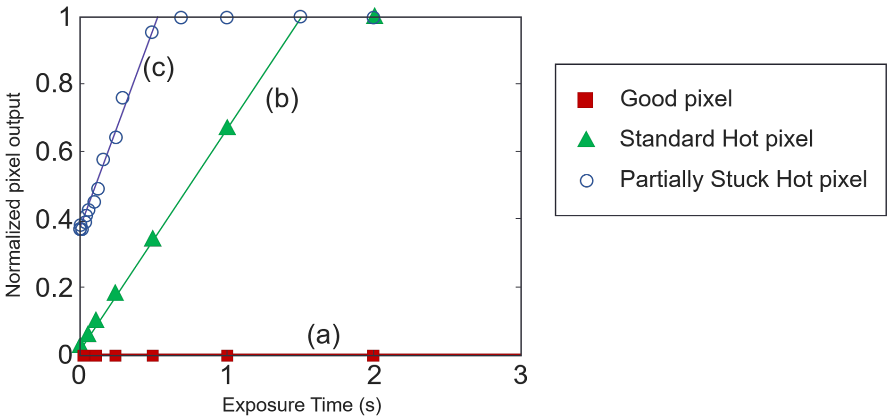

Figure 41: Dark response of defective pixels from [18], upscaled

For what concerns the image simulator, these pixel defects are essential to model, since they can result in a large number of false positives when performing image segmentation for streak identification. Manufacturers normally produce an upper range for the defect density, which can be used to directly simulate worst-case scenarios.

In the model implemented for the simulator we accept as inputs:

- Warm Pixel Density: 1-0 float
- Stuck Pixel Density: 1-0 float
- Dead Pixel Density: 1-0 float
- Time-to-Double (T2D)[s]: max and min int values
- Offset (b)[ADU]: max and min int values

We can model the behaviour of these pixels by directly operating on the ADUs values, where we randomize pixel position, T2D values and ADU offsets. Using ideal pixel values before applying sensor bias, we calculate the defective ADU values:

$$ADU_{defect} = ADU_{ideal} \cdot (1 + \frac{T_{exp}}{T2D}) + b_{offset} \tag{37}$$

If values of ADU surpass the bit-depth maximum limit, values are automatically assigned as saturated and set the maximum value. An explanation of the Seed-based randomization technique used is included in Annex IV. Upon generation of the defective pixel, 3 .txt files are generated containing the coordinates and values associated with each type of defective pixel, along with the original values that have been replaced.

3.7.1 Defective Imagery Analysis for T2D modelling

In order to accurately identify and estimate defective pixels within calibration imagery, we can conduct a similar procedure to the one seen previously:

1. **Sample data from Bias Frames**
    - → Compute and store Average
    - → Compute and store Bias
    - → Compute and store STD
2. **Sample data from 300s Dark Frame**
    - → Subtract Average and Bias to center distribution
    - → Flag pixel values > limit*STD [limit = 3÷10]
    - → Save pixel coordinates
3. **Sample data from all Dark Frames**
    - → Subtract Average and Bias to center distribution
    - → Save pixel values from flagged pixels
    - → Evaluate T2D in flagged pixels

We can expand on this process by repeating steps 2 and 3 for "ideal" pixels, i.e. pixels that on 300s exposure times have a photoelectric response similar to those of the bias frame (and thus have close to zero dark current values).

Results for the CCD sensor:

Data shown on Figure 43 demonstrates an expected behaviour, with ADU offsets always contained within 3σ on all exposure times. These offsets are likely caused by the inherent noise sources of the electronics, and fall within the expected range. Data displayed on Figure 42, however, displays a stark different behaviour: the outlier pixels are scaling linearly with exposure time, with proportionally different dark currents.

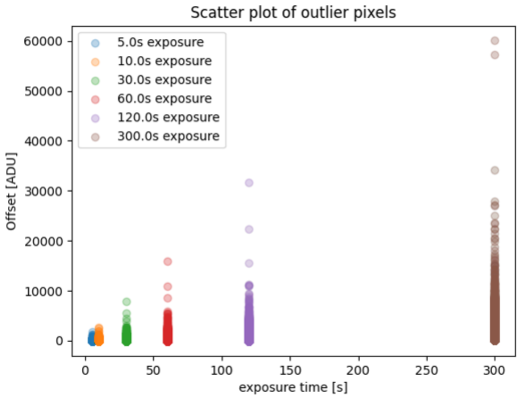

Figure 42: Outlier pixels ADUs

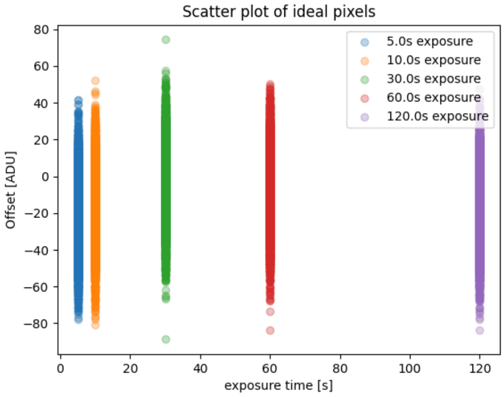

Figure 43: "Ideal" pixels ADUs

One can visualize how closely correlated are the results if we utilize the (37) T2D definition used earlier. If we plot the data of 60s and 300s Dark Frames against each other and represented as T2Ds, it is visibly noticeable the strong correlation for low T2Ds (strong proportional scaling), while results become loosely correlated for higher T2Ds as they are affected by noise.

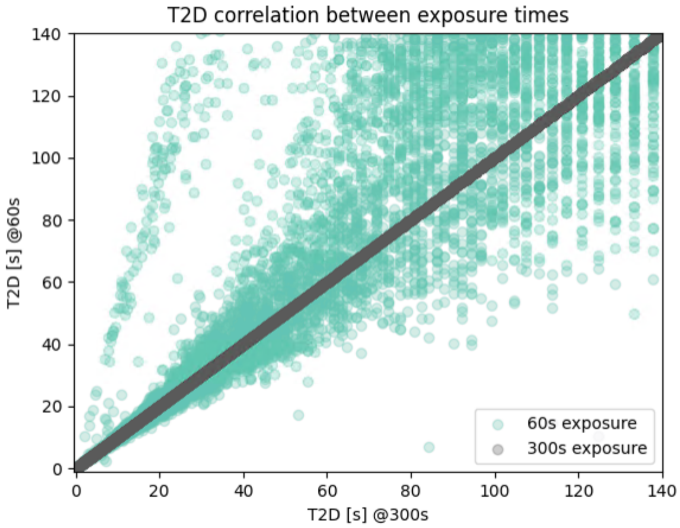

Figure 44: Comparison of T2Ds between 60s and 300s Dark Frames

Interestingly, there is a smaller "fan" of data that seems to scale proportionally differently to the rest. Although statistically small compared to the main distribution, this phenomena is likely due to an amplification gain defect in a part of the sensor.

By comparing between High-gain and Low-gain mode, we notice that the number of outliers does not vary significantly, unless if we set the threshold to 3-sigma. In that case, the thermal noise from the signal interferes with the outlier detection and generates inconsistent results.

frequency[MHz]	$\sigma_{biasframe}[pxl]$	$> 10\sigma[\#]$	$> 5\sigma[\#]$	$> 3\sigma[\#]$
12	12.98469	7667	13805	40586
2	12.98164	8237	13818	117412

Table 6: Outlier pixel behaviour at 300s Dark Frames

To properly model the T2Ds within the simulator, an appropriate distribution must be identified. Histogram data from outlier analysis can come in useful to test the fit of existing PDFs for random variable generation. Accordingly, we can plot the ADU offsets in such an histogram:

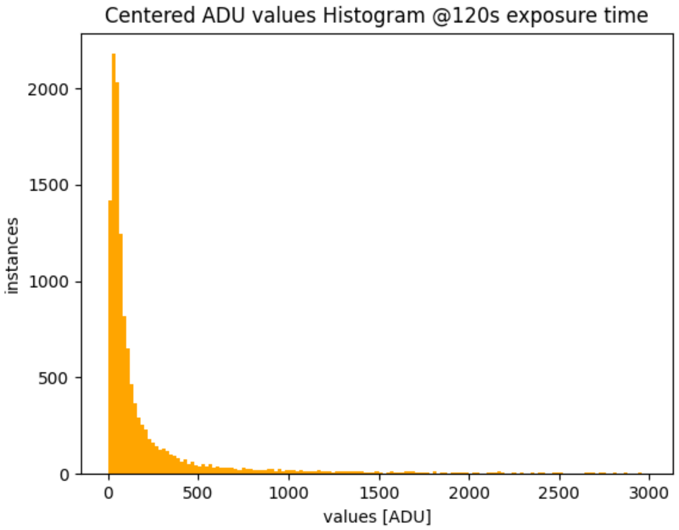

Figure 45: Histogram of ADU offsets for 120s Dark Frame

However the data for modelling requires that we remove the exposure time dependency of the ADU values, so conversion to T2D values is necessary. We can calculate the T2D values from equation (37):

$$T2D(x,y) = \frac{t_{exp} \cdot ADU_{bias}}{ADU_{centered}(x,y)} \tag{38}$$

And now can we plot their histograms according to exposure time and appreciate the variations in the distributions:

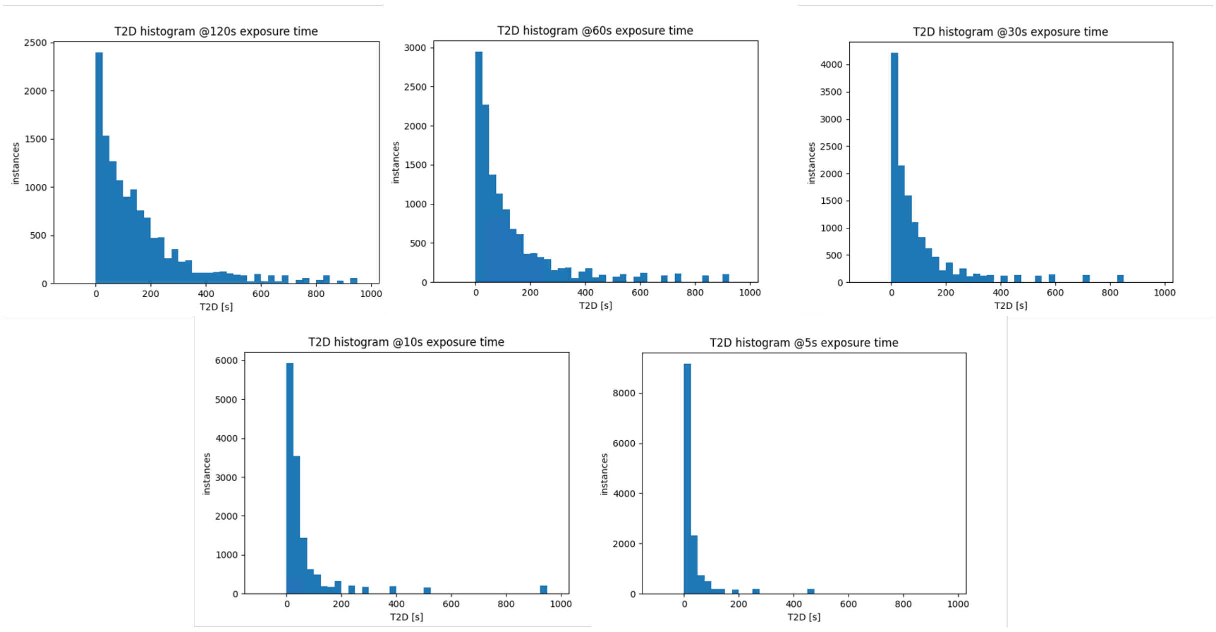

Figure 46: Histograms of T2Ds across exposure time

It is immediately noticeable how the distribution is skewed and restricted to a smaller domain as exposure time decreases, with a higher occurrence of T2Ds close to 0 as exposure time decreases.

After performing a variety of fitting tests with Exponential, Rayleigh, Weibull and Gumbel distributions, the Exponential PDF is chosen for modelling the phenomena, since defective pixel T2Ds are independent of each other, and this distribution is of the memory-less type.

$$f(x,\lambda) = \begin{cases} \lambda e^{-\lambda x}, & \text{if } x \geq 0, \\ 0, & \text{if } x < 0. \end{cases} \tag{39}$$

Where λ is the sole parameter of the distribution, also known as *rate parameter*. The distribution is bounded to the interval $[0,\infty)$. In Python, we utilize the *numpy.random.exponential()* method to generate a list of random variables for the T2D values.

Results for the CMOS sensor:

By performing the same analysis on the recently installed IMX 411 CMOS sensor, we can compare the performance relative to the 5-year old CCD sensor. At identical cooling and exposure conditions, we can compare data on cumulative outlier pixels:

Outliers [num]:	5s	10s	30s	60s	120s	300s
$ML11002@-25^{\circ}C$:	865	2253	7599	7602	7792	13805
$IMX411@-25^{\circ}C$:	4711	5223	7019	10472	17017	40567

Table 7: Outlier count for varying exposure times

Results show that at 300 seconds of exposure, roughly 0.1289 % of the CCD pixels (1 in 776) are flagged as defective, compared to the 0.0268 % (1 in 3731) of the 1-year old CMOS sensor. Data from [17] suggests that defective pixel density would scare proportionally with lifetime, but more data across multiple sensor's lifetimes would be required to definitely come to such a conclusion.

The same linearity of ADU offsets can be noticed on the CMOS sensor, with ideal pixels experiencing offsets within a reasonable range.

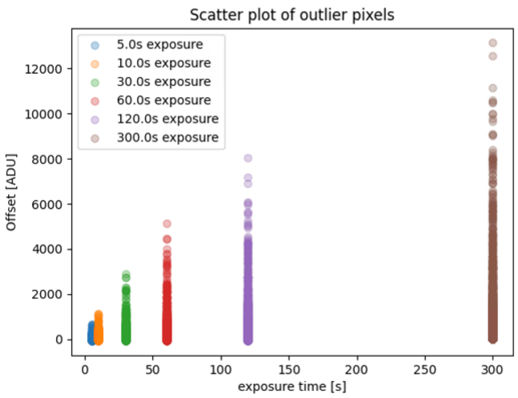

Figure 47: Outlier pixels ADUs

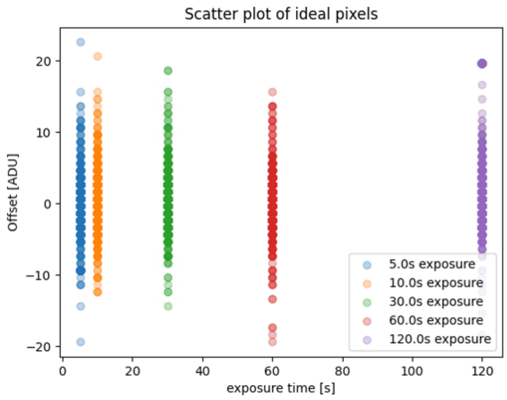

Figure 48: "Ideal" pixels ADUs

T2D correlation across exposure times is much more accurate, thanks largely to the heavily reduced dark-current rate and readout noise. Data at 120 seconds of exposure time scales almost identically to those at 300 seconds, proving that the dark current rate of those defective pixels remains practically constant during dark frames exposures.

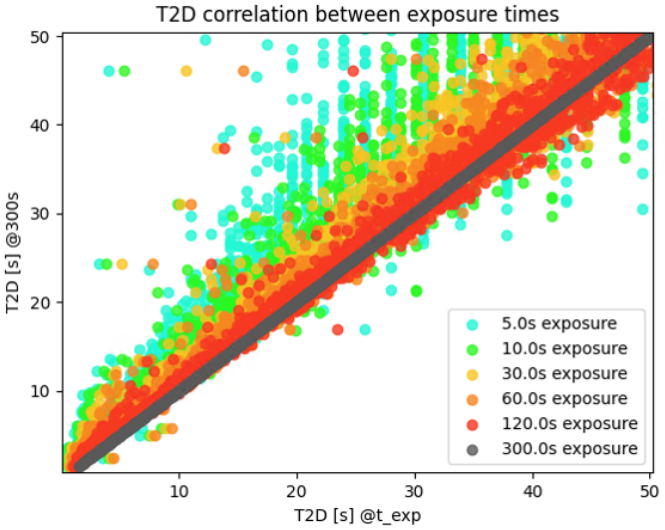

Figure 49: Comparison of T2Ds across exposure times on CMOS Dark Frames

Finally, we plot the histogram of the T2D data acquired from equation 37. In this case, the distribution peak is no longer at the origin, indicating that the average dark current rate of the defective pixels is lower to those of the CCD.

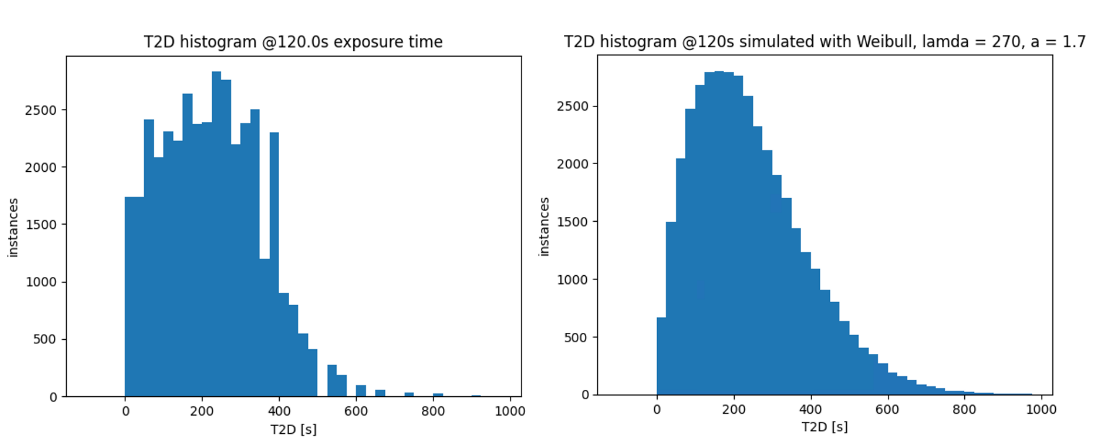

Figure 50: Weibull fit on sampled dark frame data at 120s exposure time

In this case, it was found to be more appropriate to model the phenomena using a Weibull distribution, since defect rates and proportionality are documented to have a loose connection with sensor life [17]. Weibull distributions are normally used to model reliability and life data analyses, so its use in this context can be justified as appropriate. We represent the Weibull PDF as:

$$f(x, \lambda, k) = \begin{cases} \frac{k}{\lambda}\left(\frac{x}{\lambda}\right)^{k-1} e^{-(x/\lambda)^k}, & \text{if } x \geq 0, \\ 0, & \text{if } x < 0. \end{cases} \tag{40}$$

Where λ represents the "scale parameter", and k constitutes the "shape parameter". This distribution can be made identical to that of exponential if the shape parameter is set at 1. For modelling and providing a more comprehensible input, we can utilize the Median Value, defined as $Median = \lambda(\ln 2)^{1/k}$. Figure 50 displays the fitted distribution on our data, which was estimated using the Python package *scipy.stats.weibull_min.fit()* and generated through the method *numpy.random.weibull()*.

3.8 SIP distortion

Distortion constitutes an intrinsic characteristic of the camera array and lenses that should be taken into account. These phenomena can be corrected within the data processing tools if this distortion information is modelled as a function of pixel position. The **Simple Imaging Polynomial** convention used in the *Spitzer Space Telescope* allows to calculate this distortion data via 2d polynomials and can be stored as a set of parameters within the FITS header.[19] The SIP coefficients are supported within the WCS methods, and even in scenarios where the polynomial coefficients can vary from one image to the other, such as with a moving scan mirror position, the distortion can be rapidly estimated.

Implementing this method calls for a set of relative pixel coordinates (*u,v*) with origin at CRPIX1, CRPIX2, provided within the header, and physically located on the focal plane. We define the set of angular coordinates (*x,y*) having origin at CRVAL1, CRVAL2, expressed as RA/DEC values. Then these "intermediate world coordinates", expressed in degrees, are uniquely determined on the plane-of-projection as:

$$\begin{pmatrix} x \\ y \end{pmatrix} = \begin{pmatrix} CD_{1,1} & CD_{1,2} \\ CD_{2,1} & CD_{2,2} \end{pmatrix} \begin{pmatrix} u + f(u,v) \\ v + g(u,v) \end{pmatrix} \tag{41}$$

The CD-matrix values store information on skew, rotation and scaling, whereas f(u,v) and g(u,v) represent the distortion polynomials defined as:

$$f(u,v) = \sum_{p,q} A_{p,q} u^p v^q, \qquad p + q \le A_{ORDER}[2-9] \tag{42}$$

$$g(u,v) = \sum_{p,q} B_{p,q} u^p v^q, \qquad p + q \le B_{ORDER}[2-9] \tag{43}$$

With A and B matrices storing the distortion coefficients. If any of the latter are not expressely indicated, they can be set as 0. Results from work carried out on the Spitzer Infrared Array Camera have demonstrated that cubic coefficients are sufficient to correct for distortions of up to 2-3 pixels. Furthermore, Spitzer provides reverse coefficients to perform fast inversion to find the original pixel coordinates:

$$\begin{pmatrix} U \\ V \end{pmatrix} = CD^{-1} \begin{pmatrix} x \\ y \end{pmatrix} \tag{44}$$

U and V are the "corrected pixel coordinates", and original coordinates can be found by summing them to the reverse polynomials:

$$u = U + F(U, V) = U + \sum_{p,q} AP_{p,q} U^p V^q, \qquad p + q \leq AP_{ORDER}[2 - 9] \tag{45}$$

$$v = V + G(U, V) = V + \sum_{p,q} BP_{p,q} U^p V^q, \qquad p + q \leq BP_{ORDER}[2 - 9] \tag{46}$$

For the necessities of the image simulator, we shall perform these reverse transformations to simulate image distortion. However, these reverse polynomials are not necessarily always included within the FITS data, and they must be approximated through iterative inversion techniques. The pseudocode for such an approximation goes as follows:

Algorithm 1 Pseudocode

```
procedure REVERSE SIP
    (u,v) ← RA/DEC coordinates
    N,M = APorder, BPorder
Create a grid of points
Compute corrected coordinates $U, V$ for each point
loop:
    for $N \times M$ matrix do
        Populate matrices A,B with forward coefficients.
        close;
    for UxV matrix do
        udiff = u-U.
        vdiff = v-V.
        close;
udiff,vdiff.flatten()
A = A,B
b = udiff, vdiff
Perform least-squares solution of $Ax$ = udiff
Perform least-squares solution of $By$ = vdiff
APcoeff = x
BPcoeff = y
Extract AP and BP coefficients into $N \times N$, $M \times M$ matrices
```

Using the forward coefficients provided in the Spitzer image headers, we can validate our algorithms by comparing the results obtained:

Coefficient	Tabulated Value	Approximated Value
AP_{01}	3.6698E-06	2.6805E-06
AP_{02}	-9.1825E-06	-9.2695E-06
AP_{03}	-3.8909E-09	-3.8356E-09
AP_{10}	-2.0239E-05	-1.9749E-05
AP_{11}	-4.8946E-05	-4.8915E-05
AP_{12}	1.7951E-07	1.7946E-07
AP_{20}	-2.8622E-05	-2.8697E-05
AP_{21}	-2.9553E-08	-2.9419E-08
AP_{30}	1.9119E-07	1.9116E-07

Table 8: Reverse coefficients of AP matrix

Clearly, this method is only an approximation of the distortion, and leads to a 5% maximum error (or about 0.1 pixels) when computing pixel distortion for the Spitzer camera array.

If we decide to plot the RMS distortion of x and y in a heat map, we notice that for this case the maximum distortion is taking place at the edges of the pixel array, where the maximum offset is roughly 2.5 pixels.

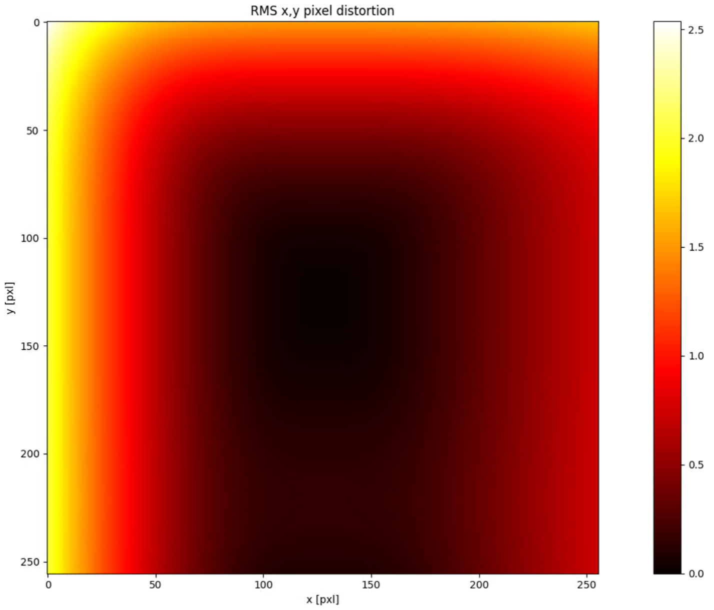

Figure 51: RMS distortion from approximated reverse coefficients on the Spitzer Infrared Array Camera

The implementation of these functionalities are included in the Astropy.WCS methods *all_world2pix* and *all_pix2world* which permit the simultaneous use of SIP and core WCS corrections.

4 Validation & results

4.1 Scenario selection

A set of 15 scenarios have been outlined to validate the models introduced in the image simulator. These scenarios are characterized by an increasing complexity, starting from the simplest calibration images and ending into the most complex tracking scenario. This way it's possible to gradually introduce the different effects being simulated and comment how they affect the output.

Images are produced both unbinned and with a 4x4 binning, saved into the .FITS format and evaluated using external scripts.

A comprehensive breakdown of the scenarios is provided in the following table:

ID	Scenario	Effects simulated
1	Bias Frame @0.01s	**RO, FPN noise**
2	Dark Frame @5s	RO, FPN noise, **DC rate, Defective pixels**
3	Dark Frame @300s	RO, FPN noise, DC rate, Defective pixels
4	Empty Sky	RO, FPN noise, DC rate, Defective pixels, **background photons**
5	Stars - Low Mag	RO, FPN noise, DC rate, Defective pixels, **FWHM, Stars (Filtered)**, background photons
6	Stars - All	RO, FPN noise, DC rate, Defective pixels, FWHM, **Stars (ALL)**, background photons
7	Object - SNR:20	RO, FPN noise, DC rate, Defective pixels, FWHM, **Object(Arbitrary)**, background photons
8	Object - Simulated	RO, FPN noise, DC rate, Defective pixels, FWHM, **Object(Simulated)**, background photons
9	Sideral - Low SNR	RO, FPN noise, DC rate, Defective pixels, FWHM, Object, Stars, background photons
10	Sideral - High SNR	RO, FPN noise, DC rate, Defective pixels, FWHM, Object, Stars, background photons
11	Sideral + Cosmics	RO, FPN noise, DC rate, Defective pixels, FWHM, Object, Stars, background photons, **cosmics**
12	Sideral + Straylight	RO, FPN noise, DC rate, Defective pixels, FWHM, Object, Stars, background photons, **straylight photons**
13	Tracking	RO, FPN noise, DC rate, Defective pixels, FWHM, Object, Stars, background photons, **Tracking**
14	Tracking + Straylight	RO, FPN noise, DC rate, Defective pixels, FWHM, Object, Stars, Background and Straylight photons, Tracking, **Vignetting**
15	Tracking - FULL	RO, FPN noise, DC rate, Defective pixels, FWHM, Object, Stars, Background and Straylight photons, Cosmics, Tracking, Vignetting, **Pointing Error**

Table 9: Scenario selection effects breakdown

4.1.1 Scenarios 1-3: Calibration Frames

SCENARIO 1 - BIAS FRAME

The simplest scenario we shall generate is the Bias Frame taken at 0.01 seconds of exposure time. We produce both binned and 4x4 binned results, where the only effects introduced are bias, RO and FPN noise. In this and all subsequent scenarios we shall collect statistical information on mostly unbinned images, but for this section binned images will also be evaluated.

Bin type	σ	Median	μ
Unbinned Image	3.91	1002	1002.54
4x4 Binned Image	1.02	1002	1002.07

Table 10: Bias frame results

Table 10 displays the effect of binning on images, that is mostly noticeable in a drastic reduction of STD by an order comparable of that of the bin size. Average values are also reduced significantly. We can produce a surface plot on obtained results to visualize the typical noise pattern that will characterize most of the results.

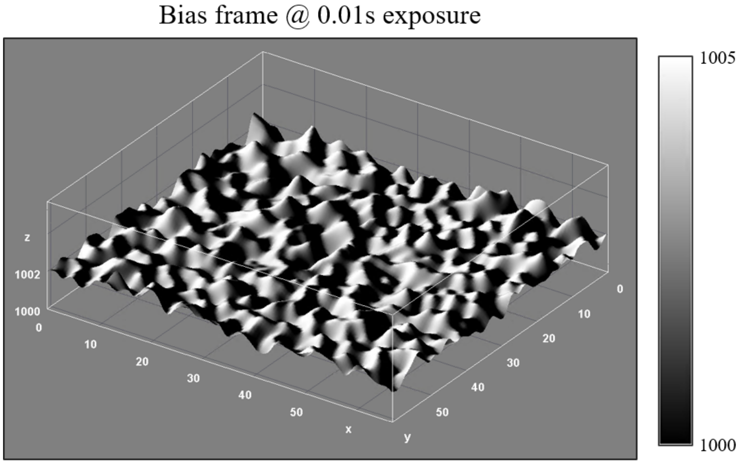

Figure 52: Surface plot of readout noise background

SCENARIO 2 & 3 - DARK FRAMES

For scenarios 2 and 3, we simulate dark frames across a variety of exposure times for binned and unbinned imagery. We introduce defective pixels and dark current rate phenomena to generate these results, with 10.000 hot pixels ranging from a minimum of T2D: 2 and a median of T2D: 217. Dark current rate is set to a conservative 0.0006 ADU/pxl, for ideal $-35\,\text{deg}$ C cooling conditions.

Bin Type	σ	Median	μ
Unbinned 5s	3.92	1002	1002.54
4x4 Binned 5s	1.02	1002	1002.07
Unbinned 300s	5.28	1002	1002.73
4x4 Binned 300s	1.35	1002	1002.26

Table 11: Simulated dark frames results

Table 11 displays the results obtained on 5 and 300 second scenarios. The 300 second scenario allows us to appreciate the same long-tail distribution phenomena seen in real calibration imagery. These defective pixels are particularly noticeable when 3d plotting these values, and can be easily identified on unbinned imagery.

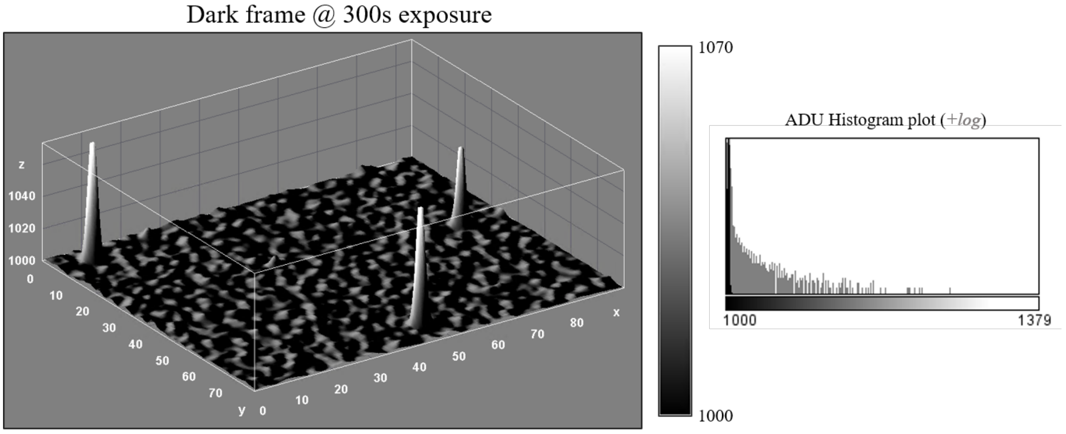

Figure 53: Surface plot of a simulated 300s dark frame

However, a typical sideral scenario rarely surpasses the 5 seconds of integration time, and never exceeds 30 seconds. For these types of scenarios, the defective pixels are barely noticeable, especially in binned imagery where their effect is greatly mitigated. Table 12 displays STD and outlier analysis results (with the same approach from section 3.7.1) obtained on binned imagery.

Dark Frame	σ(unbinned)	Detected outliers
4x4 Binned 5s	1.02(3.92)	56
4x4 Binned 10s	1.02(3.93)	100
4x4 Binned 30s	1.03(3.95)	402
4x4 Binned 60	1.05(4.02)	857
4x4 Binned 120s	1.09(4.21)	1705
4x4 Binned 300s	1.35(5.28)	3997

Table 12: Outlier counts for binned imagery

Even at 300 seconds, with a 5-sigma tolerance, not even half of the defective pixels can be resolved, thanks to the improved performance of the CMOS sensor and the mitigating effects of binning. We also produce the same scatter plots on outliers, along with a linear regression on inlier values to confirm the validity of the results:

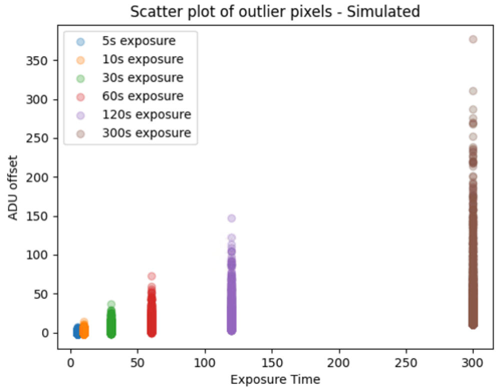

Figure 54: Outlier pixel ADUs

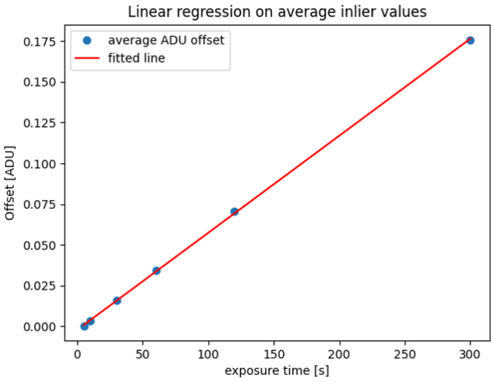

Figure 55: DC rate linear fit

4.1.2 Scenario 4: Empty Sky

With Scenario 4 we are able to introduce the first of the Poisson-distributed noise sources, that is the photons incoming from the background noise. Applying the model developed in section 3.6.3, we can calculate the photons entering our sensor based on a 22 magnitude background sky. Simulations show that about 3 billion photons would be hitting the sensor wells across 5 seconds, with an approximate number of 19-20 photons per pixel well. These photons are modelled through a Poisson distribution, which increases the overall STD of our distribution, and biases the mean and median values:

Scenario	σ	Median	μ
2 - Dark Frame @5s	3.92	1002	1002.54
4 - Empty Sky @5s	7.46	1014	1013.69

Table 13: Empty sky scenario results

Comparing the results with the 5 seconds Dark Frame, clearly the effect of background noise is more degenerative than defective pixels in terms of signal resolution for low exposures, and this effect will be permanently modelled in Sideral and Tracking scenarios. The following graph displays the distribution change generated, typical of a Poissonian-like PDF.

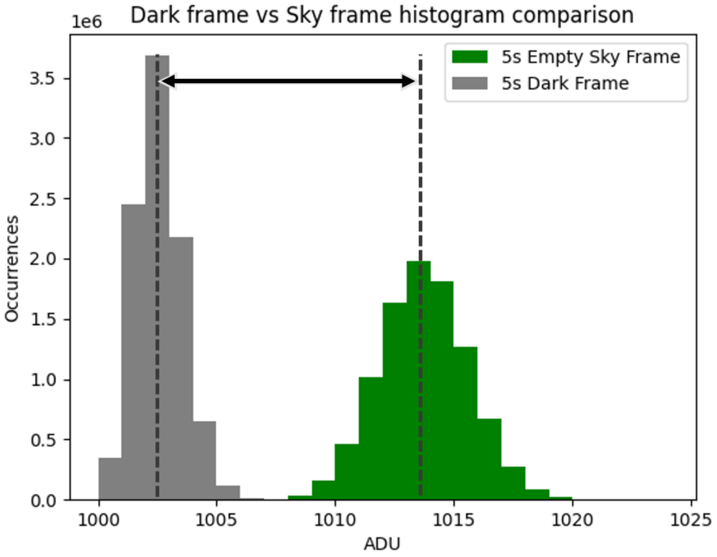

Figure 56: Histogram comparison of simulated sky frame

4.1.3 Scenarios 5-6: Stars

In Scenarios 5 and 6, we introduce the GAIA star catalogue, and stars are represented as point-like features as in a Sideral scenario (without the target object). We utilize a catalogue of approximately 30k stars ranging from 18 to 5 magnitude for Scenario 6, but we limit the range of stars between 18 and 17 to identify the fainter stars that constitute the majority of the database in Scenario 5.

Scenario	σ	Median	μ
4 - Empty Sky @5s	7.46	1014	1013.69
5 - Stars (Low Mag) @5s	7.68	1014	1013.73
6 - Stars (All) @5s	285.56	1014	1016.71

Table 14: Results from star representation scenarios

Results from table 14 demonstrate how higher magnitude stars have an exponentially greater impact on standard deviation and mean values, and magnitudes closer to 5 can almost saturate the pixel well, when the photoelectric response to excitation becomes non-linear and difficult to model. Table 15 provides some further insight on the optical performance model when representing these two Scenarios:

Scenario	Mag. Range	Visible Stars	Median SNR
5 - Stars (Low Mag) @5s	18-17	5352	4.10
6 - Stars (All) @5s	18-5	14545	10.39

Table 15: Star representation data

The distributions are also quite different, with fainter stars only providing a signal sufficient for a maximum of 150 ADUs, whereas the other scenario has a full range of values ranging from 1000 ADUs (bias offset) to saturation values at 65535 ADUs.

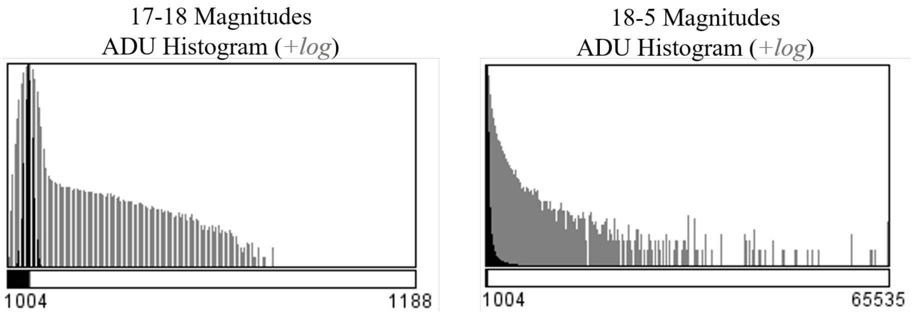

Figure 57: Histogram comparison between magnitude ranges

The following image shows results obtained at FWHM of 2.75 pixels, with a Fire LUT color map and on a full range of stars.

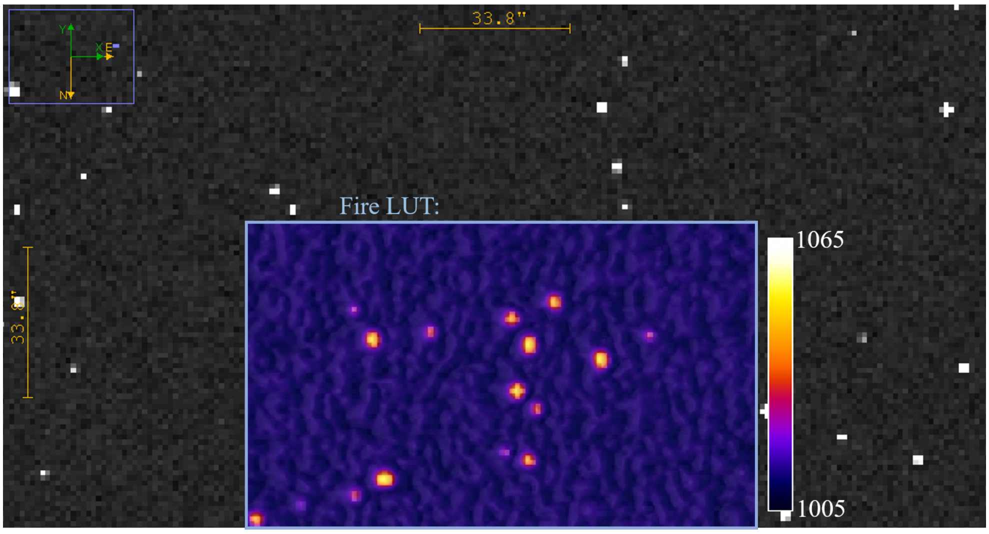

Figure 58: Overlay of Fire LUT map on simulated star sensing imagery

4.1.4 Scenarios 7-8: Target object

For Scenarios 7-8 we shall represent a lone Object in absence of stars. We utilize the approach seen in section 3.6.1 to calculate Peak and Total signal emitted by an object with the following properties:

- Distance to observer: 42.000.000 m (GEO)
- Object LOS w/ sun: 40deg

- Ω (Relative Velocity): .15 deg/s
- Temperature: 290 K
- Radius: .7 m
- Observer-Object LOS: 0 deg
- Surface: Purely Diffusive

We obtain an SNR of 1.49, with a 44 photon signal peak. This type of signal would be barely noticeable and hard to detect, since it could be easily mistaken with signal noise or defective pixels. To simulate across a variety of SNR, we calculate signal strenght based on SNR and provide it as an input within our models.

SNR	Peak Signal (ph)	Total Signal (ph)
1	29	87
1.5	44	131
3	95	286
5	174	526
10	441	1333
20	1322	3989

Table 16: Theoretical Signal strenght from SNR for FWHM = 2.75 pixels

Applying the theoretical photon counts into our model produces images with SNR ratios very close to theoretical values, and objects with SNRs larger than 5 show as clearly detectable

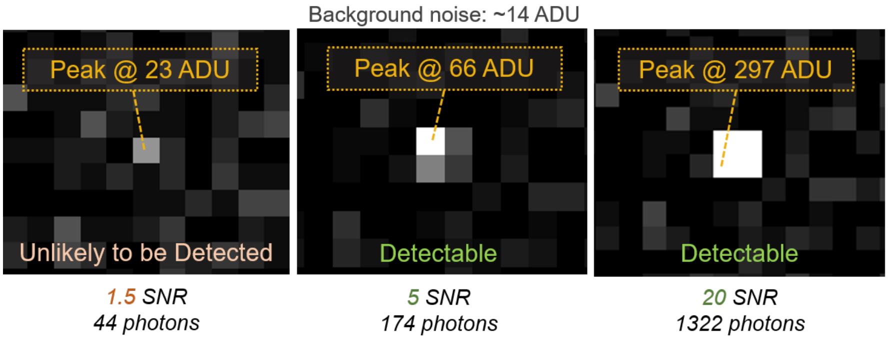

1.5 SNR
44 photons

5 SNR
174 photons

20 SNR
1322 photons

Figure 59: Detectability of simulated sources based on SNR

4.1.5 Scenarios 9-12: Sideral

Scenarios 9 to 12 constitute Star Sensing scenarios, also known as fixed Sideral pointing scenarios, in which we introduce a debris object with a relative velocity with respect to the focal plane. In this way, the energy deposited within the sensor wells is spread across a larger number of pixels, and since total energy should be conserved, one should expect to see decreasing SNRs as streak size increases.

Scenario 9 simulates that specific topic, by utilizing the same signal seen in the static object case to generate a streak with dRa = 0.002 deg/s and dDEC = -0.005 deg/s.

Scenario 10 performs the same simulation, with an increase of photon count to 15000 photons.

Scenario	Signal Power	Object SNR	Peak ADU
8 - Static Object - Simulated @5s	1322	21.73	297
9 - Sideral - Low SNR @5s	1322	1.49	29
10 - Sideral - High SNR @5s	15000	21.64	303

Table 17: Results for sideral scenarios

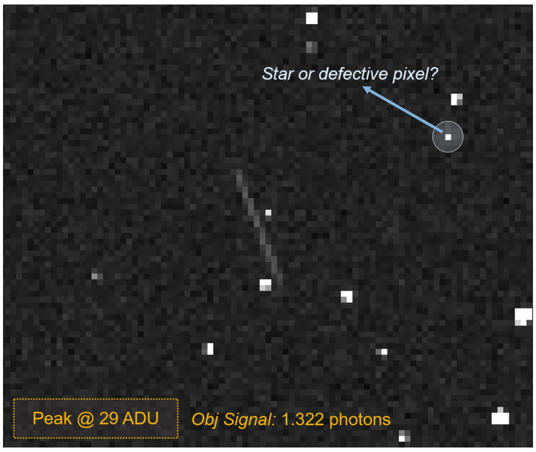

Figure 60: Faint Streak

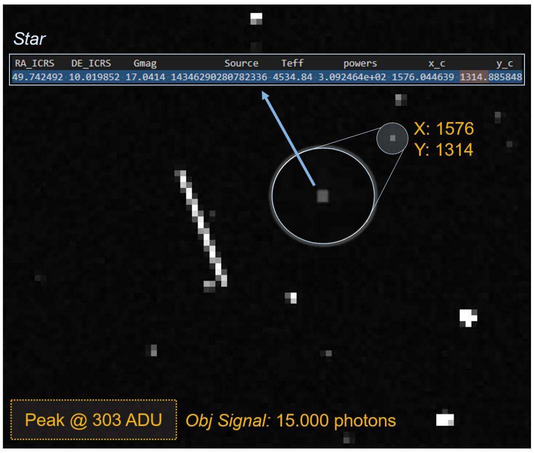

RA_ICRS	DE_ICRS	Gmag	Source	Teff	powers	x_c	y_c
49.742492	10.019852	17.0414	1434629028078233б	4534.84	3.092464e+02	1576.044639	1314.885848

Figure 61: Bright Streak

Scenario 11 introduces Medium-intensity Cosmics, introduced as a voltage offset that is introduced as ADU offsets. The scenario being simulated is taking place at a 800 km Sun-syncronous orbit, right on the edge of the SAA at **Latitude: 2.36 deg** and **Longitude: -27.69 deg**. We are simulating a total of 63570 proton-encounter events for an unshielded telescope.

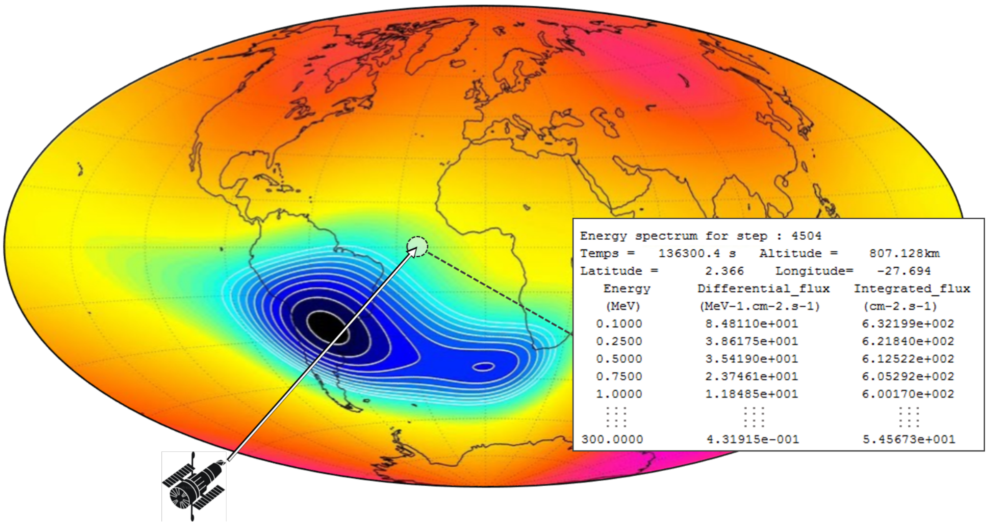

```
Energy spectrum for step : 4504
Temps =   136300.4 s   Altitude =    807.128km
Latitude =       2.366    Longitude=   -27.694
   Energy         Differential_flux   Integrated_flux
    (MeV)         (MeV-1.cm-2.s-1)     (cm-2.s-1)
   0.1000           8.48110e+001        6.32199e+002
   0.2500           3.86175e+001        6.21840e+002
   0.5000           3.54190e+001        6.12522e+002
   0.7500           2.37461e+001        6.05292e+002
   1.0000           1.18485e+001        6.00170e+002
    :::                 :::                 :::
    :::                 :::                 :::
 300.0000           4.31915e-001        5.45673e+001
```

Figure 62: Simulated location on the SAA

Scenario	σ	Median	μ
10 - Sideral - High SNR @5s	285.56	1014	1016.71
11 - Sideral + Cosmics @5s	379.51	1014	1019.34

Table 18: Comparison of results with the addition of cosmics

While SNR values remain constant, STDs and image quality as a whole is massively depreciated, with a considerable density of single defective pixels, and a problematic number of linear series of pixels being affected by cosmic ray effects. These series of pixels could easily be misidentified for debris streaks and pose a real problem for our IOD solutions.

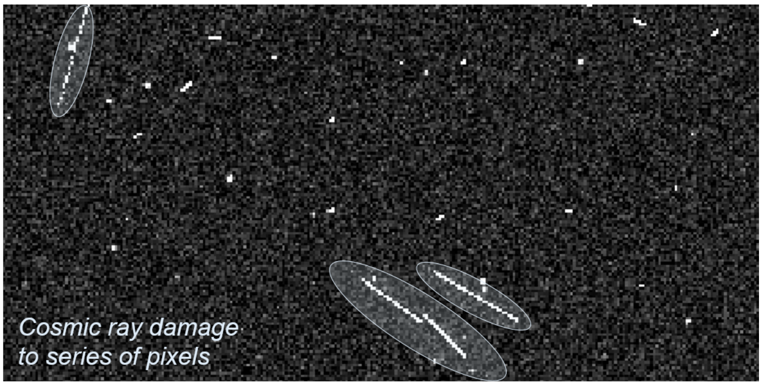

Figure 63: Simulated cosmic ray damage to series and groups of pixel wells

Finally, Scenario 12 represents an unlikely scenario where the telescope is accidentally pointing with a 70 deg LOS w.r.t. the Sun. Accounting for baffle attenuation, this effect produces roughly 200 additional incident photons per pixel. In reality, such a scenario could massively degrade the sensor and potentially render it unusable if exposed for long exposure times. Reflected straylight is also a considerable concern for other celestial bodies, especially the moon, and contributes significantly to the deposited photon count.

Scenario	Signal Power	σ	Median	μ
10 - Sideral - High SNR @5s	15000	285.56	1014	1016.71
12 - Sideral + Straylight @5s	15000	379.17	1159	1165.02

Table 19: Comparison of results with the addition of straylight

As shown in the Figure 64, the introduction of an additional Poissonian noise source introduces a bias and increase of STD similar to Scenario 4, albeit with much more dramatic results.

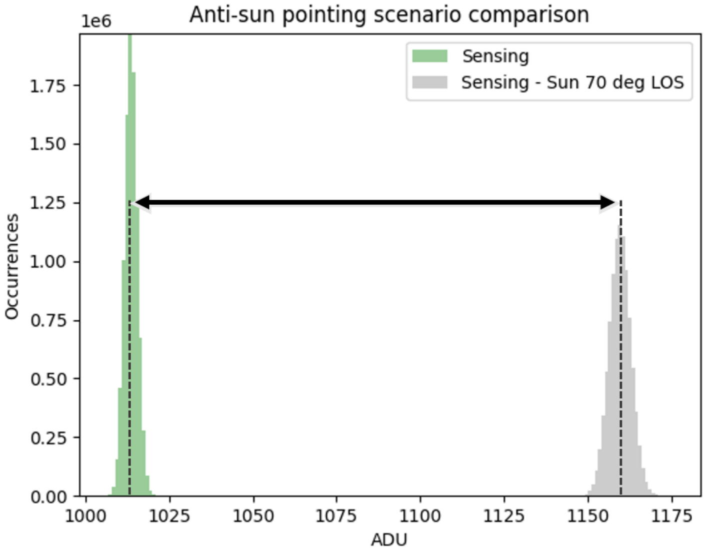

Figure 64: Distribution offset due to straylight

Star-identification capabilities are also greatly reduced, with the majority of the population now becoming undetectable, this kind of scenario could possibly compromise performance of orbital attitude determination using star tracking techniques. Object detection is also greatly compromised, with a 15.000 photon-strong signal becoming undetectable amidst the noisy background.

Scenario	Signal Power	Object SNR	Median Star SNR	# Visible Stars
10 @5s	15000	21.64	10.39	14645
12 @5s	15000	<1	0.89	6807

Table 20: Comparison of results between sideral and tracking scenarios

4.1.6 Scenarios 13-14: Tracking

Scenario 13 simulates a tracking scenario, and the focal velocity of the object across the telescope's focal plane is close to none. In this scenario, all the energy of the object is focused in its centroid, and pixel dwell time of that centroid is identical to the exposure time of our image. This process results in two noticeable differences:

- Object SNR is greatly improved, since the same pixels are exposed continuously to the same point-like source
- Star SNR is greatly reduced, since they are now represented as streaks with energy being dispersed across a wider array of pixels

We can visualize these effects by displaying the surface plot of the results obtained:

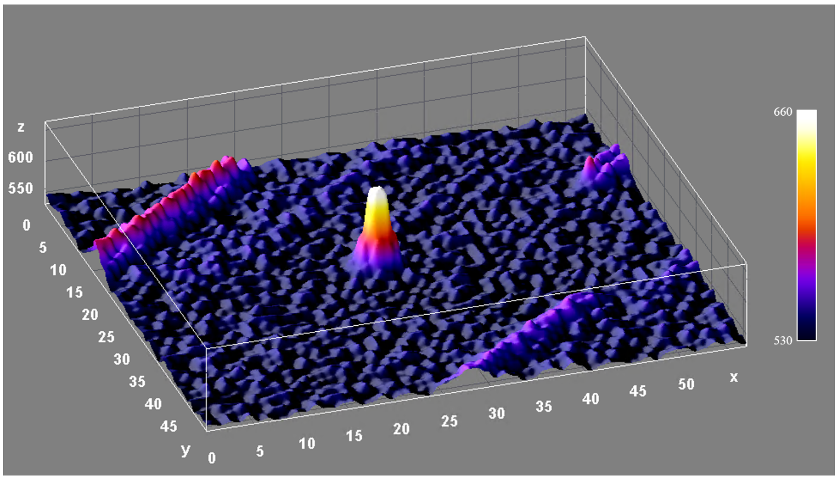

Figure 65: Surface plot of signal from tracked object

As expected, the object signal power is represented almost identically to the static object simulation, with slight differences caused by poisson-like scintillation effects simulating atmospheric turbulence in the upper regions.

Scenario	Signal Power	Object SNR	Peak ADU
8 - Static Object - Simulated @5s	1322	21.64	297
9 - Sideral - Low SNR @5s	1322	1.49	29
13 - Tracking @5s	1322	22.86	303

Table 21: Results for object SNR determination

The following figures display a heatmap plot of the results obtained, along with the log-normed histogram distribution.

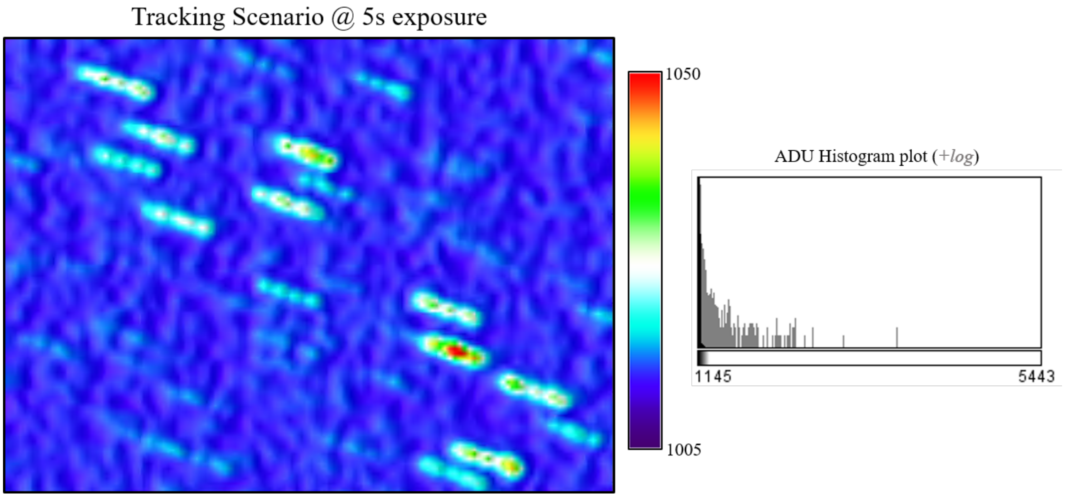

Figure 66: Tracking scenario imagery and distribution

Finally, Scenario 14 introduces vignetting, which is applied at the end of the simulation pipeline, more precisely at the ADU data manipulation phase before performing thresholding. The method described in Annex V allows us to model both behaviour of vignetting displayed in our sensors:

- CCD imagery displays vertical vignetting, with a central foci and a 10% field coverage. ADU offsets are also of a greater magnitude.
- CMOS imagery displays corner vignetting, with a shifted foci and a 30% coverage.

Our implementation allows us to simulate both of these effects, with are applied as a matrix subtraction during ADU conversion.

The results from this simulation can be easily validated by displaying surface plots across the entire image, with significant mesh smoothing. For CCD-like vignetting, the effect at the edges now becomes apparent along with their magnitude and relative coverage.

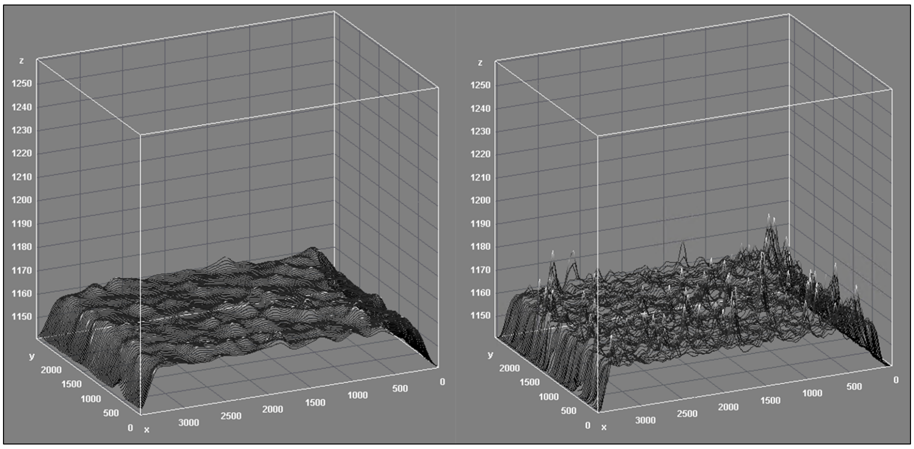

Figure 67: Scenario vignetting under different mesh smoothing

4.1.7 Scenario 15: Full Tracking

Scenario 15 models an extreme scenario where we are simulating all of the implemented functionalities at once. This type of simulation can be treated as an extreme worst-case scenario, used to simulate the upper bounds of detectable signals.

As seen in the previous sun-pointing scenario, object detection is impossible with such high values of standard deviation for the background. The same phenomena manifests within the Star catalogue representation, with a large majority of the catalogue being undetectable amongst the noise, and only 1517 stars having detectable SNR counts.

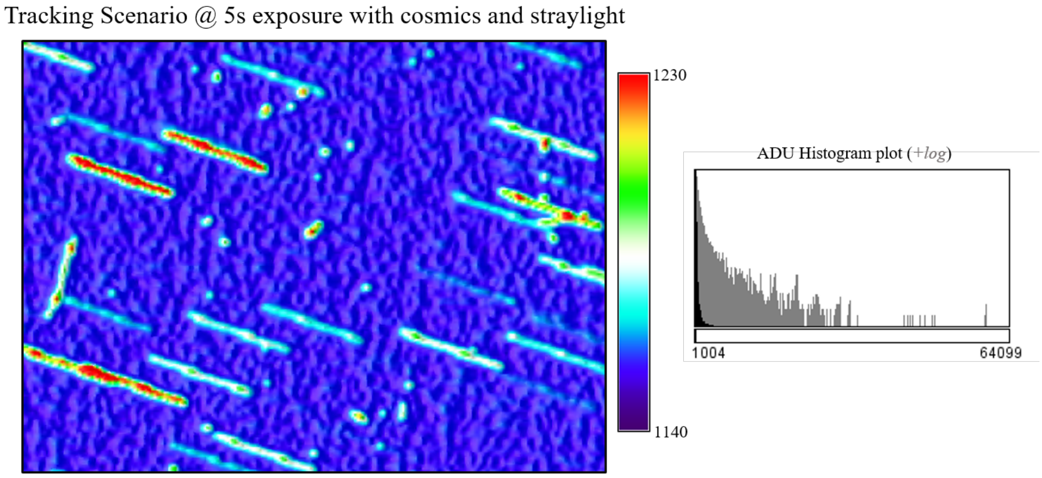

Figure 68: Full tracking scenario with imagery and distribution

Results remain somewhat similar to the previous scenario, apart from cosmic ray contributing to a large number of false-positives for streaks and defective pixels.

Scenario	Signal Power	Object SNR	σ	Median	μ
14 @5s	15000	<1	235.09	1159	1161.98
15 @5s	15000	<1	342.70	1159	1164.61

Table 22: Tracking scenarios results

These 15 scenarios have proven useful to demonstrate the individual effects implemented, along with their stack-ability and reconfiguration. A table with all relevant results is provided in Annex VII.

4.2 Real vs Synthetic imagery CMOS

The final step in the validation process consists in replicating real imagery from the ART by simulating both the signal received and all the layers of phenomena affecting the image. For the purposes of simulation, input data was either derived from the manufacturer's specification or direct observation through reverse-engineering.

The process to replicate Real-life imagery can be summarised as follows:

1. **Select a real tracking scenario**
    - → From NORAD, extrapolate object size and orbit data
    - → From HEADER, save Observation parameters
    - → From Seeing Profiles, compute FWHM
2. **Perform theoretical SNR and Signal calculation**
    - → Compute equivalent exposed surface area
    - → Return Peak and Total signal in photons
3. **Generate Star database from real pointing scenario**
    - → Provide magnitude range
4. **Simulate synthetic scenario**
5. **Compare results with real scenario**
    - → Iterate with step 4 to adjust for background magnitude

The tracking scenario in question involves a satellite belonging to the Fourth generation of the Navstar Global Positioning System constellation. These satellites are placed in semi-synchronous MEOs, and are observed daily for telescopic calibration and error compensation.

Due to the large amount of available imagery, detailed time and positioning data on these objects, they have proved to be an important asset for synthetic image simulation and validation.

Figure 69: Block IIF GPS render

Object Properties	
Name:	Navstar 71 (USA 256)
NORAD:	40105
Semi-Major Axis:	26559 km
Dimensions:	2.49 X 2.03 X 2.22 m

Table 23: Navstar 71 properties

FWHM values are extrapolated by visualizing the seeing profile of real streaks though AstroImageJ. While FWHM is not constant and varies between 5 and 3.5 pixels, faint streaks generally have values around 4.5 pixels, and constitute the majority of observed phenomena.

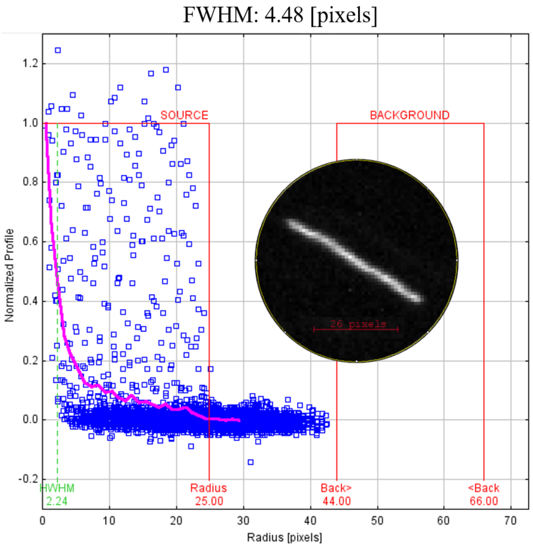

Figure 70: Seeing profile of a faint streak

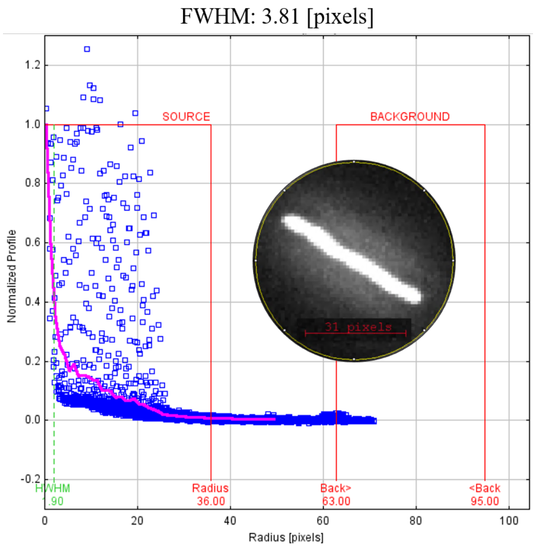

Figure 71: Seeing profile of a bright streak

The Optical Performance Model implemented within our simulator, allows to calculate hypothetical signal strength to be used as input for the PSF. We utilize an equivalent-area spherical model to represent the object, with a reflectance of 0.65 for anodized aluminum. FWHM values also come into play here, when estimating peak and total signal.

Radius	1.393 m
SNR	11.90
Peak Signal	2856 photons
Total Signal	13836 photons

Table 24: Synthetic object parameters

Finally, scenario parameters are extrapolated and used as input for the image simulator.

Scenario parameters - CMOS	
Exposure time:	2 s
Binning:	2x2 pixels
FOV:	3.07 x 2.19 deg
RA:	120.95115 deg
DEC:	-29.25022 deg
dRA:	0.008558 deg/s
dDEC:	-0.005486 deg/s
Pixel FOV:	0.79 arcsec

Table 25: Scenario parameters - CMOS

Finally, we also simulate the vignetting effect shown in the CMOS science images. This effect is much fainter than the CCD's and is only noticeable in the corners but, for the sake of completeness, is being applied accordingly.

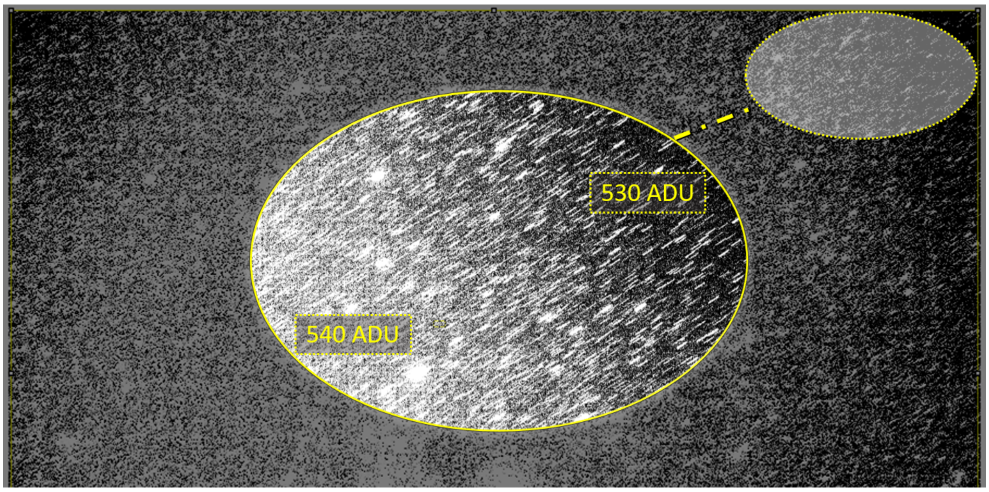

Figure 72: Corner vignetting on CMOS image

In the case of CMOS imagery, images are binned to optimize for storage, with an averaging binning technique being utilized (although additive can also be sometimes used).

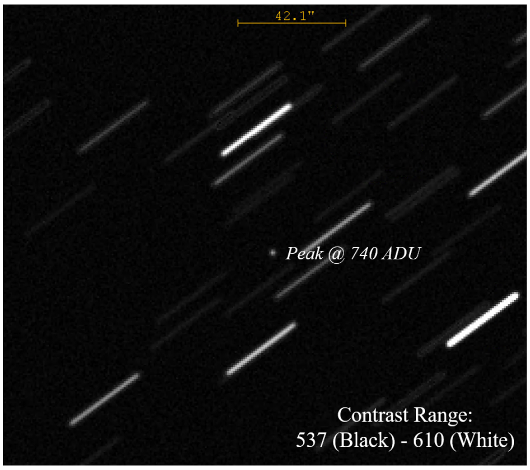

Figure 73: Synthetic image results on CMOS imagery

Comparing the results obtained, hypothetical ADU signal values are quite accurate, however standard deviation values are consistently higher.

Image	σ	Median	μ	ADU peak
Real @2s	91.66	538	541.28	768
Synthetic @2s	138.50	539	545.45	740

Table 26: Real vs Synthetic table of results - CMOS

Comparing the distributions of ADU values, the main peaks for background noise are almost identical, The deviations in STDs are attributed to wider long tails from the star representation. Since many dispersive atmospheric effects and cloud coverage are reducing the intensity of brighter objects, we consistently notice that brighter stars are being represented with higher ADUs than in real life. Overall, out of 29143 stars sampled, 20452 stars fall into frame and are being simulated.

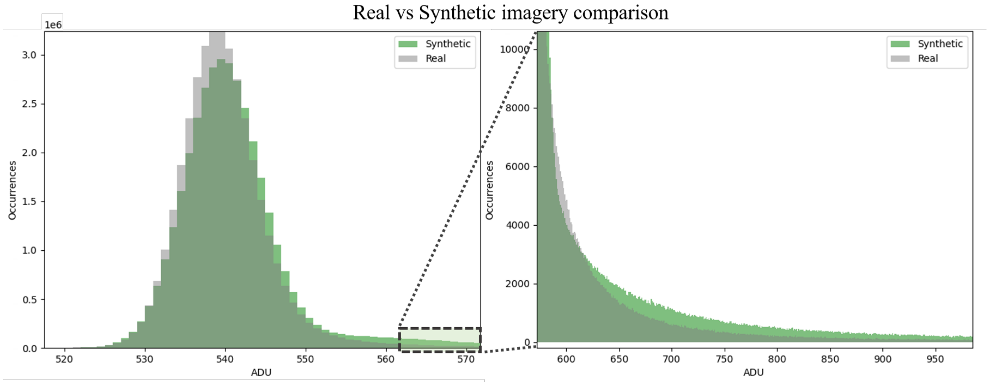

Figure 74: Real vs Synthetic histograms

All the input parameters used for the simulation are shown below. Note how the defective pixel values were reverse engineered from the characterization process illustrated in Section 3.7.1, and background magnitude has been determined through a couple of iterations.

Telescope Parameters	
Exposure time:	2 s
Binning:	2x2 pixels
dRA:	0.008558 deg/s
dDEC:	-0.005486 deg/s
Pixel FOV:	0.79 arcsec
Feature Representation	
Signal Power:	2856 photons
FWHM:	4.5 pixels
Back. Magnitude:	19.72
Star Mag. Range:	18 to 5
Noise Parameters	
Bias:	494 ADU
RO Noise:	4.8 e^-/pixel
DC Rate:	0.01 e^-/pixel/s

Defective Pixels	
Hot Pixels:	10000 #
Median T2D:	217 s
Minimum T2D:	0.5 s
Weibull Shape:	1.7
Vignette Parameters	
Correlation:	1
Max Value:	10
Coverage:	30%
Offset x:	400 pixels
Offset y:	0 pixels
Sensor Parameters	
Bit Depth:	16 bits%
Full Well:	45000 e^-
Pixel Size:	3.76 μm

Table 27: Simulation Parameters - CMOS

4.3 Real vs Synthetic imagery CCD

A similar scenario can be replicated for CCD imagery. Furthermore, for this pointing scenario there synthetic images produced before this collaboration's implementations to which we can compare the improvements in performance. Again, we utilize the calibration imagery from Navstar 67 (another Block IIF GPS platform) to derive the necessary data.

Object Properties	
Name:	Navstar 67 (USA 239)
NORAD:	38833
Semi-Major Axis:	26560 km
Dimensions:	2.49 X 2.03 X 2.22 m

Table 28: Navstar 67 properties

With corresponding spherical synthetic object having the following properties:

Radius	1.393 m
SNR	33.79
Peak Signal	3084 photons
Total Signal	6946 photons

Table 29: Synthetic object properties

In this case, images are unbinned and except from 16bit thresholding, no further post-processing is necessary. Note how Pixel FOV is much greater due to the reduced pixel array with respect to the corresponding FOV.

Scenario parameters - CCD	
Exposure time:	2 s
Binning:	None
FOV:	2.10 x 1.41 deg
RA:	276.81949 deg
DEC:	55.61763 deg
dRA:	0.01736 deg/s
dDEC:	0.004122 deg/s
Pixel FOV:	1.894 arcsec

Table 30: Scenario Parameters - CCD

We perform a visual inspection on results across the 3 images, and note down the SNRs obtained. Results show that the new imagery displays improved fidelity in both SNR representation and background noise. Under the same contrast ratio, old synthetic imagery appears much dimmer, with much lower average background values.

Plotting the distribution of ADUs helps to highlight the discrepancy between the three distribution, with new synthetic and real imagery almost perfectly overlapped, and old imagery experiencing a considerable bias and shape discrepancy.

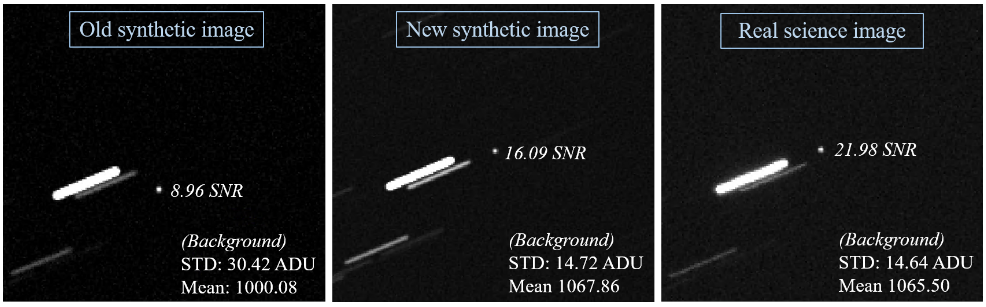

Figure 75: Comparison of real vs synthetic imagery - CCD

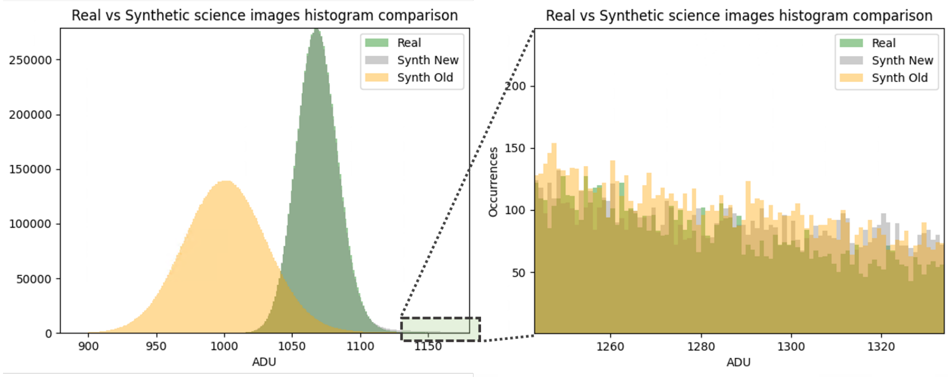

Figure 76: Comparison of Real vs Synthetic distributions - CCD

Image	$\sigma_{background}$	Median	μ
Real @2s	14.64	1067	1070.24
Old Synthetic @2s	30.42	1002	1005.57
New Synthetic @2s	14.72	1068	1076.54

Table 31: Real vs Synthetic (old and new) table of results - CCD

Due to the smaller FOV, only 20011 stars are sampled, with 9876 stars falling into frame.

The input parameters utilized for the new simulation are displayed below. As per the previous example, defective pixel values were reverse engineered from the sensor's characterization process.

Telescope Parameters	
Exposure time:	2 s
Binning:	None
dRA:	0.01736 deg/s
dDEC:	0.004122 deg/s
Pixel FOV:	1.894 arcsec
Feature Representation	
Signal Power:	3084 photons
FWHM:	2.0 pixels
Back. Magnitude:	20
Star Mag. Range:	18 to 5
Noise Parameters	
Bias:	921 ADU
RO Noise:	10.64 e^-/pixel
DC Rate:	0.0006 e^-/pixel/s

Defective Pixels	
Hot Pixels:	5000 #
Median T2D:	42 s
Minimum T2D:	2 s
Weibull Shape:	1.2
Vignette Parameters	
Correlation:	100
Max Value:	8
Coverage:	10%
Offset x:	0 pixels
Offset y:	0 pixels
Sensor Parameters	
Bit Depth:	16 bits
Full Well:	60000 e^-
Pixel Size:	9 μm

Table 32: Simulation parameters - CCD

5 Conclusion

Within this thesis, a variety of improvements have been introduced to the Image Simulator:

- An optical performance model has been introduced, with the capability of simulating synthetic features based on orbital, object and telescope parameters.
- A detailed noise model, along with the introduction of a novel characterization of pixel defects, has been developed and integrated both within the simulator and as a separate script.
- Custom functions have been introduced to simulate a variety of effects, most notably on cosmic rays, vignetting, lens distortion, and straylight phenomena.
- Streamlined validation and image recreation procedures have been detailed, providing a foundation for SBOC's software tests.
- Improvements to input and output formats, along with conversion between FWHM and EE, have been put in place.

Synthetic image recreation results also ostensibly demonstrate significant improvements in SNR determination, with improvements in both feature and background noise representation for both CCD and CMOS sensors.

These outcomes laid the groundwork for the development of onboard software for debris tracking from a space-based telescope, to help Airbus' enable the processing data directly onboard.

Further work to improve the functionalities of the image simulator might cover:

- Defective pixel identification directly from science images
- Bolometric corrections for star signals
- Variational tumbling phase functions
- Optimization in sampling conditions from the GAIA database
- Improvements to vibration simulation and atmospheric dispersion model

Annexes

I Image Stacking

Image stacking is commonly used in astrophotography to improve observations through this post-processing step. The stacking procedure computes the median or average of each pixel across a multitude of images, creating a new 2D array. This effectively improves the SNR of the observation, without increasing the exposure time. Since mean calculations are sensitive to outliers, stacking procedures are generally performed with the median.

Source: *Long Exposure Vs Image Stacking For Astrophotography (nightskypix.com)*

Figure 77: Single frame vs Stacked sky images

However, median computations in python require the simultaneous storage of all the images in memory, in a process that can easily require significant resources. We can in fact calculate the memory required using the formula:

$$M = N_{images} \cdot N_{bands} \cdot N_{bits} \cdot (Height * Width) \tag{47}$$

If we were to stack just 20 images for our CMOS sensor array (14192x10640 pixels, 16bits, monochrome), this process would require roughly 45 gigabytes of RAM. It's quite easy to see that an alternative, procedural method should be implemented to save memory usage.

A median approximation algorithm has been developed by *Tibshirani2008*[20], that effectively counts a "running median" by dividing the data into bins and counting them until half of all the numbers are accounted for. At this point, one can approximate that the median is located at the half-point of the bin where we stop our algorithm.

Algorithm 2 Pseudocode

```
procedure BinApprox Algorithm
    $(\mu, \sigma)$ ← Mean/Standard Deviation
Set the bounds:
    $minval = \mu - \sigma$
    $maxval = \mu + \sigma$
Ignore values >= maxval
Set bin width:
    $width = 2\sigma/B$
    (ignoreBin) ← if value < minval
Count and add the bin counts until (N+1)/2:
    for n in B do
        Bcounts[n] = B.count(minval <= value < minval + width.
        minval += width.
    for n in Bcounts do
        RunningCount += Bcounts[n]
        if RunningCount >= (N+1)/2 then
            Return midpoint of B[n]
        else
            Continue
```

For our purposes, bins do not need to be stored after being counted, and the memory allocated for those is freed up. Thus this method does not suffer from the common memory problems that characterize regular median stacking methods.

The downside of using this algorithm is that the precision of the answer is accurate to $\frac{\sigma}{B}$, when using a B number of bins, thus using a sufficiently large number of bins is critical to obtain reliable results.

II FWHM and EE

In signal theory and optics, FWHM and EE are often used interchangeably to characterize lens and detector performance.

Full Width at Half Maximum (FWHM) is the width of a distribution curve between the points at half of the maximum amplitude. FWHM proves useful in image processing since it's a convenient way to define in terms of pixels the drop-off of a certain diffraction pattern.

Ensquared and **Encircled Energy** (EE), are a measurement concept of concentration of energy within a region of an optical image. When measured from the centroid of a PSF, one can calculate the enveloped energy within a given radius (Encircled Energy) or within a given side of a square (Ensquared energy).

Figure 78: EE in the centroid pixel compared to FWHM

It is possible to calculate EE and FWHM interchangeably by making the three following assumptions:

1. The PSF is located in the centroid of the pixel
2. The PSF is modelled as a 2D Gaussian distribution
3. $\sigma_x = \sigma_y$

Under the second assumption, FWHM and σ are linked from the following relationship:

$$FWHM = 2\sigma\sqrt{2\ln 2} \approx 2.355\sigma \tag{48}$$

Through the definition of error function:

$$erf(z) = \frac{2}{\sqrt{\pi}} \int_0^z e^{-t^2} \mathrm{d}t \tag{49}$$

If FWHM is known, we can convert to EE, using the same σ as calculated in equation (48).

$$EE = erf\left(\frac{a}{\sigma\sqrt{2}}\right) \tag{50}$$

That is a probability of the energy residing between -a and +a (where a = half window size).

In absence of the first and third assumptions (PSF located at any position), the EE of a given pixel range is determined as:

$$EE_x = \frac{1}{2}\left(erf\left(\frac{L_{b,x} - \mu_x}{\sqrt{2}\sigma}\right) - erf\left(\frac{L_{a,x} - \mu_x}{\sqrt{2}\sigma}\right)\right) \tag{51}$$

$$EE_y = \frac{1}{2}\left(erf\left(\frac{L_{b,y} - \mu_y}{\sqrt{2}\sigma}\right) - erf\left(\frac{L_{a,y} - \mu_y}{\sqrt{2}\sigma}\right)\right) \tag{52}$$

Where L_b and L_a are respectively the distance to the upper and lower pixel bounds of the window (not necessarily square).

III Phase function models

The function for a perfectly diffuse (lambertian) sphere is:

$$\theta_{F,1}(\phi) = \frac{2}{3\pi^2}[(\pi - \psi)\cos\psi + \sin\psi] \tag{53}$$

Where ψ is the object-sun phase angle. For the perfectly specular model we use the formula:

$$\theta_{F,2}(\phi) = \frac{1}{4\pi} \tag{54}$$

We represent the diffuse-specular model as a linear combination of these two functions:

$$\theta_F(\phi) = \beta\theta_{F,1} + (1-\beta)\theta_{F,2} \tag{55}$$

For **tumbling plate-like** objects, we integrate across all possible orientations of a plate-like object and we calculate an averaged reflective phase function.

$$\theta_F(\theta) = \frac{\sin(\psi)\sin(\psi+\theta)\cos^2(\chi)}{\pi} \tag{56}$$

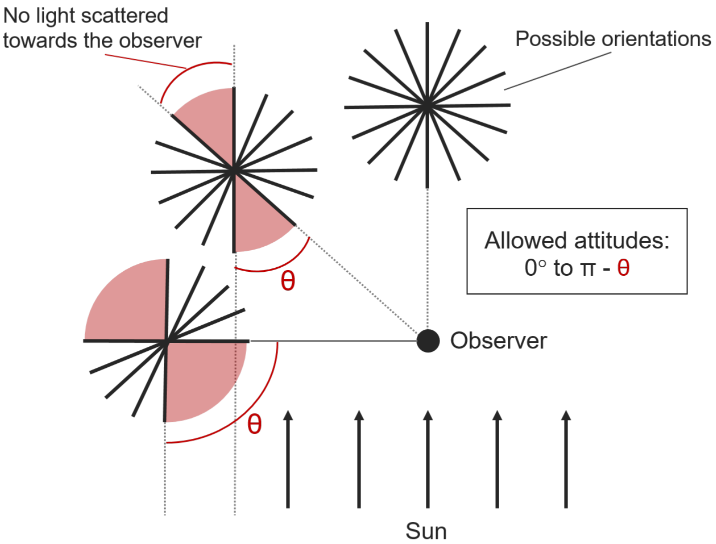

Figure 79: Permissible attitudes for light scattering

We can compute the average illuminated surface as:

$$\begin{aligned} I_{avg} &= \frac{1}{\pi^2}\int_0^{\pi}\int_0^{\pi-\theta} \theta_F(\theta)\,\mathrm{d}\psi\mathrm{d}\chi \\ &= \frac{1}{\pi^3}\int_0^{\pi}\int_0^{\pi-\theta} \sin(\psi)\sin(\psi+\theta)\cos^2(\chi), \mathrm{d}\psi\mathrm{d}\chi. \end{aligned} \tag{57}$$

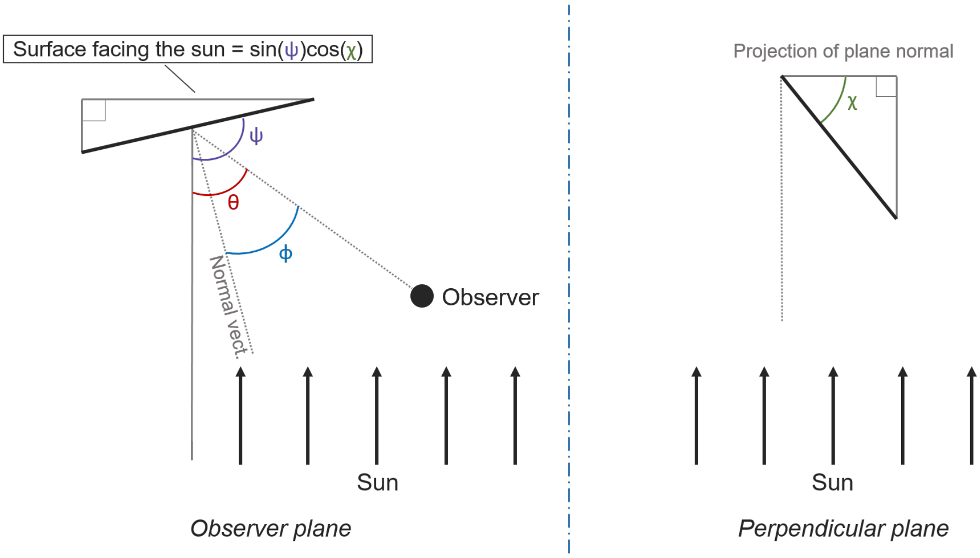

Figure 80: Geometry of a tumbling plate facing the Sun

IV Randomization techniques

For the purposes of an image simulator, replicability of consistent imagery is essential to evaluate software performance. To attain such a goal, utilization of a seed-based generation is necessary for all pseudo-random processes. Luckily this constitutes a common problem in the image-processing community, and there are multiple packages available on python to solve this issue. The methods offered in *numpy.random* are more than sufficient, and we utilize *random.seed* and *random.randint* functions to obtain consistent results. However, a procedural pixel-by-pixel randomized generation is not possible due to concerns related to the Birthday Paradox, a vericidal statistical paradox which demonstrates how a very low number of permutations can have a very high probability to be repeated.

For example, if we generate 10.000 defective pixels across a 4008x2672 pixel grid (N = 10.709.376 total pixels), we can calculate the probability that duplicates will occur if we cumulate all the individual probabilities of overlap:

$$P(n) = (1 - \prod_{n=1}^{10000} (1 - \frac{n}{N})) \cdot 100 = 99.062679\% \tag{58}$$

Where N is the total number of pixel, and n represents the current defective pixel position being randomized. Evidently, we must allocate some memory to store a set of non-duplicated values through permutation. For these purposes we use the *random.RandomState* method, and we index the pixel positions by collapsing and flattening the 2d grid into a 1d list. This list can then be

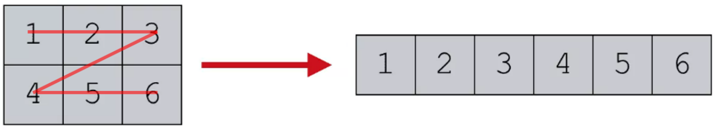

Figure 81: Flattening of 2D grid for unique index referencing

easily used for logging in output pixel data on original ADU values, pixel positions and ADU offset and proportional increase.

It is also important to note that seeds utilized for pixel defects and noise within a sequence of images should differ. The seed assigned to noise should change on every subsequent image, and no two noises should share the same seed (to avoid superimposition). For pixel defects, however, we shall utilize the same seed across all images, since these defects constitute an intrinsic characteristic of the hardware itself, and will always retain the same properties.

V Vignette generation

Some images captured by the telescope exhibit a reduction in image brightness at the peripheral regions of the field of view. This effect could be caused by light path obstructions or improper mirror design. There are multiple types: mechanical, optical, natural, pixel, and artificial vignetting are some examples, but for the purposes of the simulator it is not necessary to distinguish between the different types, instead one must construct a model that can simulate any vignette shape as it becomes necessary.

The vignetting we experience on the ART affects mostly the left and right sides of the image, and median values along the rows of the images remain unaffected. The data of the columns, however, experiences a gradient in decrease of brightness that begins in proximity of the edges. We can obtain a visual representation of the data if we superimpose the median of values of the columns on top of the image itself:

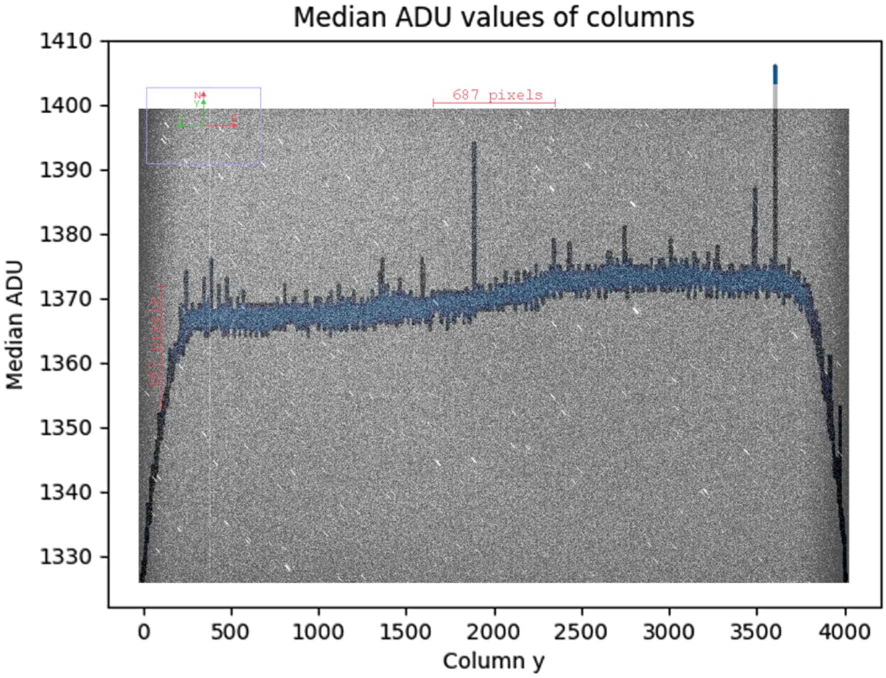

Figure 82: Vignetting phenomena on ART imagery

We can distinguish two regions within the image: the central region maintains roughly the same ADU values, with the exception of some single columns that are affected by column defects. The peripheral regions are affected directly by the vignetting, experiencing an average decrease of almost 40 ADU at the very edge.

To properly replicate the variety of possible vignetting that might arise, it was chosen to use the bivariate normal distribution PDF:

[H]

$$
\begin{aligned}
f(x,y) = \frac{1}{2\pi(1-\rho^2)^{1/2}\sigma_x\sigma_y} exp\Bigg[&- \frac{1}{2\pi(1-\rho^2)}\left(\frac{x-\mu_x}{\sigma_x}\right)^2 \\
&-2\rho\left(\frac{x-\mu_x}{\sigma_x}\right)\left(\frac{y-\mu_y}{\sigma_y}\right)+\left(\frac{y-\mu_y}{\sigma_y}\right)^2\Bigg]
\end{aligned}
\tag{59}
$$

In addition to the PDF parameters, the implementation within the simulator also accepts the following values:

- **Correlation** ρ: determines the shape and orientation
- **Standard deviations** σ_x **&** σ_y: determine the shape
- **Offset x & y**: modify values of μ_x & μ_y, determines the foci of the vignette
- **Peak Value**: determines the maximum value at the edge

- **Coverage**: determines spread of covered area by the vignette

These parameters allow the user to replicate a variety of gradient maps that can be used to replicate both vignetting (when subtracting the maps) or amp-glow (when adding the maps). Some examples of the maps generated are shown below:

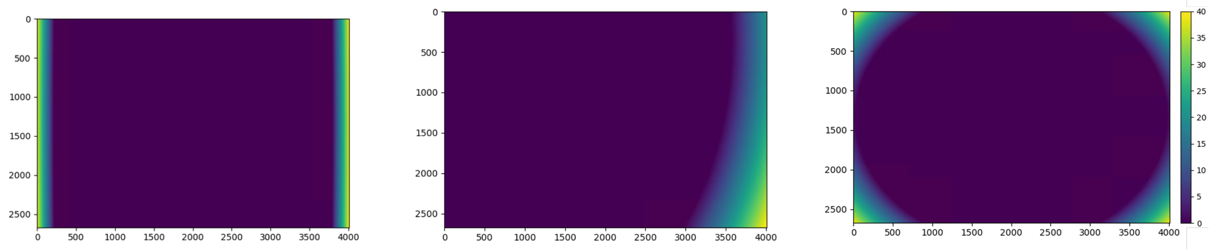

Figure 83: Types of synthetic vignettes

Where in the left image: $\sigma_y = 100\sigma_x$. Middle: offset x,y; Right: $\rho = 1$

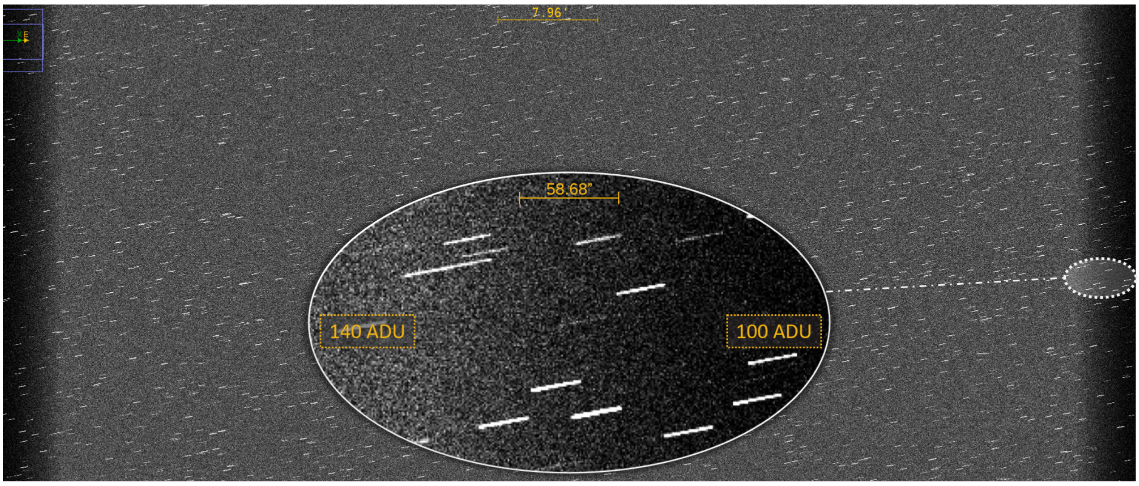

Figure 84: Synthetic image with 40 ADU peak side vignetting

VI Pixel dwell time

For SNR estimation in both Sideral and Tracking scenarios, it's necessary to estimate the deposited energy of signal sources. If there is no relative movement between the sensor and signal source, the solution is trivial and the integration time of the sensor is identical to the dwell time. However, for surveilance scenarios, this is not often the case and one must calculate the relative velocity when the signal is projected on the image focal plane.

If we assume a circular orbit, we can calculate the tangent velocity of the object as $v_t = \omega * R$. We can determine the velocity within the focal plane as:

$$v_{focalplane} = \frac{v_t}{R} * f \tag{60}$$

Calculating the pixel dwell time is now straightforward:

$$t_{dwelltime} = \frac{A_{pixel}}{v_{focalplane}} \tag{61}$$

VII Scenarios Results

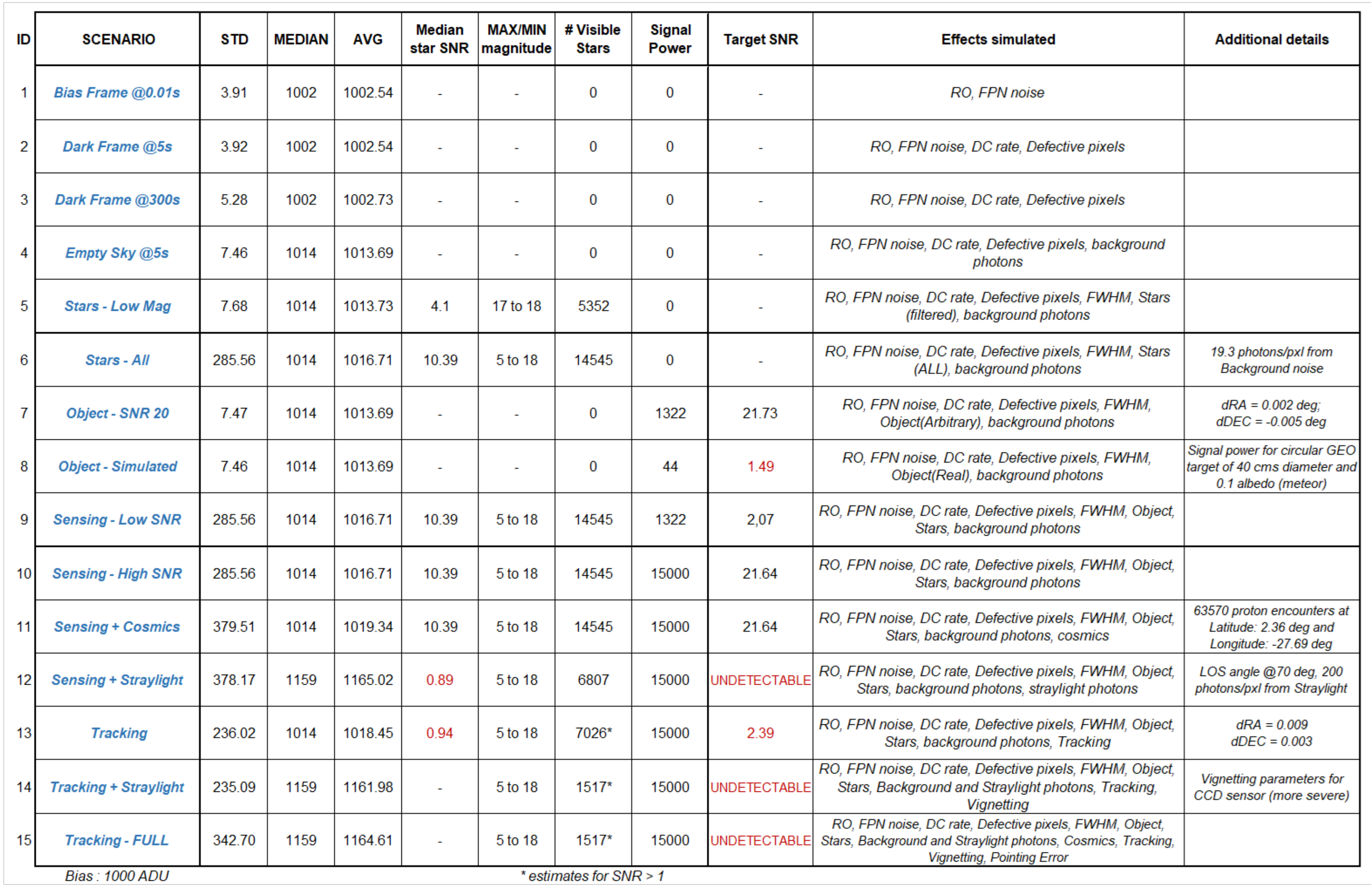

ID	SCENARIO	STD	MEDIAN	AVG	Median star SNR	MAX/MIN magnitude	# Visible Stars	Signal Power	Target SNR	Effects simulated	Additional details
1	*Bias Frame @0.01s*	3.91	1002	1002.54	-	-	0	0	-	*RO, FPN noise*	
2	*Dark Frame @5s*	3.92	1002	1002.54	-	-	0	0	-	*RO, FPN noise, DC rate, Defective pixels*	
3	*Dark Frame @300s*	5.28	1002	1002.73	-	-	0	0	-	*RO, FPN noise, DC rate, Defective pixels*	
4	*Empty Sky @5s*	7.46	1014	1013.69	-	-	0	0	-	*RO, FPN noise, DC rate, Defective pixels, background photons*	
5	*Stars - Low Mag*	7.68	1014	1013.73	4.1	17 to 18	5352	0	-	*RO, FPN noise, DC rate, Defective pixels, FWHM, Stars (filtered), background photons*	
6	*Stars - All*	285.56	1014	1016.71	10.39	5 to 18	14545	0	-	*RO, FPN noise, DC rate, Defective pixels, FWHM, Stars (ALL), background photons*	*19.3 photons/pxl from Background noise*
7	*Object - SNR 20*	7.47	1014	1013.69	-	-	0	1322	21.73	*RO, FPN noise, DC rate, Defective pixels, FWHM, Object(Arbitrary), background photons*	*dRA = 0.002 deg; dDEC = -0.005 deg*
8	*Object - Simulated*	7.46	1014	1013.69	-	-	0	44	1.49	*RO, FPN noise, DC rate, Defective pixels, FWHM, Object(Real), background photons*	*Signal power for circular GEO target of 40 cms diameter and 0.1 albedo (meteor)*
9	*Sensing - Low SNR*	285.56	1014	1016.71	10.39	5 to 18	14545	1322	2,07	*RO, FPN noise, DC rate, Defective pixels, FWHM, Object, Stars, background photons*	
10	*Sensing - High SNR*	285.56	1014	1016.71	10.39	5 to 18	14545	15000	21.64	*RO, FPN noise, DC rate, Defective pixels, FWHM, Object, Stars, background photons*	
11	*Sensing + Cosmics*	379.51	1014	1019.34	10.39	5 to 18	14545	15000	21.64	*RO, FPN noise, DC rate, Defective pixels, FWHM, Object, Stars, background photons, cosmics*	*63570 proton encounters at Latitude: 2.36 deg and Longitude: -27.69 deg*
12	*Sensing + Straylight*	378.17	1159	1165.02	0.89	5 to 18	6807	15000	UNDETECTABLE	*RO, FPN noise, DC rate, Defective pixels, FWHM, Object, Stars, background photons, straylight photons*	*LOS angle @70 deg, 200 photons/pxl from Straylight*
13	*Tracking*	236.02	1014	1018.45	0.94	5 to 18	7026*	15000	2.39	*RO, FPN noise, DC rate, Defective pixels, FWHM, Object, Stars, background photons, Tracking*	*dRA = 0.009 dDEC = 0.003*
14	*Tracking + Straylight*	235.09	1159	1161.98	-	5 to 18	1517*	15000	UNDETECTABLE	*RO, FPN noise, DC rate, Defective pixels, FWHM, Object, Stars, Background and Straylight photons, Tracking, Vignetting*	*Vignetting parameters for CCD sensor (more severe)*
15	*Tracking - FULL*	342.70	1159	1164.61	-	5 to 18	1517*	15000	UNDETECTABLE	*RO, FPN noise, DC rate, Defective pixels, FWHM, Object, Stars, Background and Straylight photons, Cosmics, Tracking, Vignetting, Pointing Error*	

Bias : 1000 ADU

** estimates for SNR > 1*

References

[1] *ESA / Space Safety / Space Debris / About Space Debris*. Accessed: 20-06-2023. URL: `https://www.esa.int/Space_Safety/Space_Debris/About_space_debris`.

[2] Heiner Klinkrad. *Space Debris, Models and Risk Analysis*. Springer Berlin Heidelberg, 2006. DOI: `10.1007/3-540-37674-7`. URL: `https://doi.org/10.1007/3-540-37674-7`.

[3] K. Fletcher. "Space Debris: the ESA Approach". In: *ESA Brochure* (Mar. 2017), p. 012069. URL: `https://esamultimedia.esa.int/multimedia/publications/BR-336/offline/download.pdf`.

[4] Giovanni Cirillo Simone Cantarella Martin Michel Yannick Heinz and Jens Utzmann. "Airbus Robotic Telescope and SPOOK as test-bed for space-based space surveillance". In: ESA Space Debris Office, Jan. 2023. URL: `https://conference.sdo.esoc.esa.int/proceedings/neosst2/paper/54/NEOSST2-paper54.pdf`.

[5] Oscar Rodriguez Fernandez Jens Utzmann Maria G. Dimitrova Vesselinova. "Airbus Robotic Telescope". In: ESA Space Safety Programme Office, 2023. URL: `https://conference.sdo.esoc.esa.int/proceedings/neosst1/paper/424/NEOSST1-paper424.pdf`.

[6] Jean Kovalevsky and P. Kenneth Seidelmann. *Fundamentals of Astrometry*. Cambridge University Press, 2004. DOI: `10.1017/CBO9781139106832`.

[7] George H. Kaplan. "Atmospheric Refraction of Light from Nearby Objects in Space". In: NAVAL OBSERVATORY WASHINGTON DC United States, 2014. URL: `https://apps.dtic.mil/sti/citations/AD1094247`.

[8] Mikhail Konnik and James Welsh. *High-level numerical simulations of noise in CCD and CMOS photosensors: review and tutorial*. 2014. arXiv: `1412.4031 [astro-ph.IM]`.

[9] Martin Marciniak. "On the testing and validation of stray light attenuation for microsatellite star tracker baffles." In: 2014. URL: `https://rshare.library.torontomu.ca/articles/thesis/On_the_testing_and_validation_of_stray_light_attenuation_for_microsatellite_star_tracker_baffles/14665248`.

[10] Muhammad Iqbal. *An Introduction to Solar Radiation*. en. Elsevier, Dec. 2012. ISBN: 9780323151818. URL: `https://www.sciencedirect.com/book/9780123737502/an-introduction-to-solar-radiation`.

[11] Tingxin Xu et Al. Yan Ouyang. “An Approach to Space-Debris Optical Image Simulation Considering the Streak and Saturated Star-Background”. In: *Journal of Physics: Conference Series* 1060.1 (July 2018). DOI: `10.1088/1742-6596/1060/1/012069`. URL: `https://dx.doi.org/10.1088/1742-6596/1060/1/012069`.

[12] Patrik Kukić et al. “Correction for meteor centroids observed using rolling shutter cameras”. In: *WGN, the Journal of the IMO* 46:5 (2018), p. 154. URL: `https://globalmeteornetwork.org/wordpress/wp-content/uploads/2018/11/Kukic-et-al-2018-Rolling-shutter.pdf`.

[13] MD Hejduk. “Specular and diffuse components in spherical satellite photometric modeling”. In: *Proceedings of the Advanced Maui Optical and Space Surveillance Technologies Conference.* 2011, pp. 1–11. URL: `https://www.semanticscholar.org/paper/Specular-and-Diffuse-Components-in-Spherical-Hejduk/c781c63d51ffdd9d253999305b11cdd684047aa0`.

[14] Michael Bass. *Handbook of Optics, Vol. 2: Devices, Measurements, and Properties, Second Edition.* Optical Society Of America, 1994, p. 38.10. URL: `https://cdn.preterhuman.net/texts/science_and_technology/physics/Optics/Handbook%20of%20Optics%20%20second%20edition%20vol.%202%20-%20Bass%20M.pdf`.

[15] Gabriel Cristóbal. *Optical and Digital Image Processing.* Wiley-VCH, 2011, pp. 840–845. URL: `https://onlinelibrary.wiley.com/doi/book/10.1002/9783527635245`.

[16] MA 02138 AAVSO 185 Alewife Brook Parkway Suite 410 Cambridge. *Guide to CCD/CMOS Photometry, with Monochrome Cameras.* 2022, pp. 52–53. ISBN: 978-1-939538-62-8.

[17] Glenn H. Chapman et al. “Predicting Pixel Defect Rates Based on Image Sensor Parameters”. In: *2011 IEEE International Symposium on Defect and Fault Tolerance in VLSI and Nanotechnology Systems.* IEEE, Oct. 2011. DOI: `10.1109/dft.2011.58`. URL: `https://doi.org/10.1109/dft.2011.58`.

[18] Glenn H. Chapman et al. “Empirical formula for rates of hot pixel defects based on pixel size, sensor area, and ISO”. In: *SPIE Proceedings.* Ed. by Ralf Widenhorn and Antoine Dupret. SPIE, Feb. 2013. DOI: `10.1117/12.2005850`. URL: `https://doi.org/10.1117/12.2005850`.

[19] D. L. Shupe et al. “The SIP Convention for Representing Distortion in FITS Image Headers”. In: *Astronomical Data Analysis Software and Systems XIV.* Ed. by P.

Shopbell, M. Britton, and R. Ebert. Vol. 347. Astronomical Society of the Pacific Conference Series. Dec. 2005, p. 491.

[20] Ryan J. Tibshirani. *Fast computation of the median by successive binning*. 2008. DOI: `10.48550/ARXIV.0806.3301`. URL: `https://arxiv.org/abs/0806.3301`.